CHALMERS
UNIVERSITY OF TECHNOLOGY

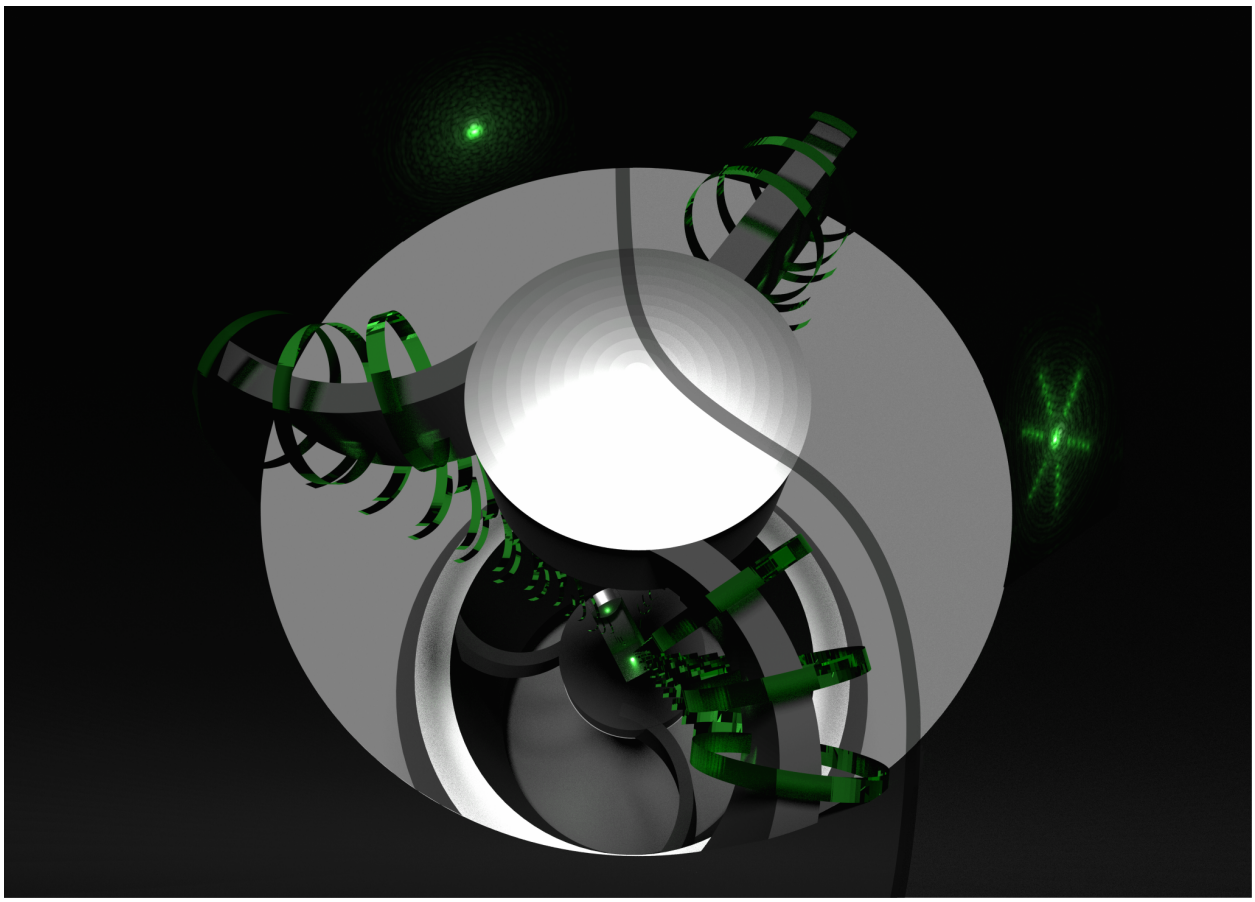

Reduction of parasitic diffraction effects in reflective microscope objectives

Investigation on alternative design of light-obscuring support structure for the secondary mirror

Master's thesis in Photonics

Rasmus Larsson

Department of Microtechnology and Nanoscience
CHALMERS UNIVERSITY OF TECHNOLOGY
Gothenburg, Sweden 2019

Master's thesis 2019

Reduction of parasitic diffraction effects in reflective microscope objectives

Investigation on alternative design of light-obscuring support structure for the secondary mirror

Rasmus Larsson

CHALMERS
UNIVERSITY OF TECHNOLOGY

Department of Microtechnology and Nanoscience
Photonics laboratory
Chalmers University of Technology
Gothenburg, Sweden 2019

Reduction of parasitic diffraction effects in reflective microscope objectives
Investigation on alternative design of light-obscuring support structure for the secondary mirror
Rasmus Larsson

Supervisor: Kristof Seidl & Stina Guldbrand, Thorlabs
Examiner: Jörgen Bengtsson, Photonics laboratory at the department of Microtechnology and Nanoscience

Master's Thesis 2019
Department of Microtechnology and Nanoscience
Photonics laboratory
Chalmers University of Technology
SE-412 96 Gothenburg
Telephone +46 31 772 1000

Cover: An illustration of diffraction from spider vanes. To the left of the dividing line: curved supports and corresponding diffraction pattern. To the right of the dividing line: the same but for straight supports. Note that certain elements visible here are not present in the physical microscope objectives studied in this work.

Typeset in LaTeX
Printed by Chalmers Reproservice
Gothenburg, Sweden 2019

Reduction of parasitic diffraction effects in reflective microscope objectives
Investigation on alternative design of light-obscuring support structure for the secondary mirror
Rasmus Larsson
Department of Microtechnology and Nanoscience
Chalmers University of Technology

Abstract

Imaging systems employing reflective elements for focusing light can be superior to traditional lens-based systems for use in broadband applications, or at wavelengths where lenses are unavailable. They are, however, hampered by stray intensity spikes caused by diffraction against the secondary mirror support structure. The use of curved vanes for reducing the intensity spikes present for conventional straight supports has previously been investigated[1, 2] but their implementation in short focal length systems, such as microscope objective lenses, has until now remained fairly unexplored. This thesis investigates the reduction of intensity spikes in 15X and 40X reflective Shcwarzschild microscope objective lenses, where, among different support geometries, the use of curved vanes is further analysed.

By simulating diffraction of various support designs it was found that a constant curvature structure, comprising three arms, each with a subtended arc angle of 70° minimised the intensity spikes whilst still performing well with regard to other image quality criteria. In addition, the use of non-constant curvature structures for compensation of Gaussian beams was shown beneficial using numerical methods.

Practical implementation was carried out in the design of a 15X curved support structure Schwarzschild objective lens and was further experimentally tested and compared to a 15X Schwarzschild objective lens employing straight vanes. Results show a clear improvement in reduction of intensity spikes in favour of the curved vane structure. The measured data furthermore indicate a minor degradation with respect to other image quality criteria, in accordance with simulations.

Keywords: Point spread function, Spider vane, Diffraction, Numerical propagation, Schwarzschild objective, Mirror supports.

Acknowledgements

With the completion of this thesis I want to express my sincere thank you to all people who have contributed in making this work possible, be it in direct assistance, long term guidance or general support in life on the side.

First, a big thank you to my supervisors, mainly Kristof Seidl who, with his expertise on optics and practical experience, has been a great support in the lab as well as providing key insights and guidance to the project as a whole. I also want to thank Thorlabs for giving me the chance to take on this project and for accommodating me with a pleasant working environment and the experimental equipment necessary for carrying through the work. A special thanks to Olle Rosenqvist for advertising Thorlabs at Chalmers and furthermore help inspiring me in choosing my current Master's programme. I also enjoyed our brief discussions on different optics and photonics topics that occured from time to time.

I also want to thank Jörgen Bengtsson for his course in optics, but perhaps more importantly, for taking on the role as examiner for this work and for supplying me with tips along the way.

Moreover, I wish to express my major gratitude toward Mikael Ströberg and Christina Lundberg for excellent teaching and for sparking my interest for physics which, without doubt, have played an essential role in bringing me to this point. So also, I wish to thank all lecturers, teaching assistants and lab supervisors I have had the chance to learn and inspire from during the, most brilliant, "Wireless, Photonics and Space engineering" master's programme.

For support in my studies, beside my studies and for brightening life in general, I wish to thank all of my friends. To my family I am sincerely grateful, for all the support, help and for always believing in me. Lastly, I want to thank myself, for always putting the time and effort into my interests and the projects I undertake.

Rasmus Larsson, Gothenburg, june 2019

Contents

1
Introduction

Light, or electromagnetic radiation, is a fundamental physical phenomenon that plays an essential role in the workings of our universe. Through its interaction with matter it functions as an essential component in many well known physical processes such as the photosynthesis, luminescence, fusion and lasing to name a few. When part of the energy, or momentum, carried by light is transferred to the material with which it interact the response may be stored as information of the event. This is the principle of a light sensor and if a number of such sensors are separated in space and placed in the focal plane of an imaging system a picture is obtained, enabling the operational system to perceive the surrounding environment.

The imaging system maps the incoming light to individual sensor elements such that points of the viewed scene are resolved. The principle is ancient, developed by evolution itself and has since the dawn of man enabled us to see the world by forming an image on the retina of our eyes.

Thus, it is not surprising that the study of optics dates back several thousands of years[3] and that the interest for the topic still pushes the technology forward today [4, 5, 6].

Important optical systems that have been developed comprises the telescope [7]; for resolving distant objects, the microscope; for resolving small scale objects as well as advanced camera objectives for achieving photo realism. Conventionally, just like our eyes, most of these imaging systems utilize the functionality of a transparent lens to map the observed scene to the sensing elements. The traditional lens does, however, not perform a perfect transformation of light and impairments known as aberrations will reduce the system's image quality. One aberration that is inherent to the use of lenses is chromatic aberration which is an effect of chromatic dispersion of the lens medium. Since light of different wavelengths travels at different speeds inside a medium the delay imposed on the light by the lens will differ and thus the different colours will focus at different distances. This as well as other aberrations can be mitigated by the use of different compound lens schemes that may cancel the unwanted effects, though, the construction of such systems are usually costly and time consuming as many lenses need to be aligned with high precision. Moreover, the improved performance over spectral range scale with complexity and number of lenses used. Therefore it is difficult to realise a broad band imaging system based on lenses solely.

An alternative to transparent lenses is the use of curved mirrors, an idea that was realised already during the 17:th century[7] as a means of evading chromatic aberration in telescope design. The focusing is simply achieved using a concave and convex mirror and the principle still finds use in modern systems such as the

Hubble space telescope which employs a Cassegrain reflector design[8]. Reflective objectives are also used in microscope systems for broad spectral imaging where the most prevalent reflector design is the Schwarzschild objective[9].

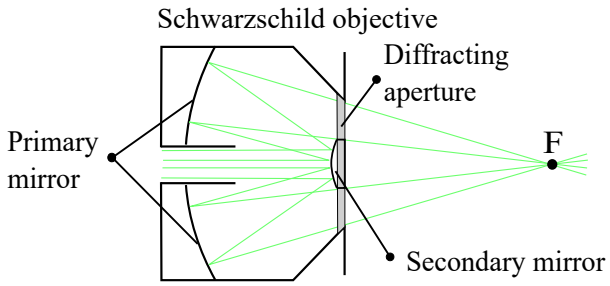

(a) A simple schematic of a Schwarzschild microscope objective. the green lines represent the light ray path through the system. The focal point is located in point F

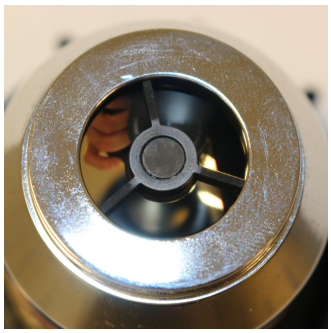

(b) An image of the diffracting aperture of the Schwarzschild microscope objective employing straight supports.

Figure 1.1

Different designs of reflective imaging systems help reduce many of the unwanted aberrations in addition to the advantage of always being free from chromatic dispersion. However, the use of two mirrors is often followed by a practical issue with regard to the support structure of the secondary mirror, also denoted as spider vanes. In the action of maintaining the mirror in place the support will obscure the light path causing the radiation to diffract against it, see figures 1.1a and 1.1b. When imaging with coherent light, the diffraction in turn leads to intensity spikes in the obtained image if using conventional straight support structures[1] (see figure 1.2). This effect may pose a considerable problem for certain applications where it is of importance that the focused light is narrowly confined. The anisotropic spread of light away from the focus also breaks the circular symmetry of an imaged point which degrades its visual appearance [10]. It should be mentioned that, in off-axis reflective systems the problem of light obstruction is avoided, although the asymmetric shape of these systems make them more susceptible to other aberrations that are difficult to compensate. Their increased size may also pose another issue for microscopy applications.

Figure 1.2: An image of the diffraction pattern caused by a reflective Schwarzschild objective with straight supports. The diffraction pattern is the image obtained in point F presented in figure 1.1a.

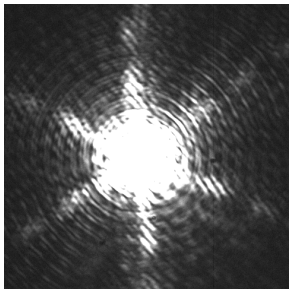

Some work has been put in to investigate the effect of mirror supports on various image quality criteria and how, using curved support structures, these effects may be reduced[1, 2]. The analysis of spider vane diffraction is however not complete, especially considering short focal length systems such as microscope objectives where the light ray trajectories are far from parallel. This thesis focuses on furthering the

incomplete analysis in the interest of practical implementation of support structures aimed to reduce the undesired diffraction for reflective microscope objectives. In particular, the work covers the spider vane design of a 15X and a 40X Schwarzschild objective but the methods employed may be extended to designs of similar optical systems. Furthermore, depending on the user preference and how it values different image quality criteria, the optimum spider vane design may vary. A general approach toward this problem is carried out so as to accommodate most user preferences with a single design. In addition, the effect of different input intensity distributions on diffraction is briefly investigated and further expanded in the special case of Gaussian beams.

1.1 Aim

As presented above, the aim of the thesis encompasses the study of spider vane diffraction in short focal length systems. This with the goal to develop support structures for such a system that reduce the unwanted diffractive effect while still maintaining the other optical qualities of the system at a desired level. The resulting analysis is to be practically implemented on the 15X and the 40X Schwarzschild microscope objectives developed at Thorlabs Sweden[11] and takes into account different image quality criteria when optimising the final design.

The following goals have been set as means of achieving the stated aims.

- Identify and implement an accurate numerical propagation method for optical simulations on the Schwarzschild objective
- Develop an experimental setup able to measure the diffraction from the spider vanes, more specifically the point spread function (PSF) of the objective
- By means of simulation, find and optimise a spider vane structure that reduces the diffraction while maintaining the other original optical design qualities
- Via experimental measurements verify the simulations and confirm that the improved qualities of the developed design are obtained also in practice.

1.2 Thesis outline

Presented here is the structure employed for this thesis:

- In Chapter 1, the thesis topic is provided together with a background explaining its relevance. The aim of the thesis work is presented along with concretised goals.
- In Chapter 2 the theory of diffractive optics, relevant to the thesis work, is covered.
- Chapter 3 presents the experimental setup and methodology used for measuring the PSF for the Schwarzschild objectives and other investigated systems.
- In chapter 4 the numerical propagation method used for simulating diffraction from the support structures is presented and further analysed with respect to performance.

- Chapter 5 describes the process of finding the optimal spider vane design according to the above stated aims. This includes a brief treatment of diffraction of non-uniform input fields, in particular Gaussian beams.
- Chapter 6 deals with the practical implementation of the optimised spider vane geometry found in chapter 5.
- The results and discussion of the Schwarzschild objective prototype experimental testing is presented in chapter 7.
- In chapter 8, conclusions summarise the thesis work.

The approach of this report structure is to provide results and discussions continuously in each chapter, concerning the matter at hand, rather than summarising each in its separate part.

2

Free space optics

To identify an optical propagation method suitable to simulate the imaging system under study, and perhaps more importantly, to understand the observed diffraction, it is necessary to review the underlying physical model. This chapter will mainly briefly describe some relevant concepts employed throughout the thesis.

2.1 Imaging systems

As briefly mentioned in Chapter 1 an imaging system maps light rays emitted by a point to another point in space. Conventionally, this mapping is achieved by a transparent lens, see figure 2.1.

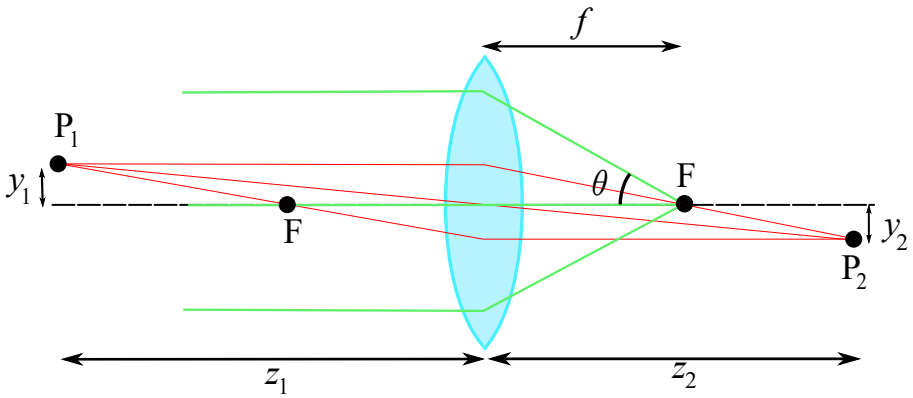

Figure 2.1: A simple imaging system comprising a lens. A point P_1 is imaged to a point P_2. Parallel rays are focused in the focal plane z =F.

Parallel rays are focused in a plane (the focal plane) at a distance from the lens denoted as the focal distance f. The magnification M of the imaged point P_1 onto P_2 is $M = z_2/z_1$. Though the visualisation here is given by ray optics the concept is the same as for wave theory of light. The lens achieves the focusing of incoming light by imposing a spatially dependent phase change such that the total phase change accumulated between point P_1 and point P_2 is the same regardless of path through the lens. A measure of a systems angular view is the numerical aperture, defined as $\mathrm{NA} = n \sin\theta$, where n is the refractive index of the medium after the lens (usually air).

2.1.1 The Schwarzschild objective

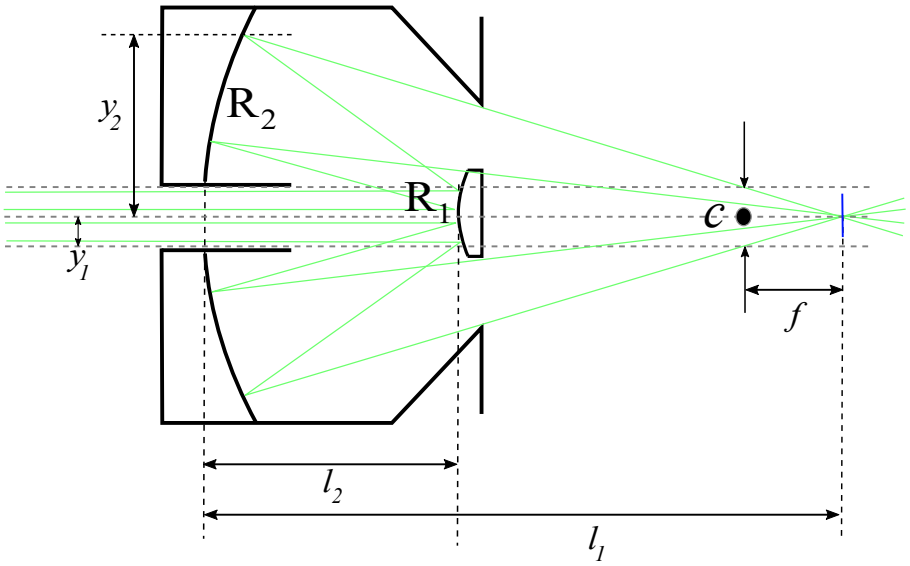

Figure 2.2: A rough schematic of a reflective Schwarzschild imaging system. The exact parameter relations are given by (2.1). Note that R_1 and R_2 are radii centered in point c.

The Schwarzschild objective is a type of imaging system that achieves the point to point mapping utilising a pair of spherical mirrors, see figure 2.2. The two spherical surfaces with radii R_1 and R_2 are concentric in point c. When the objective is used in infinity corrected systems the image plane coincides with the focal plane (blue in the figure). The parameter relations for the Schwarzschild objective considered in this work are given in (2.1)[12]. Using these parameter relations eliminates third order spherical aberration, coma and astigmatism.

$$\begin{cases} l_2 &= 2f \\ l_1 &= (\sqrt{5}+2)f \\ R_1 &= (\sqrt{5}-1)f \\ R_2 &= (\sqrt{5}+1)f \\ y_2 &= (\sqrt{5}+2)y_1 \end{cases} \tag{2.1}$$

2.2 The electromagnetic wave

The underlying physics governing propagation of light is described by the set of relations known as Maxwell's equations[13]. For linear, nondispersive, isotropic and homogeneous media one solution is the plane wave. Using complex vector notation, the electric field for a monochromatic plane wave propagating in $\hat{k}$ is given by (2.2)[13].

$$\mathbf{E}(\mathbf{r}) = \mathbf{E}_0 e^{j\mathbf{k}\bullet\mathbf{r}} \tag{2.2}$$

Here, $\mathbf{k} = \hat{k}2\pi/\lambda$ is the wavenumber, λ the wavelength and $\mathbf{E}_0$ the complex amplitude of the field ($\mathbf{k} \perp \mathbf{E}_0$). The time averaged poynting vector $\bar{\mathscr{P}}$ describes the direction and magnitude of the propagating power. For free space propagation it is related to the intensity via $\bar{\mathscr{P}} = I\hat{k}$ where the intensity I is related to the electric field as $I \propto |E|^2$.

2.2.1 Coherent light

Coherence is a measure of how well the light correlates with itself at different points in time, denoted "coherence time" and at different positions on the wavefront, denoted "spatial coherence". Conventional light sources, with an extended light-emitting area and a broadband radiation, emit light with very low coherence, whereas laser light is typically highly coherent.[13]

2.2.2 The scalar approximation

When considering wave propagation in free space where the interfering plane waves are close to parallel and of the same polarisation it is usually convenient to omit the vector notation. The plane wave is then rewritten in a scalar form, see (2.3).

$$U(z) = U_0 e^{jkz} \tag{2.3}$$

U_0 is the field amplitude and $\hat{z}$ is taken as the direction of propagation. For short focal length systems such as the Schwarzschild objective this approximation may appear questionable. Consider figure 2.2, the worst imaginable case would be linearly polarised light in the plane of the picture and the largest error would occur for the plane waves (E_1, E_2) travelling furthest away from each other through the system. Their trajectories are separated by an angle $v = 2\arcsin(y_1/f)$ and their superposed fields would measure $\mathbf{E} = \sin(v/2)(E_1 - E_2)\hat{z} + \cos(v/2)(E_1 + E_2)\hat{y}$. The intensity of these interfering waves would measure $I \propto \sin^2(v/2)(E_1 - E_2)^2 + \cos^2(v/2)(E_1 + E_2)^2$ while in the scalar approximation we would have $I_{\text{scalar}} \propto (E_1 + E_2)^2$. The intensity error, or difference is thus $I - I_{\text{scalar}} \propto -4\sin^2(v/2)E_1E_2$. The largest error is obtained for when $|E_1| = |E_2|$ and the resulting relative intensity error becomes $(I - I_{\text{scalar}})/I_{\text{scalar}} = \sin^2(v/2) = \Delta I_{\text{scalar}}$. ΔI_{scalar} thus serves as an estimate for the accuracy of the scalar approximation. Keep in mind though that this is an error representing the interference between two single waves. When considering interference between all waves travelling through the objective the relative intensity error is likely to be far smaller in every point than the presented estimate.

2.2.3 The spherical wave

A solution to Maxwell's equations in the scalar approximation is the spherical wave. The spherical wave describes the field as radiated from a single point in space. The scalar spherical wave is presented in (2.4)[13].

$$U(r) = \frac{U_0}{r} e^{jkr} \tag{2.4}$$

Here, U_0 is a constant and r the distance from the point source. The waves propagate radially away from this point and the wavefronts constitute spherical surfaces.

2.2.4 The Gaussian beam

Another solution to Maxwell's equations in the scalar approximation is the Gaussian beam, see (2.5)[13].

$$U(\rho,z) = U_0 \frac{w_0}{w(z)} \exp\Big[-\frac{\rho^2}{w^2(z)}\Big] \exp\Big[jkz + jk\frac{\rho^2}{2R(z)} - j\zeta(z)\Big]$$
$$w(z) = w_0\sqrt{1+(z/z_0)^2}, \quad z_0 = \frac{\pi w_0^2}{\lambda}, \quad R(z) = z[1+(z_0/z)^2], \quad \zeta(z) = \arctan(z/z_0) \tag{2.5}$$

Here, ρ is the radial distance from the axis z along which the field propagates. $w(z)$ is the beam radius $\rho = w(z)$ at which the field amplitude has dropped to $1/e$ of its value on the z-axis. w_0 is the minimum beam radius present at focus in $z = 0$ and $R(z)$ is the wavefront radius of curvature. The Gaussian beam is an important solution that very well approximates collimated optical beams such as those produced by lasers.

2.3 Scalar Fourier optics

Figure 2.3: A representation of the propagation problem where the field $g(x,y)$ in plane S_2 is sought from knowledge of of the field f in plane S_1, a distance d away along the z-axis.

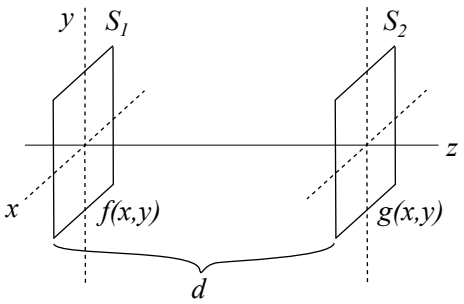

The general principle of scalar Fourier optics in free space states that an arbitrary scalar field can be represented by a sum of plane waves with different amplitudes and different directions. By applying the transfer function of free space to each plane wave component, the field in an arbitrary plane can be calculated as the superposition of all plane waves propagated from the input plane.

Consider an optical system with optic axis along $\hat{z}$, see figure 2.3. A plane wave of wavelength λ, $2\pi/\lambda = k = \sqrt{k_x^2+k_y^2+k_z^2}$, with an arbitrary direction of propagation can be written as $U(x,y,z) = U_0 \exp[j(k_x x + k_y y + k_z z)]$. If a snapshot of this plane wave is taken in any plane orthogonal to $\hat{z}$ the plane wave represents a single harmonic function, $f(x,y) = U_0 \exp[j2\pi(\nu_x x + \nu_y y)]$, in coordinates (x,y) with spatial frequencies $\nu_x = k_x/2\pi$, $\nu_y = k_y/2\pi$.

Let the harmonic function f be present in the input plane $z = 0$. To propagate this function to an output plane separated by a distance d_z along $\hat{z}$ we simply multiply f

with the propagation factor in the z-direction: $g(x, y, z = d_z) = f(x, y) \cdot \exp(jk_z d_z)$. The input-output relation for a single spatial harmonic is then given by, (2.6)[13]:

$$g(x,y) = H(\nu_x,\nu_y)f(x,y), \quad H(\nu_x,\nu_y) = \exp(jk_z d_z) \\ = \exp\left(jd_z\sqrt{k^2 - k_x^2 - k_y^2}\right) = \exp\left(j2\pi d_z\sqrt{\frac{1}{\lambda^2} - \nu_x^2 - \nu_y^2}\right) \quad (2.6)$$

where $H(\nu_x, \nu_y)$ is the transfer function of free space. For propagating an arbitrary input field $f(x, y)$ we decompose it into its plane wave components:

$$F(\nu_x,\nu_y) = \iint_{-\infty}^{\infty} f(x,y)\exp[-j2\pi(\nu_x x + \nu_y y)]dxdy = \mathscr{F}\Big\{f(x,y)\Big\}(\nu_x,\nu_y) \quad (2.7)$$

and the output field is readily determined as the superposition of the propagated harmonics at the output plane:

$$g(x,y) = \iint_{-\infty}^{\infty} F(\nu_x,\nu_y)H(\nu_x,\nu_y)\exp[j2\pi(\nu_x x + \nu_y y)]d\nu_x d\nu_y \\ = \mathscr{F}^{-1}\Big\{F(\nu_x,\nu_y)H(\nu_x,\nu_y)\Big\}(x,y) \quad (2.8)$$

$\mathscr{F}$ and $\mathscr{F}^{-1}$ here denote the 2-dimensional fourier transform and its inverse. This methodology for calculating the output field, given an input field, is applicable for all linear optical systems, not only free space propagation and it is commonly denoted "angular spectrum propagation".

In the special case of the input field being a single point source, that is, a delta function centered at $(x = 0, y = 0)$ one obtains the impulse response function h as the output field: $h(x,y) = \mathscr{F}^{-1}\Big\{H(\nu_x,\nu_y)\Big\}(x,y)$. The modulus square of the impulse response function is defined as the point spread function, PSF$= |h(x,y)|^2$, which represents the intensity distribution in the output plane induced by a point source in the input plane. The PSF is an important quantity for an imaging systems since it provides information on its ability of mapping a single point in the object plane to a point in the image plane. Another common quantity that provides image quality information is the modulation transfer function, defined as [14]: $\mathrm{MTF}(\nu_x,\nu_y) = \Big|\mathscr{F}\Big\{\mathrm{PSF}(x,y)\Big\}(\nu_x,\nu_y)\Big|$, which describes the transmission of the individual spatial frequencies[14, 15].

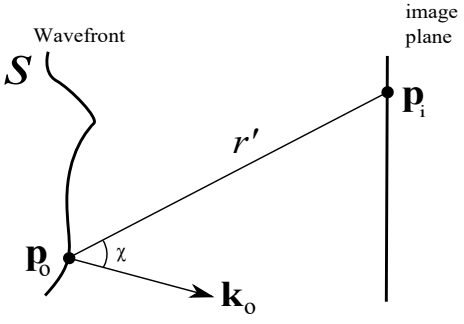

Figure 2.4: A visualisation of Huygen-Fresnel's principle. Point $\mathbf{p}_0$ lies on the object wavefront S and emits a spherical wave that contributes to the field in point $\mathbf{p}_i$. The distance between them is r' and the angle between directions $\mathbf{p}_0 - \mathbf{p}_i$ and $\mathbf{k}_0$ is χ.

2.3.1 Huygen-Fresnel's principle

An alternative approach to evaluating the field in the output plane, given an input field, is to employ Huygen-Fresnel's principle. According to Huygen-Fresnel's principle, each point $\mathbf{p}_0$ on a wavefront emits a spherical wave with an amplitude proportional to the E-field amplitude in that point, see figure 2.4. Furthermore the spherical wave sent out is shifted in phase by $\frac{\pi}{2}$ relative to the phase of the field in that point. The field in $\mathbf{p}_i$ is then the superposition of spherical waves emitted from the object plane.[13] Moreover, seeing as the object wave has a direction of propagation, the medium being homogeneous, isotropic and linear thus suggests $\mathscr{P} \parallel \mathbf{k}$. The amount of radiated power in a specific direction from each point on the object plane will therefore depend on the angle relative to the phase front normal. To account for this we use the factor derived in Kirchhoff's diffraction formula together with accompanying physical constants. The final expression for the E-field in $\mathbf{p}_i$ is then given by (2.9)[16]:

$$g(\mathbf{p}_i) = \frac{-i}{2\lambda} \int_S f(\mathbf{p}_o) \frac{e^{ikr'}}{r'} (1 + \cos\chi) dS \tag{2.9}$$

where g is the field in $\mathbf{p}_i$ and f is the field in $\mathbf{p}_o$. S is the surface of integration (object wave phase front) and dS is the differential area element of S.

2.3.2 Diffraction

A field that is let to propagate through and beyond an amplitude modulating aperture generates an intensity distribution called a diffraction pattern. This pattern is the results of interference between the diverging waves that result from transmission through the aperture. The diffraction will depend on the properties of the incoming wave, the modulation imposed by the aperture as well as at what distance from the aperture the intensity is viewed. Commonly, an aperture consists of a thin opaque screen with areas providing transmission. The aperture function $p(x, y)$ is thus spatially dependent and takes on only two possible values: 1 where the aperture transmits and 0 where it is opaque. The relation between the optical field just in front of (f_1) and behind (f_2) the aperture is usually approximated by $f_2(x, y) = p(x, y)f_1(x, y)$. Although this approximation violates the fact that the electric field must remain continuous it provides accurate results in many optical diffraction problems[16]. Evaluating the field in an image plane further away is then accomplished using, for example, angular spectrum propagation of free space or Huygen-Fresnel's principle, on the field f_2. For calculating the PSF one must only make sure that the field f_1 is that generated by the point source.

In the special case of far field diffraction, or, diffraction through a lens with focal length f, it can be shown that the input-output relation reduces to: $g(x, y) \propto \mathscr{F}\Big\{f_2(x/\lambda d, y/\lambda d)\Big\}$ [13], where d is the propagation distance (and $d = f$ in the case of a lens). Furthermore, if the field f_1 is a plane wave propagating along $\hat{z}$, i.e $f_1 = 1 \ \forall \ \{x, y\}$ the resulting field becomes $g(x, y) \propto \mathscr{F}\Big\{p(x/\lambda d, y/\lambda d)\Big\}$ [13]. The diffraction pattern thus becomes the modulus square of the fourier transform of the aperture function. For later reference, two simple aperture functions and

their corresponding fourier transforms are presented: the rectangular aperture (see (2.10), (2.11) and figure 2.5) and the circular aperture (see (2.12), (2.13) and figure 2.5)[13].

$$p_{\text{rect}}(x,y) = \begin{cases} 1, & -d_x/2 \leq x \leq d_x/2, \quad -d_y/2 \leq y \leq d_y/2 \\ 0, & \text{else} \end{cases} \tag{2.10}$$

$$E(x,y) \propto d_x d_y \text{sinc}\left(\frac{d_x x}{\lambda d}\right)\text{sinc}\left(\frac{d_y y}{\lambda d}\right), \quad I(x,y) \propto |E(x,y)|^2 \tag{2.11}$$

$$p_{\text{circ}}(\rho,\phi) = \begin{cases} 1, & \rho \leq D/2 \\ 0, & \text{else} \end{cases} \tag{2.12}$$

$$E(\rho) \propto \frac{2DJ_1(\pi\rho D/\lambda d)}{\pi\rho}, \quad I(\rho) \propto |E(\rho)|^2 \tag{2.13}$$

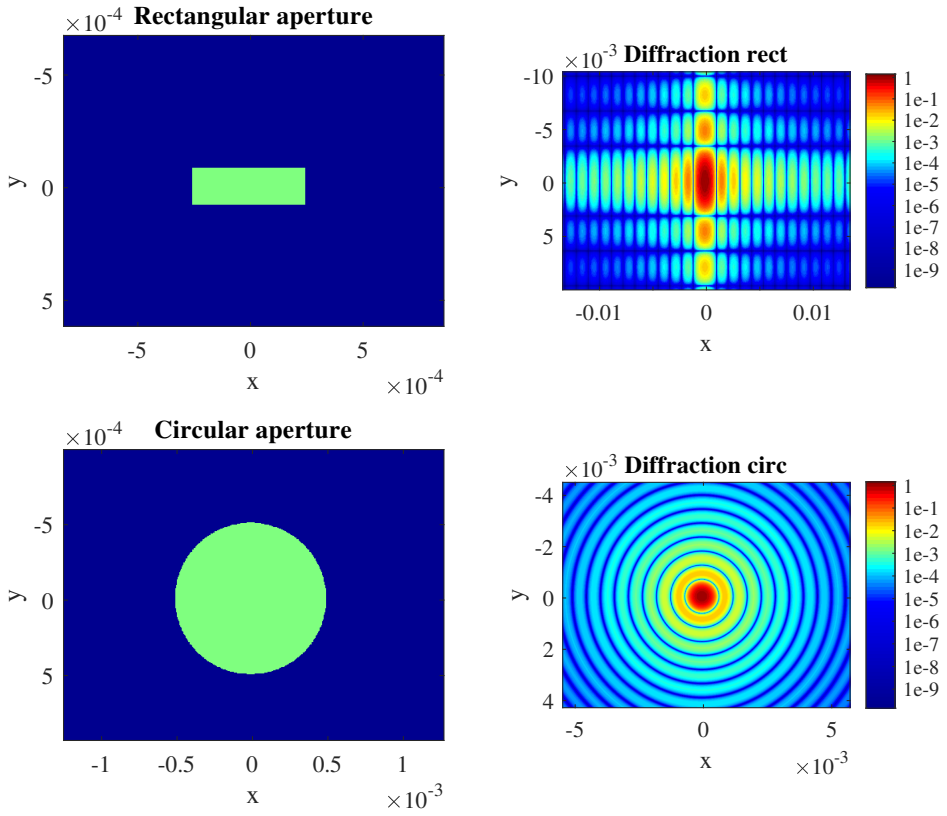

Figure 2.5: Here, the diffraction from the rectangular aperture given in (2.10) as well as the circular aperture in (2.12) is visualised. Parameters used: $f = 1$, $D = 1 \cdot 10^{-3}$, $d_x = D/2$, $d_y = D/6$, $\lambda = 543 \cdot 10^{-9}$. The respective diffraction pattern is normalised to its maximum value and the relative magnitude is visualised in colour.

d_x and d_y are the dimensions for the rectangular opening while D is the circular aperture diameter. d is the propagation distance, (ρ, ϕ) polar coordinates and $J_1(x)$

is the first order bessel function of first kind which is bound by an envelope function approximately proportional to $1/\sqrt{\rho}$[17]. Here, $\mathrm{sinc}(x) = \sin(\pi x)/\pi x$.

3
Measuring diffraction

In the purpose of verifying simulation results experimentally and ultimately for providing evidence for the improved diffraction pattern of an optimised spider vane design a method for measuring the diffraction pattern is required. This chapter presents the measurement technique employed throughout the work with purpose of capturing the intensity distribution for the different investigated optical systems. In addition, the numerical image analysis aimed at circumventing the limited measurement window of the camera, is briefly described.

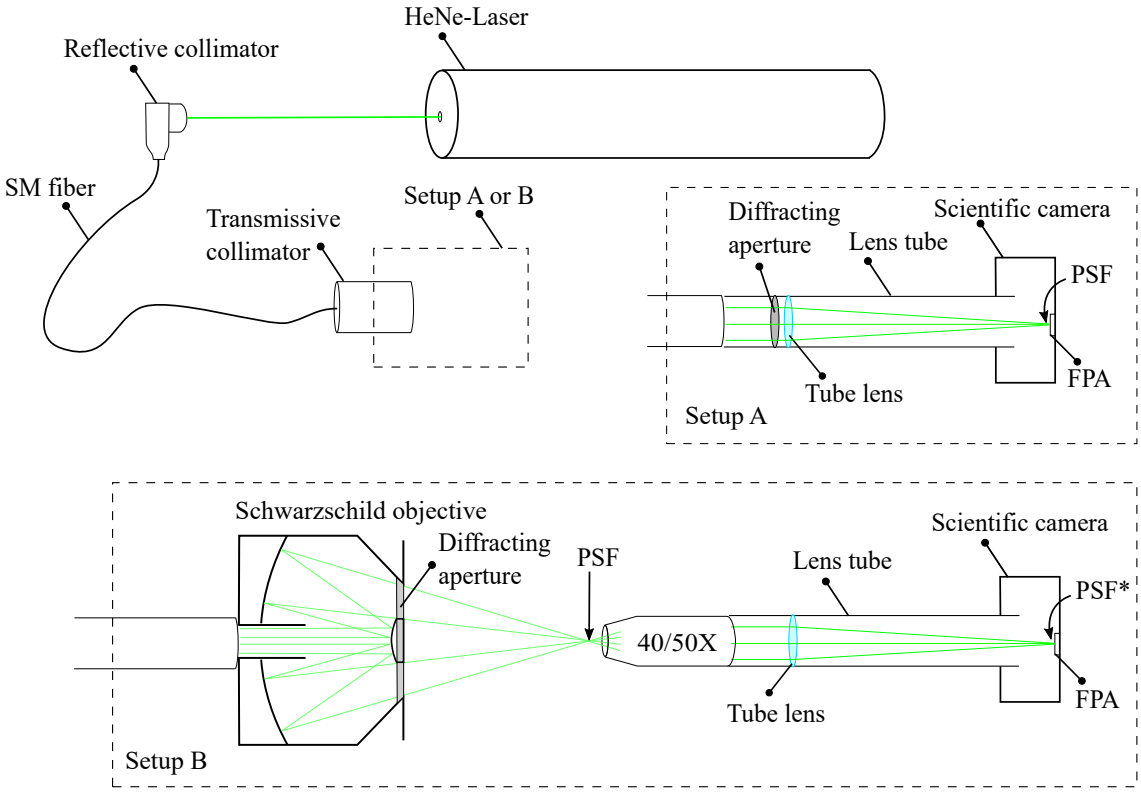

Figure 3.1: A schematic of the experimental setup employed.

3.1 Experiment

The experimental setup utilised for measuring the diffraction is depicted in figure 3.1. A complete list of the equipment is provided in appendix B.1.

Recall from section 2.3.2 that the input optical field f_1, the aperture function p and

the properties of propagation between f_2 and g determine the observed diffraction pattern. When measuring the diffraction of a given system it is thus of interest to control these three aspects.

When comparing simulation with experiment, knowledge of the input field of the system, system structure as well as pixel size in the focal plane array is required. These parameters have not been measured but taken as lookup values from schematics and website specs for used equipment. Here (optical) field refers to the complex electrical field, amplitude and phase, as discussed in chapter 2.

3.1.1 Forming the input field

First and foremost, a light source producing monochromatic waves of high coherence is needed for generating the diffraction pattern in accordance with section 2.2.1. To accommodate this a Helium-Neon laser was used. With a wavelength of $\lambda = 543\,\text{nm}$ the light is in the range of the intended use of the Schwarzschild objectives studied and since it also lies in the visible spectrum the problem of tracking the beam was simplified.

The continuous wave emitted by the laser is focused into a single mode fiber via a reflective collimator. At the opposite end of the fiber the light is coupled out into free space using a transmissive collimator. The idea behind the fiber was to utilise the fiber to collimator-transition which outputs a large waist, near Gaussian, output beam that closely resembles the plane waves required to produce the PSF. Moreover, by tweaking the alignment of the reflective collimator the transmitted power could be varied.

The two types of optical systems that are experimentally studied in this work are the Schwarzschild objective (see section 2.1.1) and the simple lens system presented in section 2.1. With regard to the Schwarzschild objective's intended use in infinity corrected systems and the simplicity of using tube lens optics for the setup it was decided to study diffraction in the focal plane for both systems. Points imaged in the focal plane are located in infinity (recall section 2.1) and the spherical wave incident on the objective, or lens, generated by any such point is approximately a plane wave across the input aperture. To check whether the Gaussian beam, the input field of the objective, is a valid approximation to a plane wave one can calculate the phase front radius of curvature and amplitude distribution of the field using (2.5). For this setup, the distance from the beam waist to the input aperture is on the order of [cm] and the beam radius on the order of [mm] which produce small phase differences on the order of [mrad] over the, below centimeter sized, input apertures. The intensity distribution across the input aperture is however not as constant, considering a beam radius of $w_0 = 3.7\,\text{mm}$ and an input aperture radius of $4\,\text{mm}$ on the 15X Schwarzschild objective. Though the Gaussian beam does not perfectly replicate a plane wave it is deemed sufficient for the analysis of diffraction in this thesis as experimental results matched simulations, taking this flaw into consideration, quite well.

3.1.2 Producing and imaging the diffraction

When studying the simple lens system of section 2.1 a thin screen with a hole and central obscuration, forming an annular aperture, is placed right in front of the tube lens according to setup A in figure 3.1. The field is then let to propagate from the transmissive collimator, through the lens tube and up till the aperture screen. After transmission through the aperture screen the PSF is readily obtained at the focal plane of the tube lens where it is captured by a focal plane array of a scientific monochromatic CCD camera. To clarify, the infinity corrected imaging system under study here comprises the aperture screen and the tube lens.

When studying the Schwarzschild objective the optical field is transmitted through the objective where it diffracts against the spider vane structure supporting the secondary mirror, see setup B in figure 3.1. The PSF we wish to measure is readily obtained in the focal plane of the objective, however, due to the short focal length of the objective the focal plane PSF is too small to resolve adequately using the available CCD camera. To enhance the resolution of the Schwarzschild PSF it is magnified using an additional imaging system. A 40X or 50X transmissive objective maps the PSF to infinity before it is refocused onto the FPA by the tube lens, altogether accomplishing a magnification of roughly 40-60X. The secondary imaging system was aligned manually to the Schwarzschild focal plane using translational stages and for minimising vibrational fluctuations, the setup was mounted on an optics table for both studied systems. The use of this secondary imaging system will alter the Schwarzschild PSF by its transfer function and produce a modified (and magnified) PSF* but for the purpose of this work this effect is considered insignificant since the magnifying objective's numerical aperture is larger than the Schwarzschild objective's which implies that it does not impose any additional major diffractive effects.

3.1.3 Registering the intensity

The intensity on the FPA is captured manually using an accompanying software tool to the scientific CCD camera. The tool allows for different exposure times and gain of the semiconductor PiN array elements. The dynamic range of the detector elements is limited by noise and saturation. To avoid saturation and blooming effects the power needs to be controlled. To change the input power to the system, the alignment of the reflective collimator is adjusted. Light outside the numeric aperture is thus lost if the angle is increased.

At the beginning of each measurement the exposure time and gain was set to minimum values and the angle of the collimator was altered until the peak intensity was not saturated. Then a series of images was captured when increasing the exposure time [1-100] ms. Larger exposure times risk smearing the intensity due to vibrations which caused the image to fluctuate at a frequency of 2 Hz at worst case over 1-2 neighbouring pixels. For increasing the measured signal further above the noise floor the collimator alignment was adjusted to let through more power. Using this series of images it was possible to artificially generate a larger dynamic range by removing noise and background lighting from lower exposure time images and removing saturated intensities from higher exposure time images. By stacking these

images on top of each other the PSF is reconstructed, compared to simulations and evaluated with respect to image quality criteria.

3.2 Image analysis

As already mentioned, noise and saturation in the photo detector elements of the CCD camera limit the intensity range available for accurate measurements. In order to capture a larger range of the PSF intensity values the image was scanned over the dynamic range by measuring the intensity at different input powers and exposure times. The individual measurements were filtered from noise and stacked on top of each other using a calculated relative gain determined from the measurements themselves. An example of a reconstruction of a PSF from raw data is presented in figure 3.2.

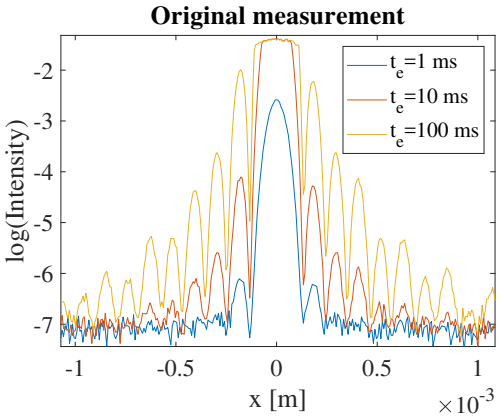

(a) Measurement of the intensity for three different exposure times $t_e = [1\text{ (blue)}, 10\text{ (red)}, 100\text{ (yellow)}]$ ms.

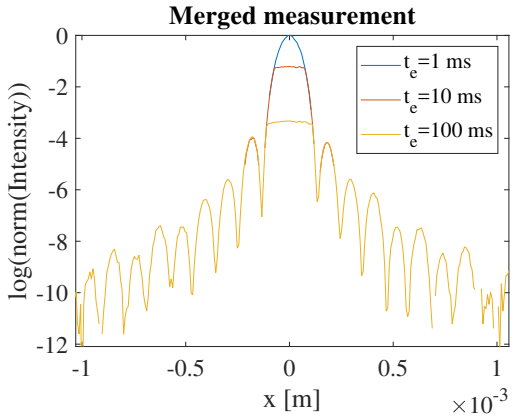

(b) The merged intensity of the individual measurements presented in figure 3.2a. The merging procedure used to obtain the fused data is described in section 3.2.

Figure 3.2: A visualisation of the merge of obtained intensity data. The data presented here is obtained from a cross-section through the PSF peak of measured 2D-data. Here "log" refers to the natural logarithm.

The complete algorithm employed for the merging of data is presented in appendix B.3.

4

Numerical field propagation

The ability of performing numerical simulations bring a great benefit to many design problems where the entire system is too complex to evaluate analytically and the possibilities of physically altering the device are limited. In addition, simulation results also contribute valuable information that enhances our understanding of the problem at hand. Regarding this work, as is common in optics, calculations become extensively difficult to carry out if all device parameters are taken into consideration [13, 18, 16]. The approach of manufacturing and testing a large number of different spider vane designs experimentally would instead be time consuming and costly. The benefit of utilising numerical simulations for this thesis' purpose is thus evident.

This chapter presents the numerical field propagation method that was developed and used for simulating diffraction for the optical systems studied in this project. For practical use of the presented method, additional material concerning the numerical implementation is presented in appendix A.1.

4.1 Choice of method

Figure 4.1: The geometry and coordinates used to describe propagation between the object and image planes.

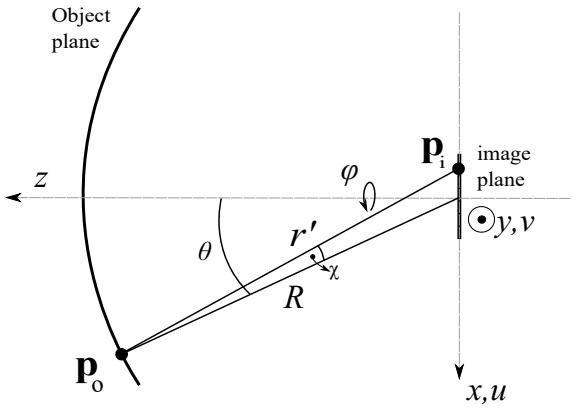

There are a number of well established propagation methods concerning propagation of scalar optic fields based on the Fresnel or Fraunhofer approximations[16, 13, 18], however, many of these approximations rely on the light rays being close to parallel. In the case of systems of large lateral extent compared to the propagation distance, such as the Schwarzschild objective, this is not the case and it has been verified in this work that the performed approximations do not hold and that the methods employing them produce erroneous results, see e.g appendix A.1.1.1. Using the exact expression of the free-space transfer function in the method of angular spectrum propagation, see section 2.3, instead requires an immense number of sampling points to satisfy the large spatial frequency bandwidth of the system, at the wavelength of interest. Using the two-step method, from [19], employing the

fresnel approximation requires the intermediate plane to be far away which imply a scaling factor close to unity which result in too coarse sampling in the image plane. These methods conventionally assume the object and image plane to be parallel and separated by a distance along the optic axis, recall figure 2.3.

In this work we avoid the problem of ridiculous sampling requirements and paraxial approximations by choosing the object plane to be a spherical surface cap focused in the focal plane where the PSF is evaluated, see figure 4.1. Just as for a plane wave transmitted through a lens the spherical wavefronts inside the Schwarzschild objective are concentric in the focal plane. It is thus convenient to choose this starting surface since it coincides with the phase front of the field travelling through the spider vane aperture. A straight forward way of calculating the output field from the phase front of an input field is in accordance with the Huygen-Fresnel principle.

Starting from the integral in (2.9), doing some mathematical manipulations and performing an approximation we arrive at the following expression (4.1) for the field in the image plane:

$$g(u,v) = -iRe^{ikR}e^{ik\frac{u^2+v^2}{2R}}\mathscr{F}\left\{\frac{f(\nu_x,\nu_y)}{\sqrt{\frac{1}{\lambda^2}-\nu_x^2-\nu_y^2}}\right\}(u,v) \tag{4.1}$$

The complete derivation of the result in (4.1) is given in appendix A.1.1. The approximation made in the derivation (further analysed in appendix A.1.1.1) assumes that the image plane's lateral extent is small, that the lateral extent of the object plane is not too large and that the propagation distance is not too small. Some propagation geometries are thus not supported by this method, however, for the purpose of evaluating the PSF for focused optical systems it performs quite well.

The variables $\nu_x = x/R\lambda$, $\nu_y = y/R\lambda$ bear a strong resemblance to the spatial frequencies discussed in section 2.3 but keep in mind that f has not undergone a fourier transform in this expression. Instead the spatial coordinates (x, y) have merely been rewritten for the purpose of writing the solution in the form of a fourier transform. The entire factor outside of the fourier transform describes a constant amplitude but varying phase across the image plane. When evaluating the normalised PSF this prefactor vanishes and the intensity assumes the shape of the absolute value squared of the fourier transform. Moreover, when the field before the diffracting aperture f_1 equals a constant over the entire plane, recall section 2.3.2, the field just after the aperture becomes proportional to the aperture function p. So in our concentric system, if we assume the aperture function p to be the shadow cast onto the spherical starting surface by the 3D-spider vane structure illuminated by a point source in focus, then the resulting PSF of the Schwarzschild objective is given by (4.2):

$$\mathrm{PSF}(u,v) \propto \left|\mathscr{F}\left\{\frac{p(\nu_x,\nu_y)}{\sqrt{\frac{1}{\lambda^2}-\nu_x^2-\nu_y^2}}\right\}(u,v)\right|^2 \tag{4.2}$$

The result in (4.2) is very similar to the case of far field diffraction described in section 2.3.2 which states that the diffraction is the fourier transform of the aperture function. The factor $1/\sqrt{\frac{1}{\lambda^2}-\nu_x^2-\nu_y^2}$ compensates the cartesian coordinate mapping onto the sphere and is further explained in appendix A.1.1. It is a slowly

varying function over the object surface and its influence on the PSF is generally small.

In terms of numerical evaluation, the fact that 4.2 comprises a fourier transform is very advantageous. The fast fourier transform algorithm available in most modern numerical softwares is extremely efficient and helps speed up simulations despite large array sizes.

4.2 Simulation parameters and constraints

When evaluating the PSF numerically from (4.2) there are a number of practical details to consider. If care is not taken when choosing the system parameters for the given simulation the method may break down and produce erroneous results. In relation to the physical dimensions of the optical system we wish to simulate, the sampling distance a and window size D_w play an important role. Firstly, the input field needs to be adequately sampled at the starting surface for the field at the image plane to be correctly calculated. The window size D_w obviously needs to span the entire aperture of the system but the choice of D_w further affects the presence of parasitic higher order spatial frequencies. The specific sampling requirements on a imposed by the choice of method are treated thoroughly in appendix A.1.2. The effect of window size on the evaluated field is treated in appendix A.1.3 where, in addition, the optimum choice of array size N, and sampling distance a is discussed.

When the sampling distance and window size have been set for a specific problem the array size N is determined as $N = D_w/a$ and represents the number of samples along each column and row. Using the fast fourier transform (FFT), the sampling distance b in the image plane can be computed as (4.3):

$$b = \frac{R\lambda}{Na} \tag{4.3}$$

This relation shows the trade off between adequate sampling in the object plane and high resolution in the image plane. This issue can be alleviated somewhat by increasing the amount of samples N but the price comes as increased computational time. Another parameter that is considered when choosing a and N is the window of interest in the image plane D_{image}. Points outside of this diameter risk being erroneous due to higher order spatial frequencies and insufficient sampling.

4.3 Testing of method

In the interest of evaluating the developed propagation method and to ensure it provides sufficient accuracy when simulating the Schwarzschild PSF it was tested against both theory and experiment. A comparison between analytic and numerical treatment of diffraction through a simple circular aperture is presented in section 4.3.1. In section 4.3.2 the simulation is compared to experimental results for diffraction through a thin screen annular aperture and in section 4.3.3 the PSF of the 15X Schwarzschild objective is simulated and compared to the measured PSF.

4.3.1 PSF of a focused imaging system with circular aperture

As mentioned in section 2.3.2 the resulting PSF from a circular aperture in a focused imaging system is described by (2.13). Figure 4.2 shows a comparison between evaluation of the diffraction problem using the analytic expression in (2.13) and the method developed in this chapter (4.1). Note that the PSF is normalised to its maximum value and presented as a cross-sectional plot for easier comparison. Used parameters are: $D = 1\,\text{mm}$, $d = 200\,\text{mm}$, $\lambda = 543\,\text{nm}$. For the numerical method, the input field is assumed to be a plane wave, and other values are $R = d$, $N = 7000$, $a = 3.8396\,\mu\text{m}$, $D_{\text{image}} = 2\,\text{mm}$.

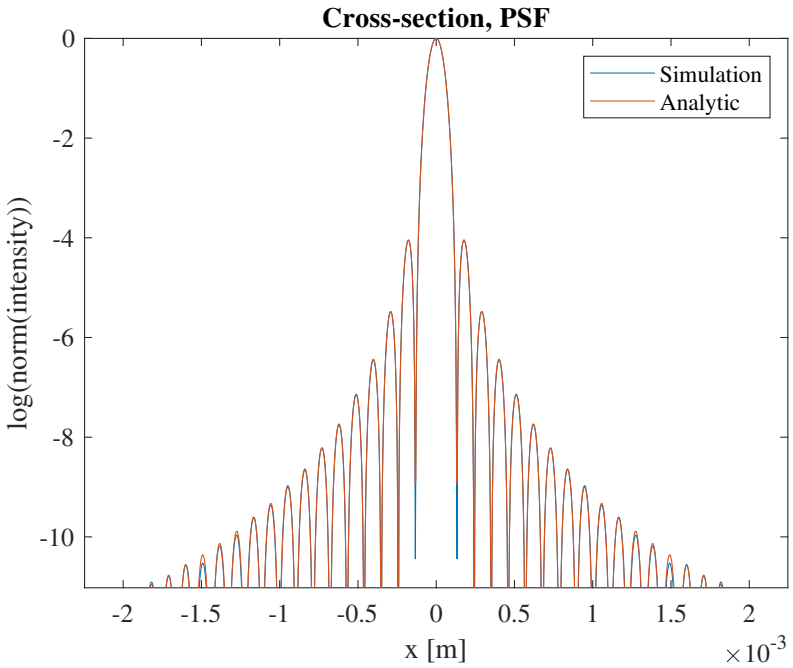

Figure 4.2: A numeric comparison between the diffraction patterns evaluated using the analytic expression in (2.13) (orange) and the numerical model in (4.1) (blue). ”log” indicates the natural logarithm.

It is clear from this comparison that the developed method and theory agree well for $x \leq D_{image}$. The small visual difference is most likely due to different sampling points for the two calculations.

4.3.2 Central obscuration diffraction

In this experiment the system under study comprises ”setup A” depicted in figure 3.1 where a central obscuration aperture element, see figure 4.3, was used as the diffracting aperture. The aperture element was placed just in front of the tube lens and the transmissive collimator was threaded onto the same tube system making the entire setup quite vibration insensitive.

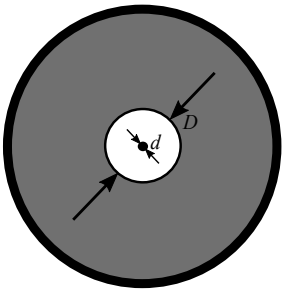

Figure 4.3: Annular aperture used as diffraction element in the experimental setup. The aperture is the item R1DF50 available at Thorlabs website with $D = 1\,\text{mm}$ mm and $d = 50\,\mu\text{m}$.

In the simulation the input field is taken as the spherical phase front exiting the tube lens, focused in the FPA, thus the simulated intensity pattern coincides with the measured intensity on the FPA. A comparison between measured intensity and simulated intensity is visualised in the form of a cross section plot given in figure 4.4. The input wave was assumed perfectly gaussian with $w_0 = 3.7\,\text{mm}$ and other simulation parameters are as follows: $d = 50\,\mu\text{m}$, $D = 1\,\text{mm}$, $R = 200\,\text{mm}$, $\lambda = 543\,\text{nm}$, $a = 3.8396\,\mu\text{m}$, $N = 7000$ and $D_{\text{image}} = 2\,\text{mm}$. The simulated intensity was translated in lateral coordinates using Matlab's image register to fit the experimental data. The experimental data was merged from three images taken at exposure times $\tau = [1, 10, 100]$ ms and minimum gain.

The comparison of experiment and simulation show a good agreement. The first seven orders of maxima match well whilst beyond, noise begin to disturb the measured data.

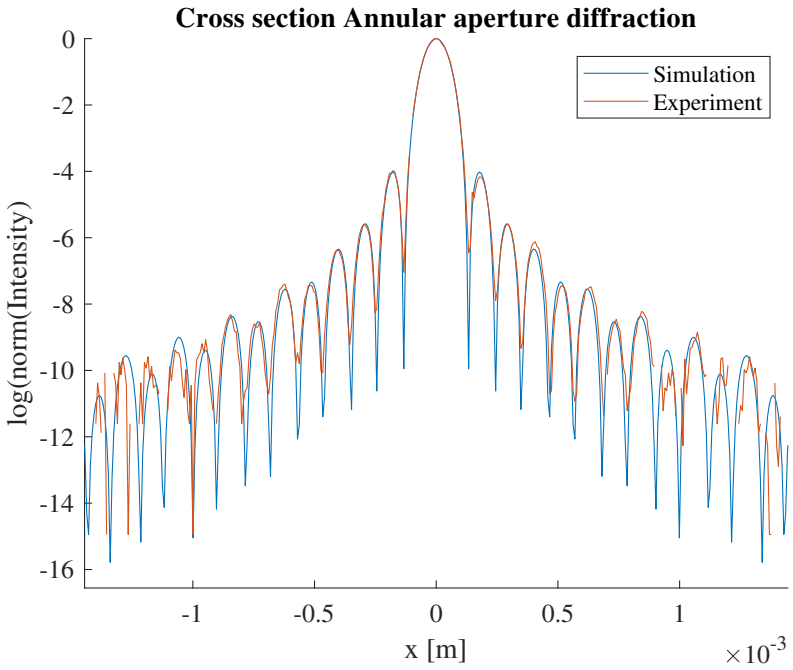

Figure 4.4: A cross section comparison between the measured normalized intensity (orange) and simulated normalized intensity (blue) using the numerical method in (4.1). "log" indicates the natural logarithm.

4.3.3 Diffraction of a Schwarzschild objective

In this experiment "setup B" was used, see figure 3.1, with the 40X transmissive magnifying objective. For a depiction of the physical dimensions of the objective

and its diffracting aperture see figures 4.5, 4.6a and 2.2. The Gaussian beam, with beam width $w_0 = 3.7\,\text{mm}$, incident on the objective inlet is propagated through the objective up to the object plane using a ray tracing method presented in appendix A.2. Though the secondary mirror and confining structure of the barrel will act as diffracting apertures their effect is neglected, mainly since the interior of the objective is designed to absorb stray light.

From knowledge of the device parameters, here: $t = 3\,\text{mm}$, $r_i = 3.8\,\text{mm}$, $R_i = 9.4\,\text{mm}$, $w = 0.9\,\text{mm}$, $L = 24.3\,\text{mm}$, $y_1 = 4\,\text{mm}$, $f = 13.3\,\text{mm}$, $\lambda = 543\,\text{nm}$ and using the relations in (4.4) the aperture projection $p(\nu_x, \nu_y)$ is readily determined. The use of a 2D aperture function for an extended aperture such as the support structure is a simplification but we justify it using the same argument as for the interior diffraction of the objective. The field present just after transmission through the aperture is visualised in figure 4.6b.

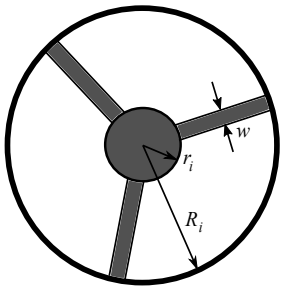

Figure 4.5: The diffracting spider vane aperture of the schwarzschild objective seen along the optic axis. The three, evenly distributed spokes support the central mirror.

$$\tan\theta_1 = \frac{r_i}{L}, \quad \tan\theta_2 = \frac{R_i}{L+t} \tag{4.4}$$

The choice of R is arbitrary, here $R = 24.6\,\text{mm}$, since the coordinates ν_x and ν_y depend only on θ and ϕ (recall figure 4.1 and see appendix A.1.1). This implies that the mathematics of the problem is independent of absolute dimensions, however, physically one should take care, especially if the system is shrunk to wavelength scale.

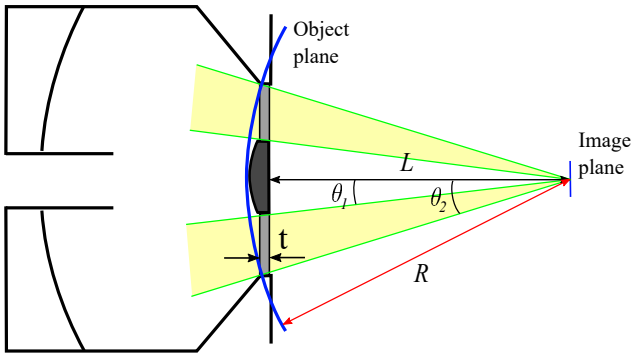

(a) A schematic of the aperture diffraction within the Schwarzschild objective. The starting surface, or object plane, is a spherical surface focused in the image (focal) plane. The aperture function p is the radial projection of the 3D spider vane structure onto the starting surface.

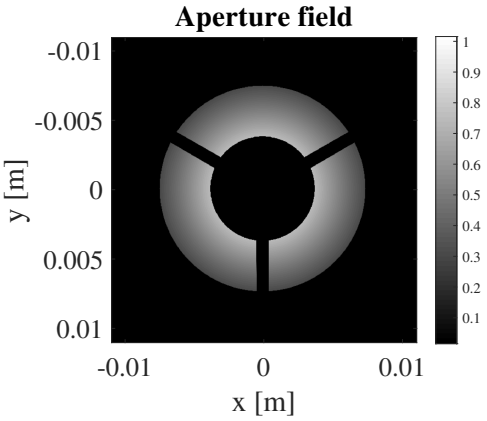

(b) Plotted here is the normalised aperture output field $f_2 = pf_1$, where p is the projected aperture function and f_1 the Gaussian field incident on the spherical surface aperture.

Figure 4.6

From the calculated aperture projection p the PSF is evaluated using (4.2) and

the simulated PSF for this objective is presented in figure 4.7. The measured PSF (PSF*) of the objective is presented in figure 4.8.

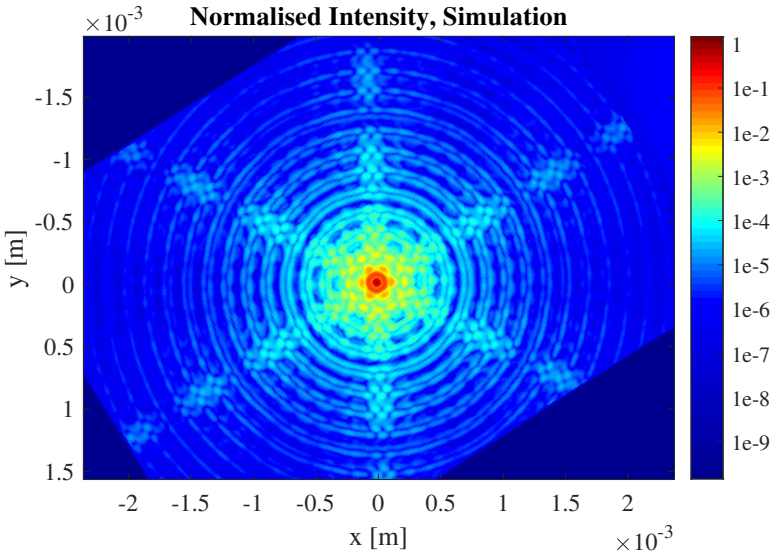

Figure 4.7: The simulated normalised PSF of the Schwarzschild objective. The odd edge effects observed are due to the image being rotated as to align with the measured PSF.

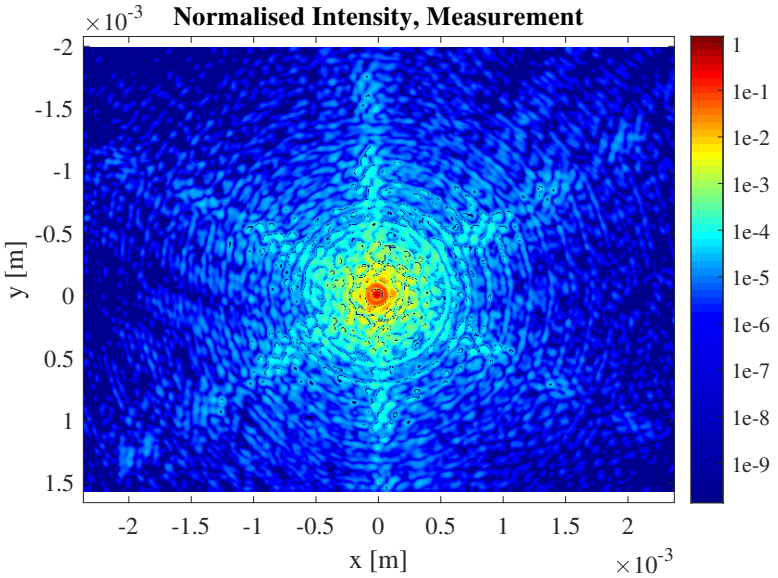

Figure 4.8: The measured normalised PSF* of setup B in figure 3.1 for a 15X Schwarzschild objective prototype.

The measured PSF* was merged from images obtained for exposure times $\tau = [1, 10, 100; 10^*, 100^*]$ ms. The *-marked times indicate a different tilt of the reflective

collimator as to allow more light into the fiber. The sampling distance is $a = 4.714\,\mu\text{m}$ and the rest of the simulation parameters are found in table B.1 in appendix B.2.

Looking at figure 4.7 and 4.8 we do see a strong resemblance between them, though the measured pattern is more noisy and slightly distorted. If one were to observe a cross sectional comparison of the two images the correspondence between simulation and experiment would not be as satisfying as for the annular aperture test. There are several reasons. In this setup the Schwarzschild and magnifying objectives are not connected which requires the magnifying objective to be aligned and focused to minimise the spot size of the PSF of the system. The focusing was done manually using a translation stage with sub mm increments. When out of focus, the three diffraction spikes do not pass through the centre of the focused spot, this was used for manual alignment and there is thus an inherent source of error. Furthermore, the peak intensities of measurement and simulation do not coincide. This due to the $\tau = 1\,\text{ms}$ image being captured at saturated peak intensity, but the possible defocusing is also a reason for decreased peak intensity. A manual scaling was used to fit the data to simulation. Moreover, to fit the data in the lateral dimensions a magnifying factor of the imaging system plus magnification objective had to be chosen as $M = 43.9$ (not $M = 40$). The simulated intensity also had to be rotated manually to fit the measured intensity. Matlab's image register would not converge on a correct rotation due to the noisy data. There are thus many sources of errors when considering the point to point correspondence in intensity. Due to the short wavelength of the light the interference changes rapidly over short distances and may vary immensely to small fluctuations and errors. Though the measured PSF* and the simulated PSF do not coincide perfectly, the general similarity is evident and it is clear that for the purpose of measuring and mitigating the six observed diffraction spikes, the method will suffice.

As an additional note, the relative intensity error of the scalar approximation can in this system be calculated as $\Delta I_{\text{scalar}} = \sin^2(\theta_2) = 0.106$. This is a quite small error. Moreover, the imaged field on the FPA is further aligned due to the long focal length of the tube lens. This will yield better agreement with the numerical method than if the PSF had been measured directly in the focal plane.

5

Spider vane design

In order to minimise unwanted diffraction in the Schwarzschild objective, which is the aim of this project, the PSF dependence on spider vane design needs to be investigated.

This chapter outlines the search for a spider vane design that reduces the intensity spikes seen in the diffraction pattern for the conventional straight support structure, see figure 4.5 for reference. Based on the theory from Chapter 2 and simulations using the method from Chapter 4, a number of different designs are considered. From this selection of spider designs one is recognised as most suited for the application and further optimised with respect to a set of different image quality criteria. Optional designs that compensate Gaussian input fields are also covered briefly.

5.1 Initial approach

While the spider vane design obviously needs to be altered from the original design in the purpose of reducing the intensity spikes, the other qualities of the objective need to remain. Clearly, the objective's operational aspects should not be altered, meaning that all device parameters, except for the supports connecting the barrel and the secondary mirror, are locked. The freedom of design thus only covers the shape of the vanes in the area bounded by the barrel (see R_i in figure 4.5) and the secondary mirror (see r_i in figure 4.5). Furthermore, it is required that the vane design is able to provide proper support to the mirror, hence a minimum vane width w and thickness t is required. With these aspects considered the goal is to find a design that optimises the PSF with regard to spike intensity and other image quality criteria.

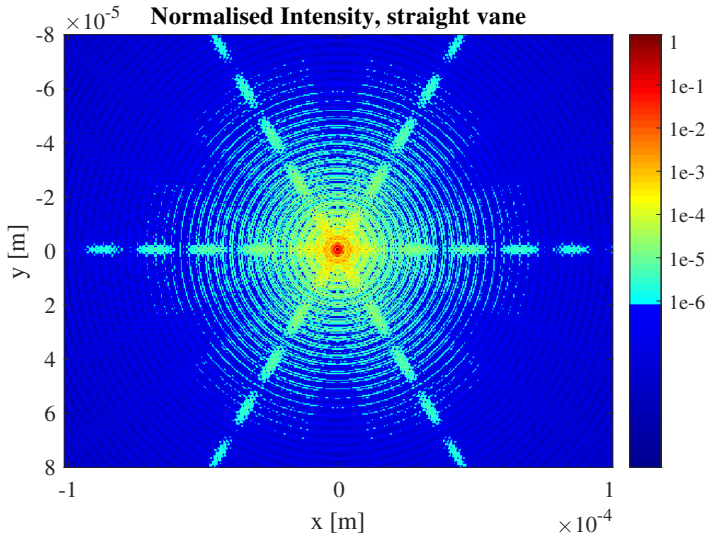

Figure 5.1: The intensity pattern obtained in the focal plane from the starting aperture in figure 4.5. Simulation parameters are found in table B.1 in appendix B.2.

To understand the origin of the intensity spikes, consider figure 5.1. It shows the simulated diffraction pattern from a straight spider vane aperture as shown in figure 4.5. From section 4.1 we recall that the PSF of the objective was approximately proportional to the fourier transform of the aperture function. With this in mind we recognise the PSF in figure 5.1 as the diffraction pattern from the superposition of rectangular and circular apertures that constitute the straight vane, see figure 5.2.

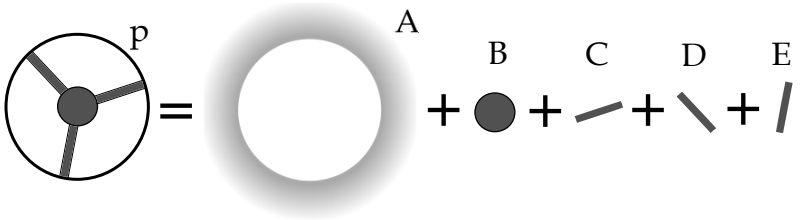

Figure 5.2: A decomposition of the aperture function into its elementary parts.

Thanks to the linear property of the fourier transform we can decompose the aperture function into its elementary components as is visualised in figure 5.2 and take the fourier transform of each component separately. The output field is then proportional to the sum of the fourier transforms of the individual components A, B, C, D, E.

The fourier transforms of these elementary aperture functions were described in section 2.3.2. In the case of a blocking aperture, as for B-E, the aperture function becomes $p_{\text{block}} = 1 - p_{\text{transmit}}$. However when a blocking aperture is added to an already transmitting area the 1 is omitted. From this it is clear that the diffracted field of the aperture and its complement relate as in (5.1) which is known as Babinet's principle[16].

$$E_{\text{transmit}} = -E_{\text{block}} \tag{5.1}$$

Looking at figure 5.1 we recognise the six diffraction spikes as the diffraction against the arm width w for the three arms, see (2.11), and the circular pattern is described by the magnitude squared E-field in (2.13) (recall figure 2.5). The slightly darker bands between the high intensity spikes are likely caused by destructive interference between the arm length diffraction $l = R_i - r_i$ and the circular aperture diffraction. One could imagine the diffraction against the arm and complement of the arm, located on the opposite side of B, to cancel out according to (5.1). A further thought would be to utilise the field canceling between transmitting and blocking apertures to remove the intensity spikes that impair the PSF. A quick analysis will however show that such a geometry is impossible, see derivation in appendix A.4.

Other approaches to field cancellation, such as wavelength scaled metasurface structures are feasible for certain types of applications[20] but would in the context of this work not only break the achromatic quality of the objective but also infer an immense increase of manufacture complexity. An approach that instead focuses on spreading the intensity spikes, that does not depend on wavelength scaled interference effects, is the idea of curved spider vanes[1]. The idea of curved vanes has already been investigated[1, 2], and its implementation is common among amateur telescope hobbyists [10]. Seemingly inspired by their use in reflective telescopes they have also seen an implementation in reflective microscope objectives, see [21]. The implementation in [21] does, however, not consider a number of effects that are investigated in this work and the consequence is further briefly discussed in section 6.2.

The reasoning behind the advantage of curved vanes on diffraction is simple, consider figure 5.3.

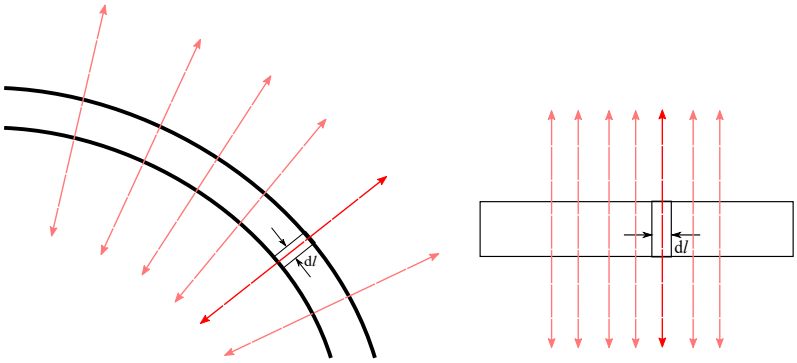

Figure 5.3: Diffraction against single differential lengths of the spider arms (diffracted light illustrated by red lines). Usage of straight arms accumulates all diffracted light in the same direction and position whilst a curved arm spread the light over a larger angle.

Theoretically one can view each differential length of the spider arm as a diffracting element. Using curved arms one can thus spread the diffracted light across a larger set of angles which will reduce the high intensity spikes, though whilst also

decreasing overall contrast. To achieve a complete homogeneous spread the arc angle total, subtended by the arms, should sum to π radians (a semicircle) or $m\pi$ radians where $m \in \mathbf{N}$, $m > 0$. In the case of three arms, each arm would subtend an arc angle of $\pi/3$ radians with each "cross-arm" direction unique. Such a spider geometry is shown in figure 5.4. Still, with these constraints there are a number of possibilities in the form of the number of spider arms and the integer m that determines the arc angle of each vane.

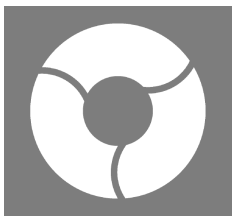

Figure 5.4: A spider mount structure using three $\pi/3$ radian curved arms.

We are already at this point able to draw a couple of conclusions. First, an increased number of arms will add stability to the structure but at the same time increase the total obscuration of the objective, that is, the blocking area will grow. It is therefore of interest to use few arms, however, 2 arms at opposite sides are unable to uniquely span π radians for $m = 1$ meaning one would need minimum $m = 2$. Since a larger m would imply a larger arc angle and thus also a larger obscuration it is of interest to keep to small m if possible. It is therefore a convenient choice to stick with 3 arms and an integer $m = 1$ for reducing the spikes at a low cost in obscuration and for maintaining stability.

For an optical system with close to parallel ray trajectories it is sufficient to employ the curved vanes aperture as visualised in figure 5.4 seen along the optic axis. For the Schwarzschild system, where the starting surface is taken as a spherical cap in the method of propagation, this aperture need to be remapped to fit the focused rays. By doing so we obtain the aperture plotted in figure 5.5. Simulating the PSF for the Schwarzschild system, using this apeture, produces the result in figure 5.6. The dimensions for the planar curved aperture as well as for the spherical curved aperture are presented in appendix A.3.

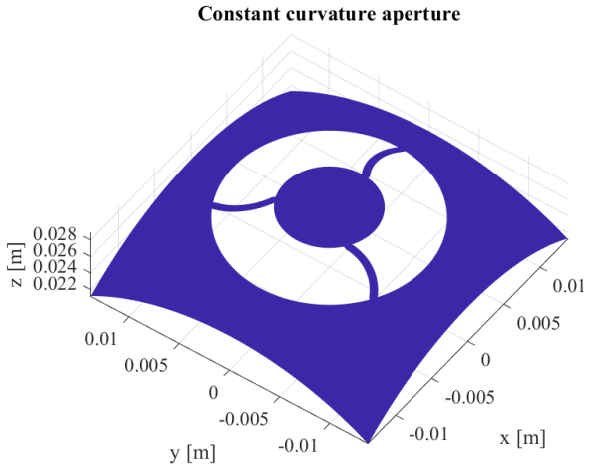

Figure 5.5: A spherical curved vane using three $\pi/3$ radian curved arms.

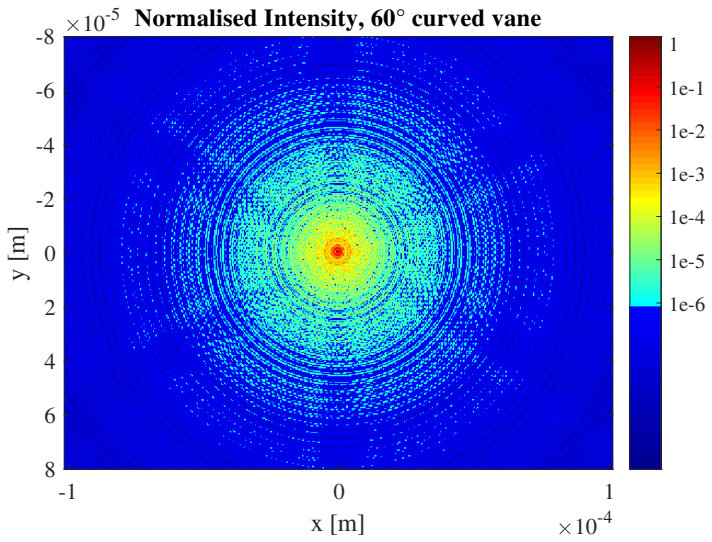

Figure 5.6: Calculated intensity pattern for the aperture shown in figure 5.5. The input field is taken as a constant, as should be for evaluating the PSF. Simulation parameters are found in table B.1 in appendix B.2 except for $\theta_{\text{arc}} = \pi/3$.

A quick comparison between figures 5.1 and 5.6 suggests that curved vanes indeed help reducing the observed intensity spikes, although it appears that the intensity distribution obtained for arc angle $\theta_{\text{arc}} = \pi/3$ is not completely isotropic in direction. Six darker bands are seen stretching out from the center. Despite this effect the idea of using curved vanes appears promising for the aim of this work and it will be further studied and optimised in section 5.2.

But before that, returning to the principle, the reasoning visualised in figure 5.3 and the predictions on optimum arc angle rely on the fact that equal amount of optical intensity is incident on each differential arm element dl pointing in a unique direction. If it was not, more light would be diffracted against segments of the arms where the intensity is higher and for a constant curvature arm it would result in an inhomogeneous spread of intensity on the different angles. For achieving isotropic spread for a specific input field a specific arm geometry is required. For the special but common case of Gaussian amplitude distributed fields the requirements on arm geometry are studied in section 5.3.

In the light of this, the ultimate reason for the remapping of the planar aperture onto the spherical cap is the factor $1/\sqrt{\frac{1}{\lambda^2} - \nu_x^2 - \nu_y^2}$ from section 4.1. This factor causes the otherwise constant input field to grow outward, demanding that the aperture curvature increase further from the centre to compensate.

5.2 Constant curvature vanes

As mentioned above, for an infinity corrected system like the Schwarzschild objective, which assumes constant amplitude input fields the principle of constant curvature vanes should enable a complete isotropic spread of the intensity in the PSF. An arc

angle of $\pi/3$ radians was already simulated in figure 5.6 and did not show perfect isotropic spread despite the reasoning presented in the above section. To understand why this is, a series of simulations over different arc angles was performed. The result is visualised in the format of the video below.

The video shows the aperture function, the azimuthal intensity variation of half the PSF ϕ: $0 \rightarrow \pi$ and the PSF, for both the complete spider vane aperture but also the curved arms only. The mentioned azimuthal intensity variation is in fact the directional power P_θ presented in the coming section 5.2.1 and normalised as $P_\theta(n, \theta_{\text{arc}})/\text{Max}\{P_\theta(n, 0)\}|_n$. The active θ_{arc} is stated in the label of the directional power plot.

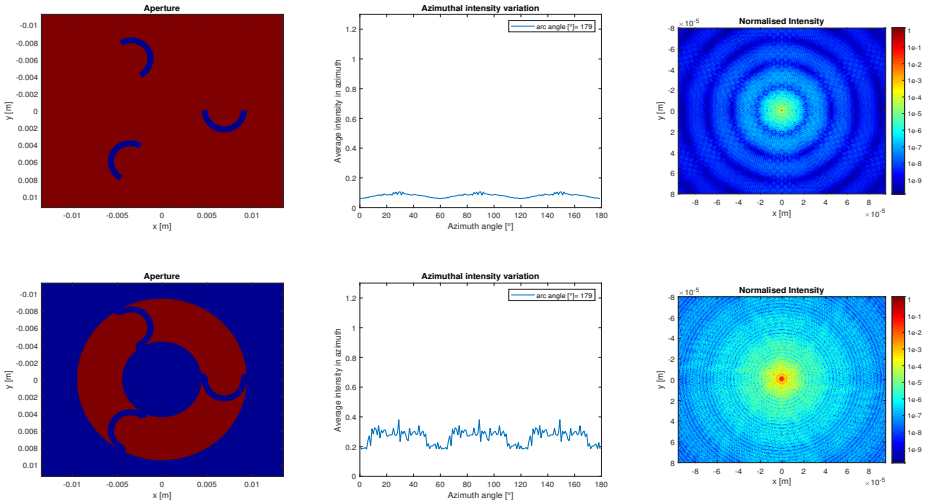

Simulation parameters are found in table B.1 in appendix B.2 except $\theta_{\text{arc}} = [0, \pi]$, and $N = 5000$.

The series of simulations shows an initial rapid decay of the intensity spikes with respect to θ_{arc} for both apertures. The complete aperture appears more noisy which is an effect of the rapid interference between annular and rectangular diffraction. The case for only arms is smoother and as the peaks decay they seem to fringe out and create small bumps at the edges of the broadened peak. This is also visible in the PSF for both apertures and is likely due to the following: While diffraction against neighbouring differential arm elements is identical along the arm the case differs when we reach the edges. Here, there edge element dl_k of inclination $kd\theta$ has no consecutive neighbour. The next element dl_{k+1} of inclination $(k+1)d\theta$ is located at the edge of another arm and since they are separated in space the light diffracted against them will not compose the same interference as for neighbouring elements. For this reason the spikes do not completely smear out at $\pi/3$ radians and it is not before $\theta_{\text{arc}} \approx 70°$ that the pattern appears fully averaged out.

Another interesting observation is the difference between azimuthal intensity variations at $\theta_{\text{arc}} = 0$ between the both apertures. Between the peaks the only arms-aperture exhibit small bumps while the complete aperture case has valleys. The bumps are easily explained from the rectangular diffraction pattern discussed in 2.3.2 while the valleys confirm our previous suspicion of the rectangular and annular diffraction patterns to locally cancel out. This might as well affect the optimum

arc angle for homogeneous intensity spread.

With this brief analysis on the PSF's θ_{arc} dependence to enhance our understanding we proceed with concretisising the intensity spread numerically in the following section, 5.2.1.

5.2.1 Angular intensity distribution

To determine the exact arc angle θ_{arc} that produces the most isotropic PSF and for the purpose of later optimisation against image quality criteria, a measure of the spread needs to be developed. To help describe the azimuthal intensity variation we define a directional power as in (5.2).

$$P_\theta(n, \theta_{arc}) = \int_{(n-1)\Delta\theta}^{n\Delta\theta} \int_{r_m}^{r_M} I_n(r, n, \theta_{arc}) \Theta(I_n) W(r) r d\theta dr \tag{5.2}$$

Here $I_n = \text{PSF}/\max\{\text{PSF}\}$ is the normalised intensity distribution evaluated in the focal plane, θ_{arc} is the arm arc angle for which the PSF is calculated, $\Theta(I_n) = 1$ if $I_n \geq I_{\min}$, else 0 and the other parameters are visualised in figure 5.7. To emphasise the diffractive effects caused by the arms and to compensate for the radial dependence of the ideal annular pattern (the obtained case if the arms were removed) we will apply a weighting function $W(r)$ to the calculated intensity in the focal plane. The envelope to the function $J_1(t)$ is roughly proportional to $1/\sqrt{r}$, see section 2.3.2, and so the envelope to the annular diffraction intensity can be approximated to be $I_{ea} \approx I_0/r^3$ where I_0 is a constant. To evaluate the intensity relative the ideal intensity at each position r away from the centre we thus choose the weighting function as $W(r) = Wr^3$ where W $[\text{m}^{-3}]$ is a constant. The use of $I_{\min}$ ensures that intensity values below a certain threshold intensity are neglected in the calculation. Due to a limited intensity resolution and dynamic range in most light sensing systems it is reasonable to make this omission since this light would not be imaged in a practical system regardless. It is also valuable to carry through this omission since the diffraction from a straight spider arm is given by $\text{sinc}^2 r \propto r^{-2}$ which decreases at a much slower rate than r^{-3}. Spike values located further out from the centre (large r) will thus be weighted heavier ($\propto r$) which is not necessarily the intention when a sensing system may not detect them. The use of $I_{\min}$ thus alleviates this issue.

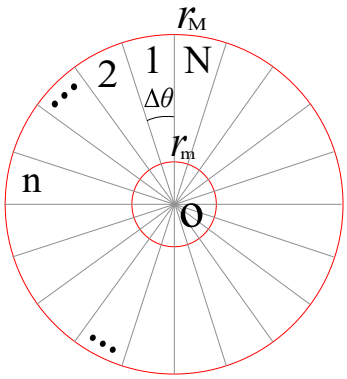

Figure 5.7: A geometric visualisation of the boundaries of the directional integrated power P_θ. The centre "O" is located at the peak intensity. Note that $\Delta\theta = 2\pi/N$.

Furthermore, the use of r_M makes sure we consider intensities within the correctly imaged circle only ($r_M \leq D_{\text{image}}/2$), as given by the window size requirement. r_m is used in cases where the large central peak needs to be omitted.

It is now straight forward to calculate the mean directional power, (5.3):

$$\bar{P}_\theta(\theta_{\text{arc}}) = \frac{\sum_{n=1}^{N} P_\theta(n, \theta_{\text{arc}})}{N} \tag{5.3}$$

The difference from the mean for each sector is then, (5.4):

$$\Delta P(n, \theta_{\text{arc}}) = P_\theta(n, \theta_{\text{arc}}) - \bar{P}_\theta(\theta_{\text{arc}}) \tag{5.4}$$

We can now define the normalised spike magnitude, (5.5):

$$S_M(\theta_{\text{arc}}) = \max\{\Delta P(n, \theta_{\text{arc}})\}|_n / \bar{P}_\theta(\theta_{\text{arc}}) \tag{5.5}$$

as well as the normalised azimuthal standard deviation, (5.6):

$$\sigma_\theta(\theta_{arc}) = \frac{\sqrt{\frac{1}{N}\sum_{n=1}^{N} |\Delta P(n, \theta_{\text{arc}})|^2}}{\bar{P}_\theta(\theta_{\text{arc}})} \tag{5.6}$$

Here, S_M is a measure of the largest intensity in any given direction and thus effectively describes the magnitude of the intensity spike. σ_θ on the other hand describes the general power deviation from the azimuthal mean and thus effectively becomes a measure of isotropic spread. The most homogeneous intensity spread is obtained when σ_θ reaches a minimum, ideally zero. The reason for the normalisation against the mean is for considering the current amount of power present in the PSF since it may vary with respect to input parameters such as θ_{arc}.

In figure 5.8 σ_θ is plotted against θ_{arc} for the only arm-aperture and full aperture simulation. For the only arm-case we note that a first minimum is reached for an arc angle around 67°, slightly larger than $\pi/3$ which was originally anticipated. Meanwhile the full aperture-case shows an extended minimum between $65° - 95°$.

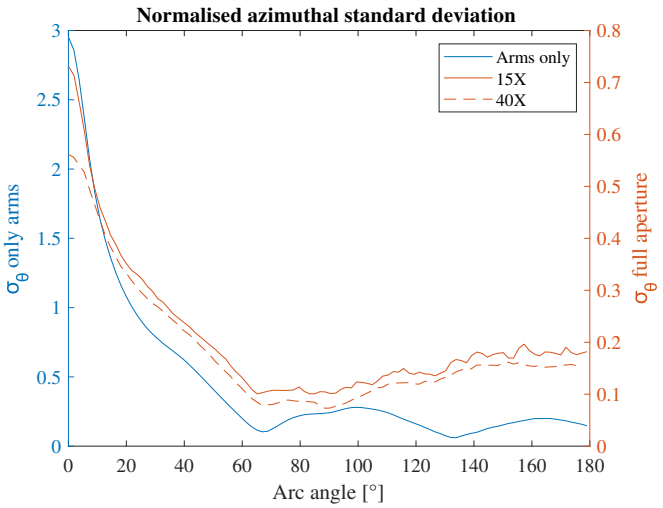

Figure 5.8: Plotted here is the normalised azimuthal standard deviation σ_θ as function of arc for the only arm-simulation (blue) and full aperture simulation (orange) for both objectives. The input field is taken as a constant, as should be for evaluating the PSF. For both 15X and 40X simulation parameters are found in table B.1 in appendix B.2 except $N = 5000$, $\theta_{\text{arc}} = [0, \pi]$, $r_m = 0$, $r_M = D_{\text{image}}/2$, $I_{\text{min}} = 1 \cdot 10^{-6}$ for full aperture simulation and $I_{\text{min}} = 0$ for only arms.

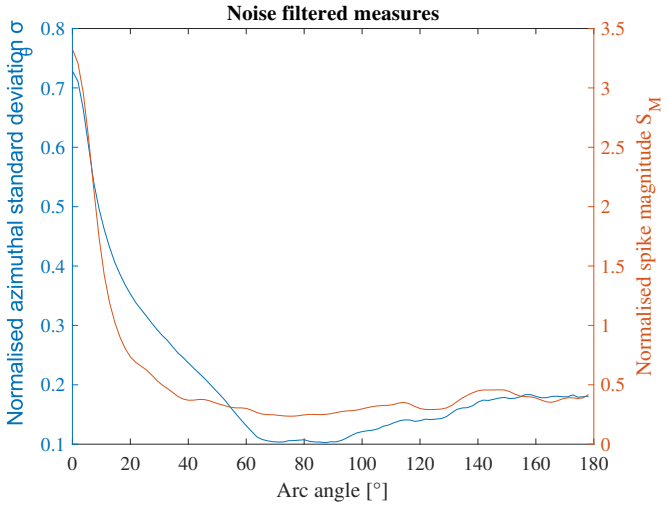

Figure 5.9: Plotted here is the noise filtered normalised azimuthal standard deviation σ_θ and normalised spike magnitude S_M as function of arc angle θ_{arc} for the full aperture 15X objective. The simulation parameters used for obtaining these results are found in table B.1 in appendix B.2 except $N = 5000$, $w = p^{(1)}$, $\theta_{\text{arc}} = [0, \pi]$, $r = p^{(2)}$, $\lambda = p^{(3)}$, $r_m = 0$, $r_M = d_{\text{image}}/2$, $I_{\text{min}} = 1 \cdot 10^{-6}$. The sweep parameters $p^{(1)}$, $p^{(2)}$ and $p^{(3)}$ are given in table A.1 in appendix A.5. For sweep over λ different values of a and D_{image} were used for each wavelength.

As in the video of section 5.2, the contrast between smoothness of the only arm-simulation and the full aperture-simulation manifests itself also here considering σ_θ as a result of interference. The fluctuations in σ_θ for the full aperture-case are a problem when one tries to determine the global minimum. Since the interference changes rapidly with small scale variations in aperture, such caused by e.g. manufacturing errors in a practical case, simulation sweeps over the affecting system parameters was done to filter out this interference noise. Simulation data from sweeps of parameters: inner circular aperture radii r_i, arm width w and wavelength λ was used to calculate interference filtered versions of S_M and σ_θ which are plotted in figure 5.9. The exact procedure describing how these filtered values are obtained is presented in appendix A.5.

According to figure 5.9 the optimum arc angle for achieving isotropic intensity lies in the range of $70° - 90°$ which corresponds nicely to the smallest intensity spikes as well from observing S_M. Generally, as can also be seen in the video of the previous section 5.2, the intensity spikes diminish quickly initially with increasing θ_{arc} and eventually relax to minimum values at $\theta_{\text{arc}} = 70° - 90°$ before subtly increasing again.

Interesting to note is the difference in the shape of σ_θ between the full aperture and only arm-cases in that the first exhibits a broad range of θ_{arc} for where it is minimum whilst for the second this only occurs at two distinct points in θ_{arc}. The reason for the extended minimum for the full aperture, from watching the previous video, is the continuous compensation for the valleys that had been present from the start. Judging from these figures, 5.8 and 5.9, we can draw two important conclusions (for the given system parameters): that an arc angle of $\approx 67°$ produces

a homogeneous spread of the original intensity spikes due to multi-arm interference as discussed previously, and that it requires an inhomogeneous spread of the initial intensity spikes to compensate for the otherwise inhomogeneous azimuthal intensity variation in order to achieve a total isotropic pattern. In this case $\theta_{\text{arc}} = 70° - 90°$ is required to compensate for the intensity valleys originating from destructive interference between arm length and circular diffraction patterns.

This observation also explains why there is no minimum in σ_θ present at arc angles slightly above 120° for the full aperture simulation while we see a minimum in σ_θ at an angle $\theta_{\text{arc}} = 2 \cdot 67° = 134°$ for the only arm simulation in figure 5.8 which would correspond to an integer $m = 2$ from the theory presented in the beginning of this chapter. Effectively, the azimuthally propagating intensity bumps at the spike's ends seen in the video are used to fill in the valleys. If the arms are made to arc another 70° these bumps are further diminished and will not fully compensate the valleys, hence $m > 1$ will produce worse results in this regard.

To gain an understanding for the effect of variation in r_i, w and λ on the PSF and the azimuthal intensity spread consider the parameter sweeps in figures 5.10a, 5.10b and 5.11.

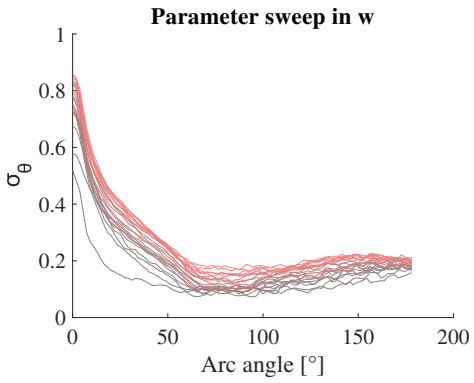

(a) Simulated σ_θ for parameter sweep in arm width $w \in [0.05, 2]$ mm. Curves of increasing red colour correspond to increasing value of w.

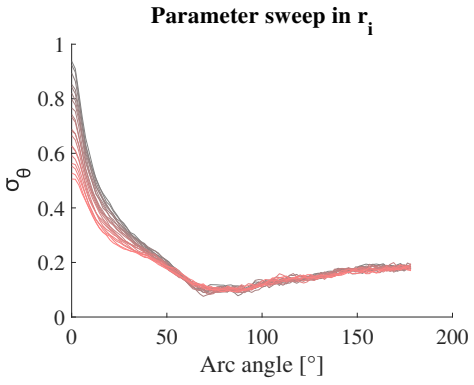

(b) Simulated σ_θ for parameter sweep in central obscuration radii $r \in [3.5, 5.4]$ mm. Curves of increasing red colour correspond to increasing value of r.

Figure 5.10

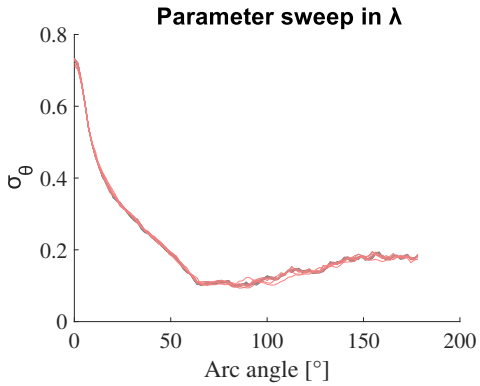

Figure 5.11: Simulated σ_θ for parameter sweep in wavelength $\lambda \in [0.2, 5]$ µm. Curves of increasing red colour correspond to increasing value of λ.

Figure 5.10a shows that the same flat minimum in σ_θ is present for what would seem all simulated widths w, although at different offsets in σ_θ. The increasing minimum value with arm width w compares nicely to the discussion in [1]. If the central intensity peak decreases proportionally to the arm area squared and the mean directional power decreases only proportionally to the area then the normalised mean power will increase proportionally to the area. From section 2.3.2 we recall that the intensity spike is proportional to the arm area squared which leads to σ_θ being proportional to the area $\propto w$. Why the trend persists for increasing arc angle may be due to a more pronounced interference effect from the wider arms effectively increasing the spread measure.

Although difficult to observe in the plot one may note that the flat minimum is reached for smaller θ_{arc} approaching $\pi/3$ for smaller widths. To return to the preceding theoretical optimum arc angle anticipation, a thinner arm make the differential rectangular element-approximation more correct in the sense that too wide arms compared to tight arc angles shape the arm closer to a circle sector than a rod. The fact that the flat minimum range is preserved shows that the intensity spikes and valleys of the azimuthal intensity variation plots in the video scale proportionally, which they should considering they originate from the same geometry now varying in w.

Figure 5.10b in contrast show an initial decrease in σ_θ with increasing inner obscuration radii r_i. This does however make sense since now the arm area decreases implying the spike intensity decreases proportional to the arm area squared. The mean power will however increase with increasing r_i like what was described for the previous case in w. Furthermore, we still find a flat minimum though it appears that its width in θ_{arc} has shrunk slightly.

The sweep in λ, plotted in figure 5.11 σ_θ show to be close to independent to wavelength other than small scale fluctuations. This is an interesting result since it does not only show that it suits an achromatic system well but also because the physical system parameters, while keeping their mutual proportions, can be scaled up or down in dimensions without affecting the performance, at least for the tested range of wavelengths.

5.2.2 Effects on the imaging system

The previous section's investigation on the angular intensity distribution established a deeper understanding on the isotropic spread versus arc angle, however, there are other effects the curved vanes impose on the Schwarzschild imaging system. Here we introduce a couple of image quality criteria and investigate their relation to arc angle θ_{arc} for use in later optimisation.

First, one evident effect caused by the arcing arms is the increased arm area, assuming constant width w, which will increase the obscuration of light travelling through the system. A direct consequence is that the amount of light transmitted will decrease. Obscuration will therefore be used as an image quality criteria and is defined as the area of the non-transmissive part of the aperture, normalised to the case of straight vanes, (5.7):

$$Q_o = \frac{\iint |1 - p(x, y, \theta_{\text{arc}})| dxdy}{\iint |1 - p(x, y, 0)| dxdy} \tag{5.7}$$

Secondly, we shall define the Strehl ratio as the peak intensity of the PSF normalised to the peak intensity of the PSF produced by a straight vane aperture, (5.8):

$$Q_s = \frac{\text{Max}\{\text{PSF}(\theta_{\text{arc}})\}}{\text{Max}\{\text{PSF}(\theta_{\text{arc}} = 0)\}} \tag{5.8}$$

The Strehl ratio is a direct measure of the amount of power that hits the focused spot, which should be all of it for an ideal system. Moreover we can qualify the system from its spot size, that is, the blur size radius ρ_s of a focused spot, (5.9):

$$Q_{\rho_s} = \frac{\frac{1}{2\pi} \int_\theta \text{Min}\{r(I_n(\theta, \theta_{\text{arc}}) = 1 \cdot 10^{-3})\} d\theta}{\frac{1}{2\pi} \int_\theta \text{Min}\{r(I_n(\theta, \theta_{\text{arc}} = 0) = 1 \cdot 10^{-3})\} d\theta} \tag{5.9}$$

What (5.9) essentially states is the average radius in direction for which the PSF has dropped to $1 \cdot 10^{-3}$ of its peak value. Conventionally ρ_s is the distance from the peak intensity to the first minimum and the reason for an altered definition here is for simpler numerical evaluation of the spot size. Finally we define the contrast as, (5.10):

$$Q_c = \frac{\iint_{r \leq \rho_s(\theta_{\text{arc}})} \text{PSF}(\theta_{\text{arc}}) dxdy}{\iint_{r > \rho_s(\theta_{\text{arc}})} \text{PSF}(\theta_{\text{arc}}) dxdy} \Bigg/ \frac{\iint_{r \leq \rho_s(\theta_{\text{arc}}=0)} \text{PSF}(\theta_{\text{arc}} = 0) dxdy}{\iint_{r > \rho_s(\theta_{\text{arc}}=0)} \text{PSF}(\theta_{\text{arc}} = 0) dxdy} \tag{5.10}$$

In words, the contrast is the average intensity found within the spot size relative to the average intensity found outside, normalised to the straight vane case. For all image quality values, the normalisation against the straight vane case provides a direct measure of improvement or degradation relative to the original design. Performing calculations of these image quality values for a simulation over θ_{arc} produced the result of figure 5.12.

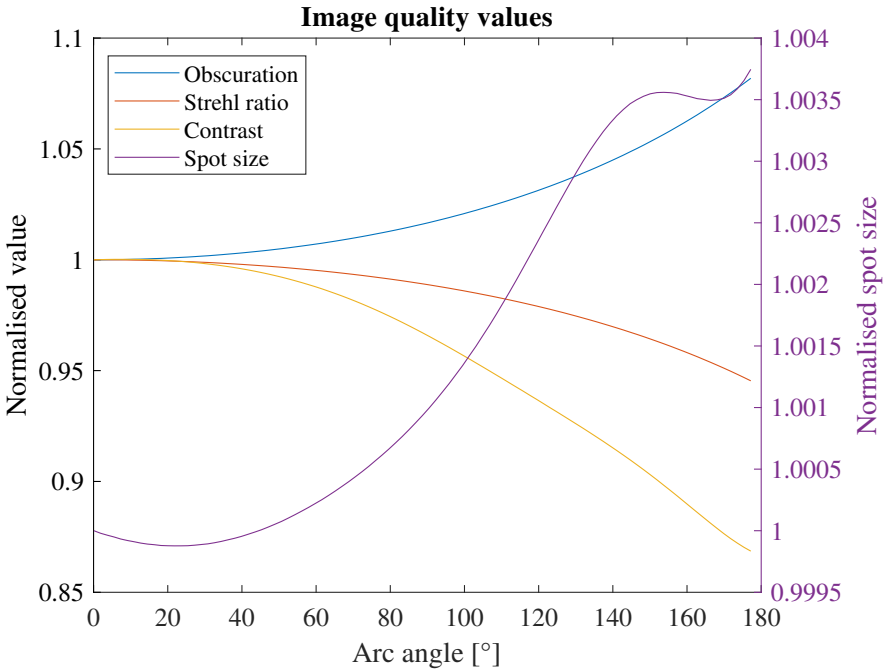

Figure 5.12: The plot shows the image quality values presented in section 5.2.2 as a function of arc angle θ_{arc}.For the left y-axis the obscuration (blue), Strehl ratio (orange) and contrast (yellow) are given. The spot size is plotted toward the right y-axis in purple. Simulation parameters are found in table B.1 in appendix B.2 except $N = 5000$, $\theta_{\text{arc}} = [0, \pi]$, $r_m = 0$, $r_M = d_{\text{image}}/2$, $I_{\text{min}} = 1 \cdot 10^{-6}$.

What figure 5.12 shows is that all of the concerned image quality values are degraded with increasing arc angle. However, the degradation appears small and for the spot size negligible, over the range of θ_{arc} which produced a minimum in σ_θ according to the previous section. For $\theta_{\text{arc}} = 80°$ the increase in obscuration is approximately 2%, the decrease in Strehl ratio 1% and in contrast about 3%, magnitudes that may be affordable in a trade-off against an isotropic PSF.

5.2.2.1 The Modulation transfer function

The effect the curved vanes has on the modulation transfer function of the system is also of interest to investigate. The MTF for the curved vanes of $\theta_{\text{arc}} = 70°$ is plotted in figure 5.13a.

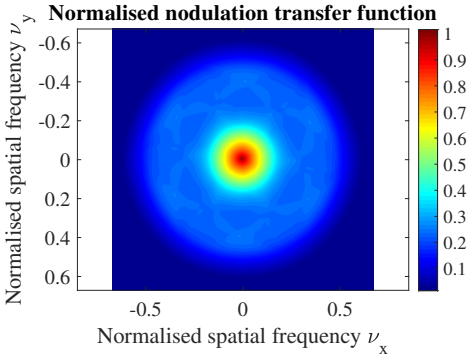

(a) The MTF of the curved vane aperture for $\theta_{\text{arc}} = 70°$ normalised to the maximum value of the MTF evaluated for straight vanes, $\theta_{\text{arc}} = 0°$. The normalisation in spatial frequency is made against the largest spatial frequency possible: $\nu_{\text{max}} = 1/\lambda$. Simulation parameters are found in table B.1 in appendix B.2.

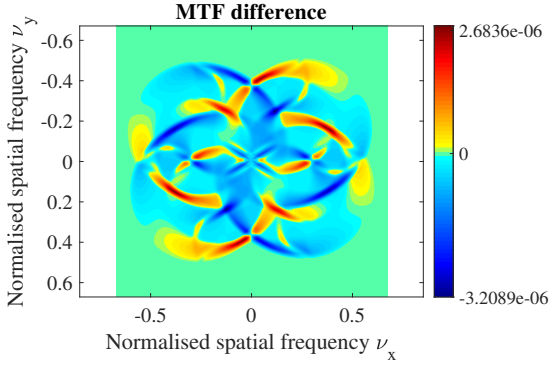

(b) Presented here is the difference between the curved vane aperture MTF for $\theta_{\text{arc}} = 70°$ and the straight vane aperture MTF ($\theta_{\text{arc}} = 0°$), normalised to the maximum value of the MTF evaluated for straight vanes. The normalisation in spatial frequency is made against the largest spatial frequency possible: $\nu_{\text{max}} = 1/\lambda$. Simulation parameters are found in table B.1 in appendix B.2

Figure 5.13

The change in MTF from the straight vane case is visualised in figure 5.13b where the difference in MTF between the curved and straight vane apertures is plotted, $\Delta\text{MTF} = \text{MTF}_{\text{curved}} - \text{MTF}_{\text{straight}}$.

Note the small values of the difference magnitude which compares to the peak value as 10^{-6} implying that the effective change between the two MTFs is in principle negligible. The plot does show however that the transmittance between spatial frequencies is shifted between one another due to the curving arms. A general decrease in MTF value may also be perceived and is further evident in the radially averaged MTF plot in figure 5.14. Here, the result is obtained as the average MTF value at each distance ν from the centre and each curve is normalised to its maximum value. The decrease between straight and curved vane MTF is very small and due to the increasing arm area with arc angle, causing a smaller throughput of all spatial frequencies.

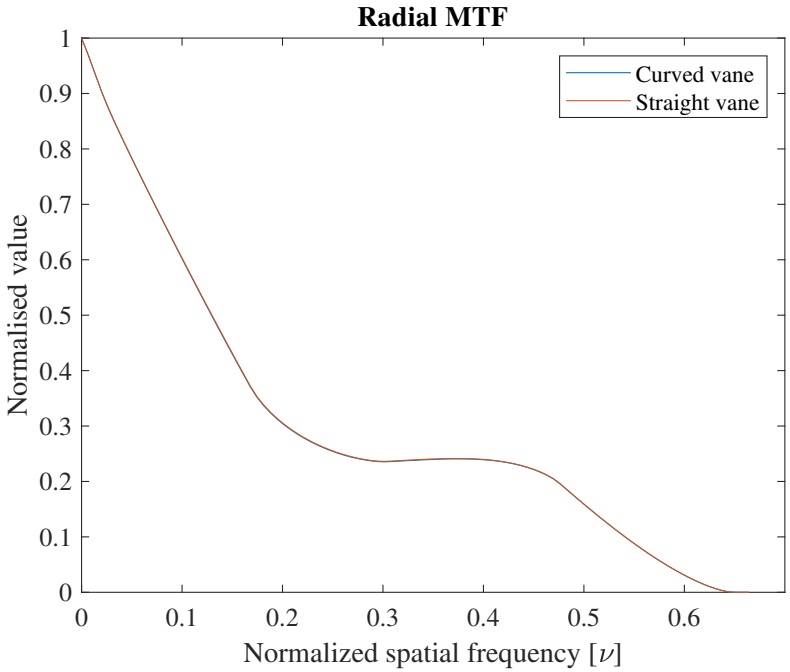

Figure 5.14: Here the azimuthally averaged MTFs are plotted for the curved vane aperture at $\theta_{\text{arc}} = 70°$ and the straight vane aperture, each normalised to their respective maximum values. The normalisation in spatial frequency is made in respect to the largest spatial frequency possible: $\nu_{\text{max}} = 1/\lambda$. Simulation parameters are found in table B.1 in appendix B.2.

To summarise the investigation on the MTF it can be concluded that the effect of the curved vanes on the MTF is negligible. The small general degradation is due to increasing obscuration area, an effect already accounted for in the quality measures derived in section 5.2.2.

5.2.3 Optimisation

It has already been established what arc angles θ_{arc} produce the most isotropic PSF but the question remains whether this θ_{arc} optimises the total device performance, considering also other image quality values. To answer this the problem was optimised in θ_{arc} using a total cost function structured from the individual image quality values. To account for the benefit of isotropic PSF two additional quality values are introduced as, (5.11) and (5.12):

$$Q_{\sigma_\theta} = \frac{\sigma_\theta(\theta_{\text{arc}})}{\sigma_\theta(\theta_{\text{arc}} = 0)} \tag{5.11}$$

$$Q_{S_M} = \frac{S_M(\theta_{\text{arc}})}{S_M(\theta_{\text{arc}} = 0)} \tag{5.12}$$

Emphasised again, the normalisation against the straight vane case provides a direct measure of improvement or degradation relative to the original design. This

normalisation thus effectively equalises the relative improvement or degradation between quality values and will further determine the expectancy-value of the coming statistical optimisation study. The total cost is written as, (5.13):

$$TC(\theta_{\text{arc}}) = w_o Q_o - w_s Q_s + w_{\rho_s} Q_{\rho_s} - w_c Q_c + w_{\sigma_\theta} Q_{\sigma_\theta} + w_{S_M} Q_{S_M} \tag{5.13}$$

where the parameters w_x are weights for the individual quality values ($\sum_k w_k = 1$). A specific set of weights $w_{1,2..}$ represents a potential user preference. Depending on what use the Schwarzschild objective will have the different quality measures will matter differently. If one assigns random weights w_x to each of the quality values and minimises the total cost TC in arc angle θ_{arc} a total of 10^5 times the result in figure 5.15 is obtained. The randomisation is used to crudely model the realistic distribution of user preferences.

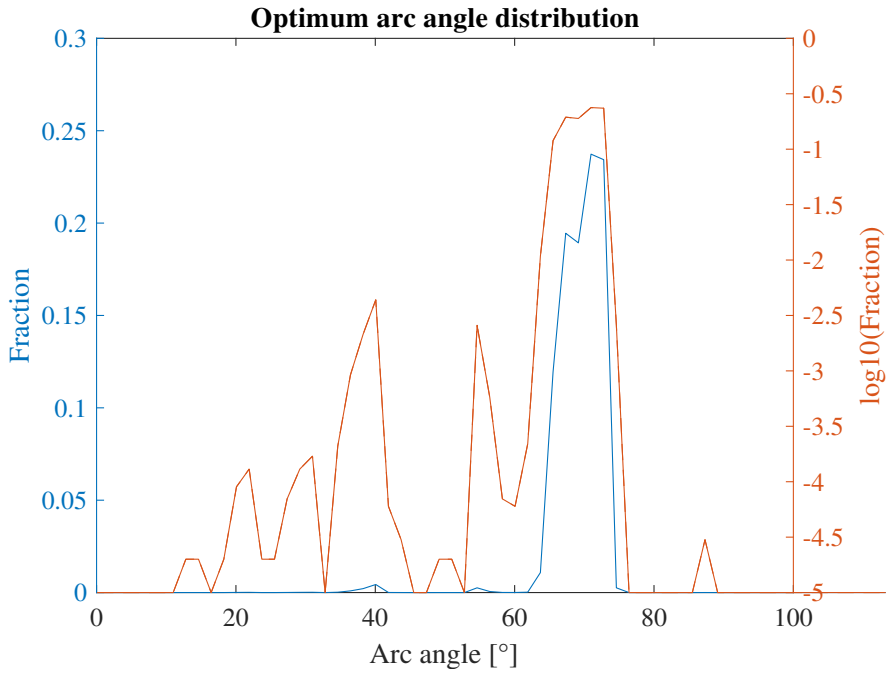

Figure 5.15: The distribution of optimal arc angles θ_{arc} for linear scale in blue and logarithmic in orange. Fraction states the number of times a specific θ_{arc} was evaluated optimal relative to the total number of cases $N_c = 10^5$. The sampled points in θ_{arc} are spaced as $\Delta\theta_{\text{arc}} = 1.8°$.

If all weights are set equal then TC returns an optimal $\theta_{\text{arc}} = 70°$ which matches the result in figure 5.15. Moreover, the number of optimal arc angles in the interval $60° < \theta_{\text{arc}} < 80°$ counts to $\approx 98.8\%$ of the total number of cases. This shows that, for the normalisation performed here, an arc angle of $\theta_{\text{arc}} = 70°$ optimises the entire system, which also matches that for obtaining isotropic PSF. It was already evident from figure 5.12 that the degradation of other quality values was small so the result comes as no surprise. If we reduce the total cost function to only contain Q_o and Q_{σ_θ}, two opposing quality values, then the ratio of weights w_o/w_{σ_θ} required for there to be a larger number of optimal arc angles below 60° is given by figure 5.16.

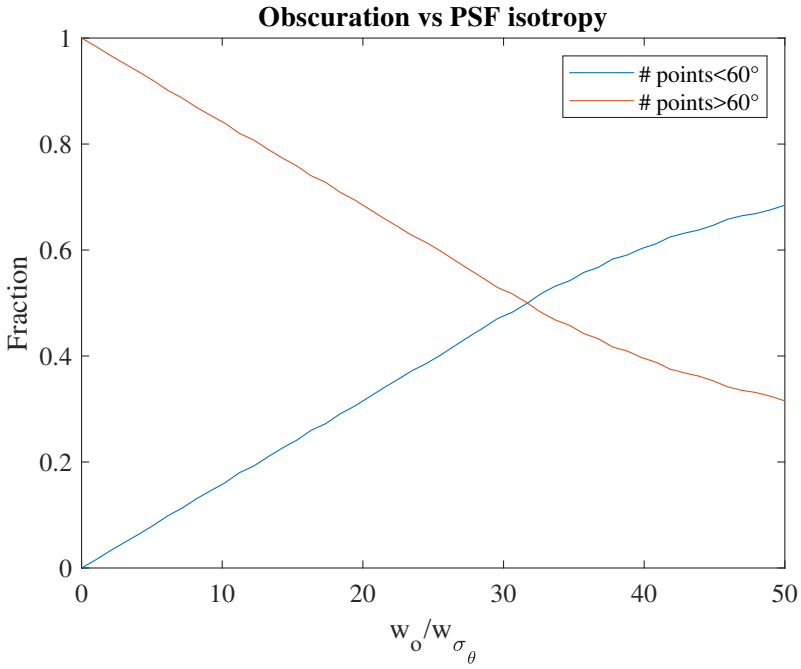

Figure 5.16: The relative number of optimal θ_{arc} less than 60° (blue) and greater than 60° (orange) for $TC = w_o Q_o + w_{\sigma_\theta} Q_{\sigma_\theta}$ as function of w_o/w_{σ_θ}.

If a user preference considers only obscuration and PSF isotropy as interesting quality measures they need to evaluate Q_0 about 30 times more important than Q_{σ_θ} for it to be more beneficial to have an arc angle $\theta_{\text{arc}} < 60°$ according to this result. There are of course situations where the intensity spikes in the PSF of the original design do not matter and in such case the use of curved vanes would only degrade the system performance. However, as is indicated by the optimisation study performed, it would appear that a majority of user preferences would benefit the most for an arc angle $\theta_{\text{arc}} \approx 70°$ taking all quality measures into aspect. Although the power cost and effect on environmental sustainability has not been explicitly evaluated it is accounted for in the obscuration and Strehl ratio values, though one can argue they should be weighted heavier. Even with that considered, the degradation appear marginal and does not alter our conclusion.

5.3 Gaussian vanes

The idea behind curved support structures originate from the idea of equally distributing the diffracted intensity per azimuthal angle as was mentioned previously. Intuitively we can state the following condition for this to occur, (5.14):

$$\text{const} = w\frac{dl}{d\theta}I(\mathbf{r}) \tag{5.14}$$

(5.14) states that the differential arm element area per subtended azimuthal angle $d\theta$ times the incident intensity needs to be constant. For this condition to be satisfied for a spatially varying intensity we must either allow a spatially varying

arm width $w = w(\mathbf{r})$ or a spatially varying arm curvature $\frac{dl}{d\theta} = \frac{dl}{d\theta}(\mathbf{r})$ or both. A varying arm width in regard to a minimum width for supporting the structure may result in impractical apertures, especially if the intensity changes over a large range. Moreover, a varying width causes a change in diffraction pattern, see (2.10), which contributes to a radial redistribution and thus an azimuthal dependence. With these things considered this solution appear less attractive. Varying the arm curvature may also seem impossible for certain intensities, however, if the intensity distribution is smooth and exhibits only a radial dependence, such as a Gaussian, then the use of spatially dependent arm curvature may suffice.

The Gaussian beam intensity is described as, (5.15):

$$I(\rho) = I_0 \exp\Big[-\frac{2\rho^2}{w_\rho^2} \Big] \tag{5.15}$$

In (5.15) we note an important parameter being the $1/e^2$-radius w_ρ which renders each Gaussian distribution unique. This implies that there will only be one vane structure that perfectly matches a given Gaussian distribution. In the case of the Schwarzschild objective, what we would ideally want is an aperture that accomplishes isotropic PSFs for a range of different input intensity distributions. It is clear that this will not be provided by the Gaussian aperture investigated here. For the purpose of verifying the truth behind (5.14) and for possible applications concerning Gaussian beams it is still of interest to study this matter.

Because of mathematical complications a close to flat starting field was considered instead of a spherical cap. System parameters are: $a = 1.28\,\mu\text{m}$, $r_i = r = 1.1\,\text{mm}$, $R_i = R = 2.8\,\text{mm}$, $\lambda = 543\,\text{nm}$, $N = 7000$, $D_{\text{image}} = 6\,\text{mm}$, $R_0 = 200\,\text{mm}$, $r_m = 0$, $r_M = D_{\text{image}}/2$, $w = 0.212\,\text{mm}$, $I_{\min} = 0$, $\theta_{\text{arc}} = 70°$. The choice of arc angle $\theta_{\text{arc}} = 70°$ is based on the assumption that it will generate an isotropic PSF like it had in the case for constant curvature vanes. For a rigorous study one should perform an additional analysis on optimal arc angle for gaussian vanes.

Figure 5.17: A Gaussian aperture for $w_\rho = \frac{r+R}{2}$.

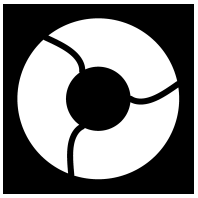

By setting $w_\rho = \frac{r+R}{2}$ and solving for $l(\mathbf{r})$ using (5.14) and (5.15) the aperture shape shown in figure 5.17 was generated. The procedure for calculating the arm shape $l(\mathbf{r})$ given a specific w_ρ is described in appendix A.6.

Using this aperture (calculated for compensating $w_\rho = 1.99$ mm) a series of simulations where the beam radius w_ρ is altered was performed. The result is visualised in the form of the video below, see the top row, where the normalised starting field $f_2 = f_1 p(\mathbf{r})$, the azimuthal intensity variation as well as the PSF is plotted. The current simulated w_ρ is stated in the legend of the azimuthal intensity variation plot. Along the simulation results provided by the video the normalised azimuthal standard deviation σ_θ was evaluated for the different input fields. The result is presented in figure 5.18.

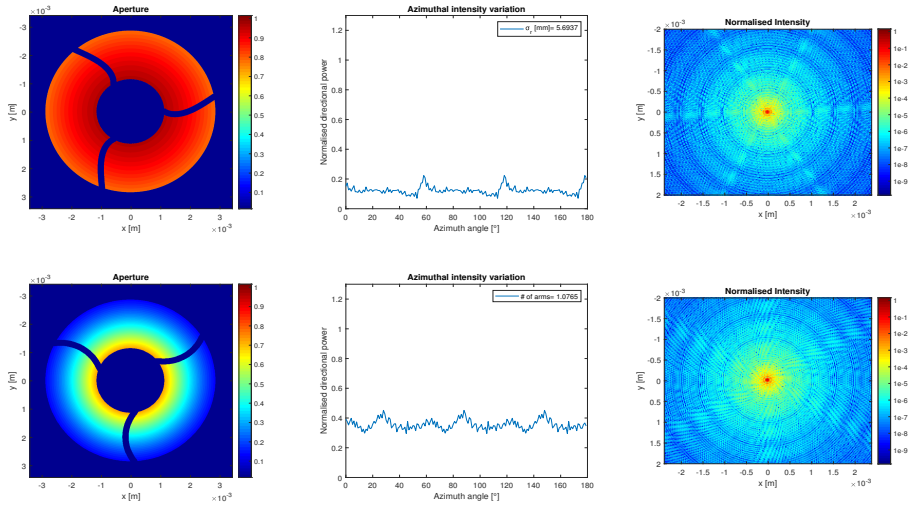

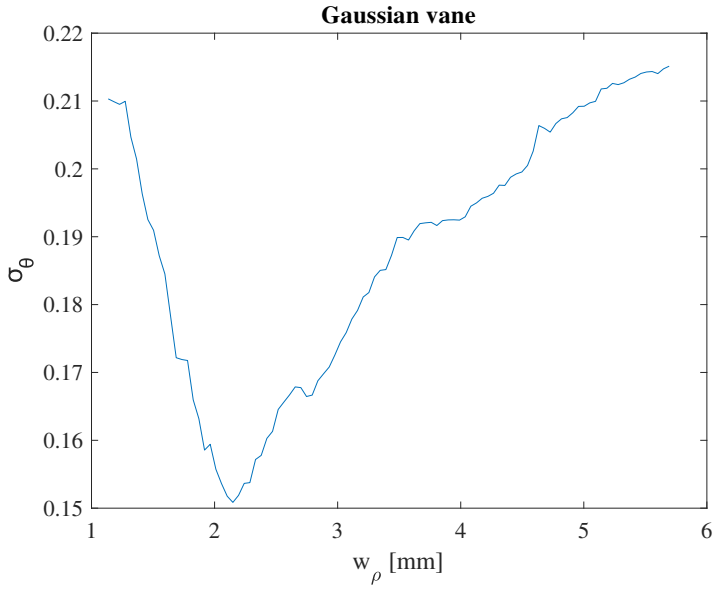

Figure 5.18: σ_θ as function of w_ρ for each input Gaussian distributed intensity.

Both from watching the video and from viewing the figure it is clear that an input beam radius of $w_\rho \approx 2$ mm yields the most isotropic spread which is very close to the radius $w_\rho = 1.99$ mm the aperture was designed for. The possible reasons why the simulated optimum does not exactly coincide with the anticipated value may be due to the simplification made in the method of obtaining the aperture shape, see appendix A.6, that $\theta_{\text{arc}} = 70°$ is not optimal for gaussian vanes or most likely, the small reduction of arc angle due to the width w that is inherent to how the aperture was generated. Nevertheless, the difference is small and it seem safe to say that the condition in (5.14) holds and may be used to generate vanes for the purpose of achieving isotropic PSF for a Gaussian beam of certain w_ρ.

5.3.1 Snake vanes

One idea of aperture shape that might accommodate both constant input fields and more spatially varying fields, such as Gaussian beams, is simulated in the bottom row in the video above. The aperture consists of a number of constant curvature vanes stacked along each arm, each curve of an arc angle of $\theta_{\text{arc}} = 70°$, as was optimal according to the previous sections. Theoretically, for a constant input field, each curve on each of the arms should diffract the intensity isotropically, hence the requirement for constant amplitude input fields should be satisfied. Moreover, since with more curves per arm, the intensity of a spatially dependent field should not change as rapidly per change in arc angle because the curvature is more intense. This would imply that even though the condition in (5.14) is not satisfied, the intensity would be more isotropically diffracted than for a single arm curve of $\theta_{\text{arc}} = 70°$. This, so called snake vane aperture is thus anticipated to account for a wider range of input fields, given that the number of arcs per arm is an integer.

However, as can be seen in the video, and the plot of σ_θ in figure 5.19 the optimum number of arcs lands on 1. The reason why this idea breaks down is the requirement on a constant arm width w which causes arms with many arcs to assume the shape of circle sectors in contrast to thin rods which the principle of curved vanes required, hence we acquire the speckled pattern for the largest number of arms which is far from what we desire. If instead we assume $w\frac{dl}{d\theta} = \text{const}$ such that the arm gets thinner with increasing number of arcs then this aperture type should perform better. In a practical system we do require a minimum w which effectively ruins this approach and although a Schwarzschild system may not benefit from a snake vane aperture they may find use in other applications. A further analysis should be employed if such is considered.

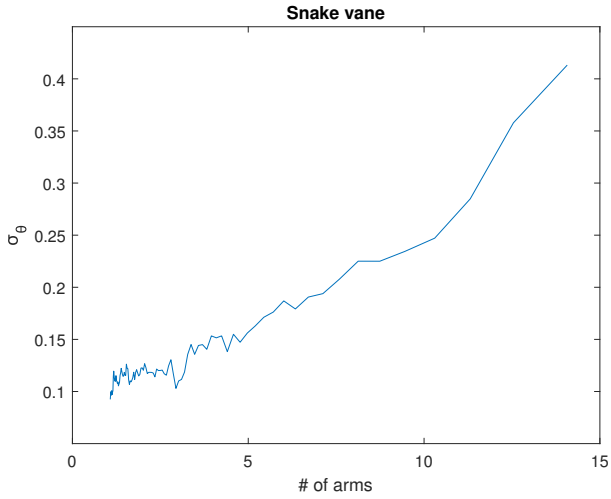

Figure 5.19: σ_θ as function of the number of arcs per arm, given in the video as "# of arms". The input field was in this case a Gaussian beam of radius $w_\rho = 1.99$ mm.

The simulation parameters for the snake vane simulations are the same as for the Gaussian vane, except varying number of arcs, constant curvature and constant

input field.

6

Physical implementation

In chapter 5 the aperture function $p(x, y)$ was optimised in respect to various image quality criteria and for the implementation in the Schwarzschild objective a constant curvature spider vane of arc angle $\theta_{\text{arc}} = 70°$ was considered to yield the best performance. The aperture function p is however just a 2-dimensional surface representing the radial projection from the support structure onto the starting surface, remember section 4.3.3. This chapter deals with the relation between the 3D spider vane structure and the aperture function p as well as the constraints on the geometry with regard to manufacture capabilities and stability requirements.

6.1 From 2D to 3D

The supports for the secondary mirror of the objective lie in a plane perpendicular to the optic axis where they connect to the barrel of the device, see figure 4.6a. This setup minimises the size of the support structure and effectively provides the most stability. The intention is thus to keep the new design under the same requirements, that it should be bound by two parallel planes separated by a thickness t which measures 3 mm for 15X and 1.3 mm for 40X. The exact geometry required for obtaining the desired aperture function p is easily found by projecting the aperture p along the radial lines converging in the focal point, from the spherical surface onto the two parallel planes, see figure 6.1.

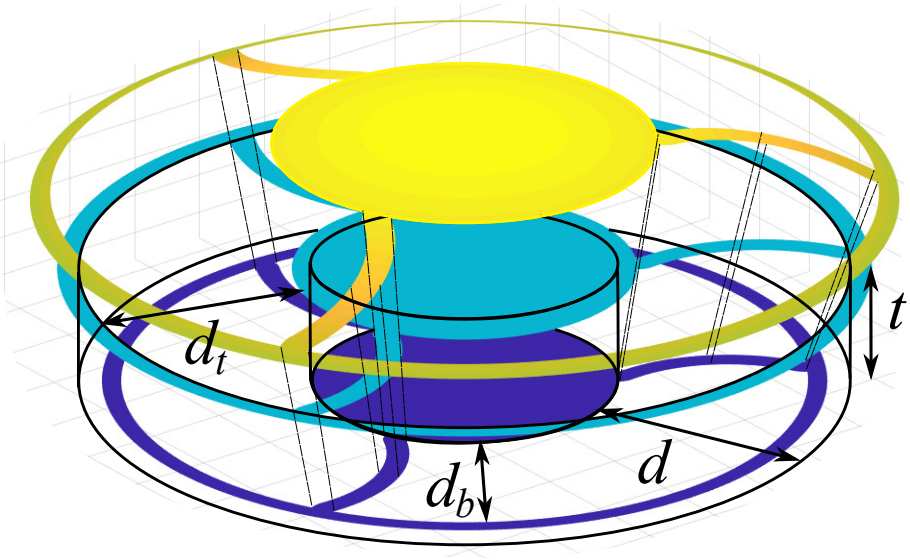

Figure 6.1: An illustration of the radial projection of p from the spherical surface onto the parallel planes bounding the 3D spider vane structure. The spherical aperture is given in yellow, the top plane aperture projection in light blue and the bottom plane aperture projection in blue. The thickness of the structure is t, the difference between physical inner and outer circular structures $d = R_i - r_i$, the difference between top plane aperture projection inner and outer circular obscurations d_t and for the bottom plane d_b. The thin black dashed lines represent radial lines.

The 3-dimensional solid structure that contributes the aperture function p on the spherical surface is thus the aperture projections on the parallel planes attached together by the radial lines as visualised in the figure. One implication this bears is the different sizes of arms on the two planes. Not only will the arm length shrink but so also the width when the projection approaches the focal point. This is seen in figure 6.1 and is further emphasised in figure 6.2 and 6.3.

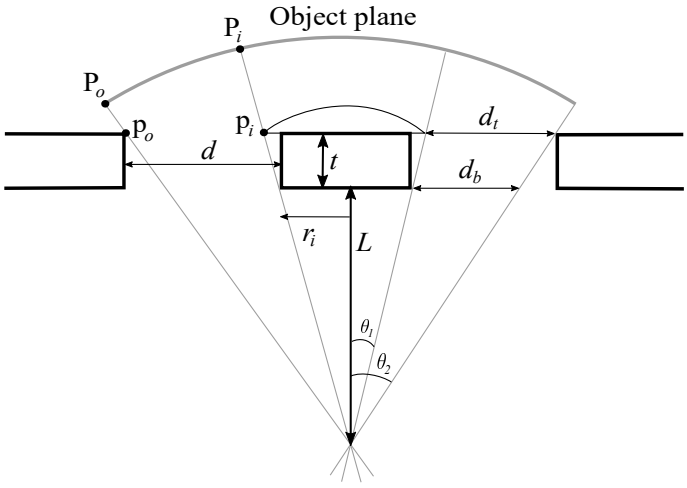

Figure 6.2: A side view of the Schwarzschild aperture. The secondary mirror is mounted on a cylindric island which is connected via arms to the annular barrel.

As is clear from figure 6.2 the arm lengths d_t and d_b for either projection does not span the entire distance between the mirror mount and the barrel. It is over these lengths the arc angle θ_{arc} need to be subtended since the rest of the arm is outside the ray path. The arms still need to connect both sides anyhow and how one wishes to shape the rest of the arm is unimportant to the diffraction problem. As an example one could continue the arcing or use a straight finish. If the structure is small to begin with and the projection lengths become very small it may be challenging to realise the desired structure depending on the method of manufacture. In this project, the prototype spider vane structure design was aimed for fabrication using a cutting wire. The wire, usually with radii in tenth of millimeters, is unable to create sharp edges as it cuts out the material, which implies that close to the connects the curves will be more rounded, effectively reducing the available space for the necessary θ_{arc} arc. This issue is more apparent for smaller objectives and objectives with larger NA, both conditions met by the 40X objective investigated here.

Figure 6.3: The shadow cast by an object increase with decreasing distance between object and point source.

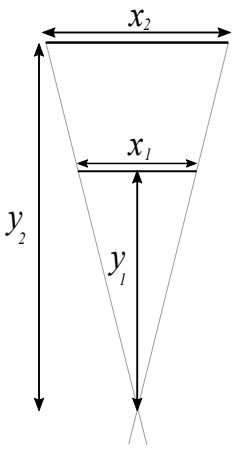

The arm width w is also subject to decrease relative the spherical surface and more importantly, as the distance between different points P on the spherical surface and corresponding projection points p on the planar surfaces is not constant (see figure 6.2), w will be non-constant on the projected apertures. Projection scales with distance, see figure 6.3, thus the projected aperture arm will be widest by the central mirror and smallest at the barrel. As there is a minimum width $w = w_{\text{min}}$ required for the arm to stay sufficiently rigid it must therefore be located by the barrel. Note that a thickness $t > 0$ will cause the bottom projection to have an even smaller width w and the minimum required width therefore refers to one of the two projections. For the spherical aperture to be constant in width the arm width needs to increase toward the central mirror, causing more obscuration than what would be the case if $w = w_{\text{min}}$ along the entire arm. If $w = w_{\text{min}}$ along the whole arm is employed, then the width $w = w(\theta)$ at the spherical surface would read, (6.1):

$$w(\theta) \approx \frac{R}{Z} \cos\theta \tag{6.1}$$

Here, R is the radial distance to the spherical surface, $Z = L + t$ if w is referenced to the top planar projection and θ is the same coordinate providing θ_1 & θ_2 in figure 6.2. For the principle of curved vanes to not break down because of this varying arm width the arm curvature needs to change such that (5.14) is not violated, considering a constant intensity. Effectively, this requires the curvature per length to increase toward the central mirror such that the width variation in (6.1) is compensated everywhere.

If this is accounted for then one would find the optimal geometry for the system of interest, however, the complexity of the mathematics describing this geometry is in itself inconvenient and for the manufacturing cumbersome or even impossible. A simple description of the system is thus appreciated on many levels and if the reduction in quality is negligible it would serve as the best solution.

6.2 Planar approximation

One simplification, which was already mentioned in section 5.2, is to use a constant curvature vane in a planar surface instead of a spherical, that is, to use figure 5.4 instead of figure 5.5. If the numerical aperture is not too large and thickness t not too thick then one can safely apply this planar aperture to one of the planes bounding the structure and the other as the radial projection, without inferring large errors on the spherical surface projection. Note that not only the arm width w will be varying on the sphere but also the curvature of the spherical arm as a consequence of this choice. If the curvature in the planar surface is taken constant then the curvature projected onto the sphere will increase in intensity towards the barrel which will add to the violation of (5.14) as $w(\theta)\frac{dl}{d\theta'} \propto \cos^3\theta$.

Sticking with the constant curvature planar approach, it is of interest to verify if an arc angle of $\theta_{\text{arc}} = 70°$ is still optimal for isotropic spread. A simulation over θ_{arc} for the planar arm aperture was made and the resulting σ_θ is plotted versus θ_{arc} in figure 6.4.

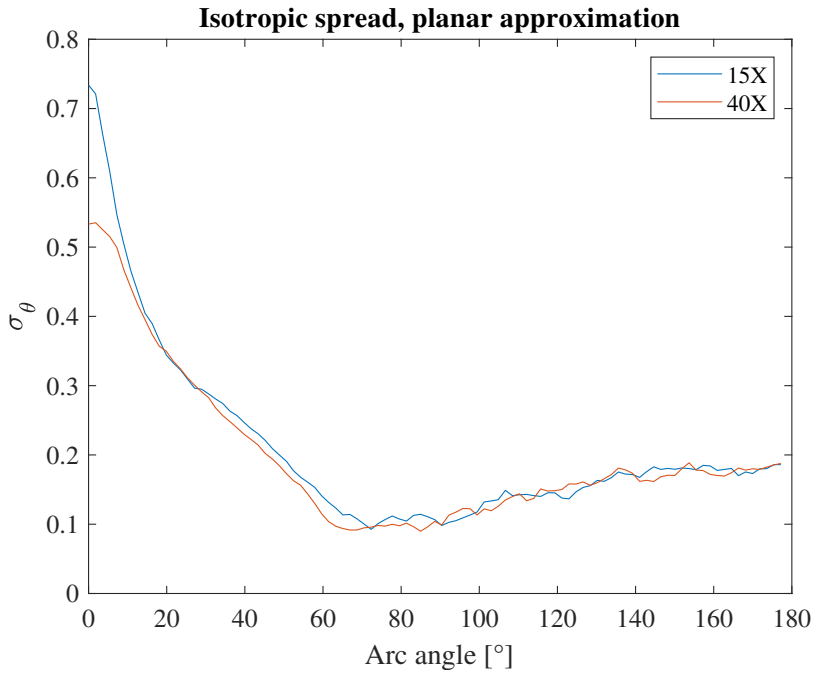

Figure 6.4: The normalised azimuthal standard deviation as function of arc angle for the 15X (blue) and 40X (orange) Schwarzschild objectives. Simulation parameters are found in table B.1 in appendix B.2 except $N = 5000$ (15X only), $\theta_{\text{arc}} = [0, \pi]$, $r_m = 0$, $r_M = D_{\text{image}}/2$, $I_{\text{min}} = 1 \cdot 10^{-6}$.

The result of figure 6.4 shows once again that an arc angle around $\theta_{\text{arc}} = 70°$ produces the most isotropic spread, in this case also when employing the planar constant curvature vane. As this simplified approach also allows us to keep the arm width w constant such that $w = w_{\text{min}}$ over the entire arm we also gain in other quality measures such as obscuration, Strehl ratio and contrast since all of them are directly related to the obscuration area. The value of σ_θ also seems on par with

what was simulated for the spherical case.

For the exact intensity distribution caused by the planar aperture case consider figure 6.5 which shows the simulated PSF for the 40X.

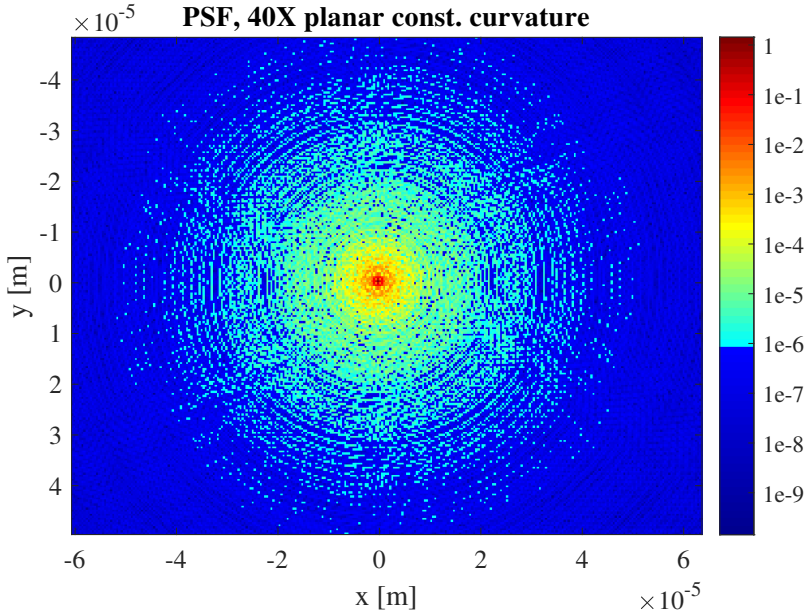

Figure 6.5: The PSF generated for the 40X objective employing the planar approximation. Simulation parameters are found in table B.1 in appendix B.2 except $\theta_{\text{arc}} = 70°$, $r_m = 0$, $r_M = d_{\text{image}}/2$, $I_{\text{min}} = 1 \cdot 10^{-6}$.

The plot conveys a PSF which looks almost perfectly isotropic. The subtle change in azimuth is probably a combination of minor deviation in optimum arc angle and the non ideal aperture shape. The nonideal aperture shape is moreover compared to that of a spherical projection onto the same top planar surface, see figure 6.6. Here one can see the exact difference between the two apertures and from this depiction, concerning the most sensitive case being the 40X objective, it is clear that the shapes are quite similar. The order of difference might even be of the same magnitude as eventual fabrication errors. Thus, considering the two objectives investigated in this work, the planar approximation may very well suffice. For objectives of larger NA, thickness and where even better performance is desired, one should stick with the spherical constant curvature vanes.

As a throwback to the previously mentioned

Figure 6.6: The composite image of a planar approximated aperture arm on the top planar surface (green + black) and the spherical constant curvature aperture arm radially projected onto the top planar surface (red + black), this time with same width w on their corresponding surfaces which meet at the barrel, hence same width there.

implementation of curved vanes in [21] we will discuss how this design compares to the design that has been developed in this work. First, in [21] the 2D aperture employs a constant curvature vane in the planar approximation of arc angle $\theta_{\text{arc}} = 60°$. Based on the investigation in chapter 5 we know that an arc angle of $\theta_{\text{arc}} = 70°$ provide further reduction of intensity spikes. Furthermore, to obtain the 3D structure in [21] the 2D aperture is simply expanded along the optic axis until it measures the desired thickness. It thus exhibit a cylindrical symmetry instead of being radially projected to compensate for the focused ray trajectories inside the microscope objective. The cylindrical symmetry of spider vanes is common in reflective telescopes since there, the obscured ray trajectories are instead parallel which is the main difference compared to a focused system. In the case of reflective microscope objectives, the consequence of not performing the radial projection is a larger obtained obscuration. This in turn results in degraded image quality measures despite that the aperture provides the same support as the width and thickness are the same. Also, the PSF will end up not being fully isotropic due to the effective varying arm width of the aperture shadow.

6.3 Implementation cost

Compared to the original design it is clear that the new proposed geometry contributes in complexity for conventional fabrication techniques. This will most certainly imply an increased production time and cost which will result in larger expenses considering both economically and with respect to environmental sustainability. These effects may already be considered at the optimisation stage for a broader evaluation to be performed. The exact implications on manufacture for the new type of design have not been investigated however and therefore no such analysis has been made. Nevertheless, since the optimisation was quite supportive of the proposed design which furthermore was possible to employ using wire cutting, a conventional fabrication technique, one should feel relatively secure in the implementation, given that the prototype testing verifies the anticipated results.

7

Prototype testing

Now that the spider vane design has undergone a thorough theoretical and numerical investigation it is of major interest to experimentally verify its anticipated qualities. This chapter outlines the experimental testing of a 15X prototype objective employing the planar constant curvature spider vane with an arc angle of $\theta_{\text{arc}} = 60°$, see figure 7.1b. Measurements on the original straight vane design, in figure 7.1a, are also covered for comparison. Again, the equipment used for obtaining the measured data is presented in appendix B.1 along with photos of the setup.

(a) A photo of the straight vane objective.

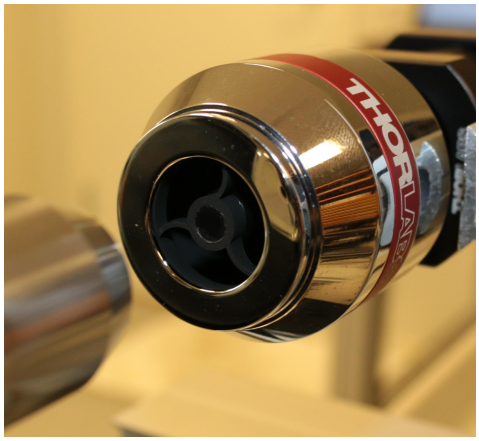

(b) A photo of the curved vane objective.

Figure 7.1

7.1 Measurement

For extracting the various image quality measures of interest and for comparison to the original design the PSF for both 15X objectives, straight vane design and curved vane design, was captured using "setup B" shown in figure 3.1 and by following the methodology described in chapter 3 and section 4.3.3. Note that the choice of $\theta_{\text{arc}} = 60°$ was based on the original curved vane principle predicting an angle of $\pi/3$ radians to give most spread of the intensity spikes and was done prior to the discovery of anticipated optimal arc angle $\theta_{\text{arc}} = 70°$.

The measured PSF for the original straight vane design is given in figure 7.2a next to figure 7.2b which shows the simulated PSF for the same system. In figure 7.2c and 7.2d the measured and simulated PSF for the new curved vane design are plotted

respectively. The PSFs are normalised to their peak intensity. The simulated PSF was multiplied by a magnification factor of $M = 60$ for obtaining the PSF* used for comparison to measurements.

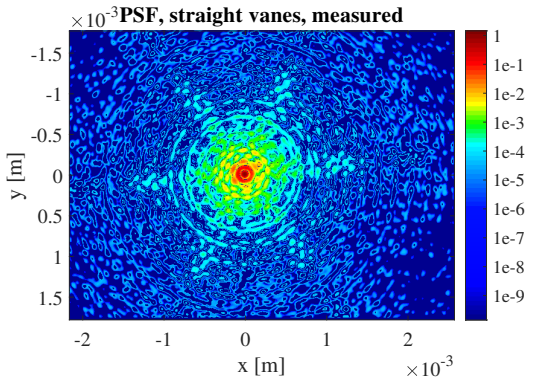

(a) The measured PSF for the straight vane 15X Schwarzschild objective.

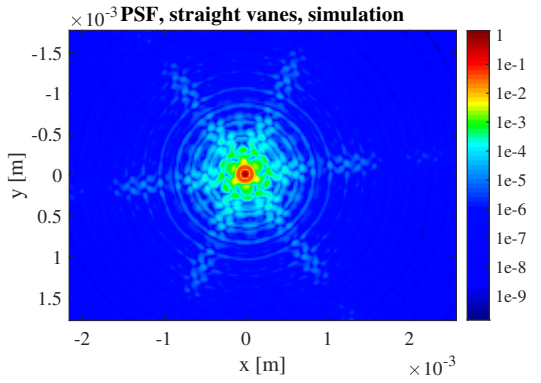

(b) The simulated PSF for the straight vane 15X Schwarzschild objective.

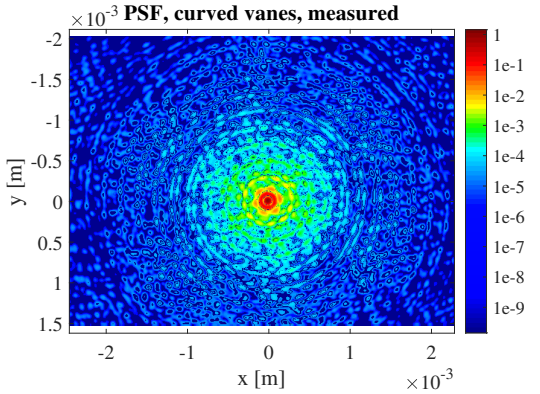

(c) The measured PSF for the curved vane 15X Schwarzschild objective.

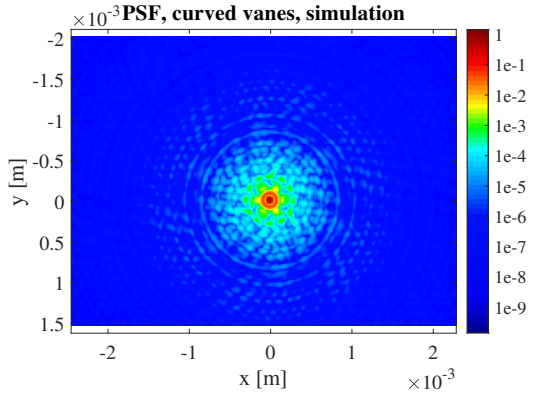

(d) The simulated PSF for the curved vane 15X Schwarzschild objective.

Figure 7.2: Simulation parameters are found in table B.1 in appendix B.2 except $\theta_{\text{arc}} = 0°$ and $w = 0.9\,\text{mm}$ for figures 7.2a and 7.2b, $\theta_{\text{arc}} = 60°$ for figures 7.2c and 7.2d, beam width $w_\rho = 3.7$ mm and $a = 4.7138\,\mu\text{m}$.

To further visualise the azimuhal PSF variation the azimuthal intensity distribution is plotted in figure 7.3 for the measured and simulated straight vane PSF and in 7.4 for the measured and simulated curved vane PSF. The directional power is given by (5.2) using $I_{\text{min}} = 1 \cdot 10^{-6}$, $r_m = 0$ and r_M =the distance to the closest window edge for each measurement.

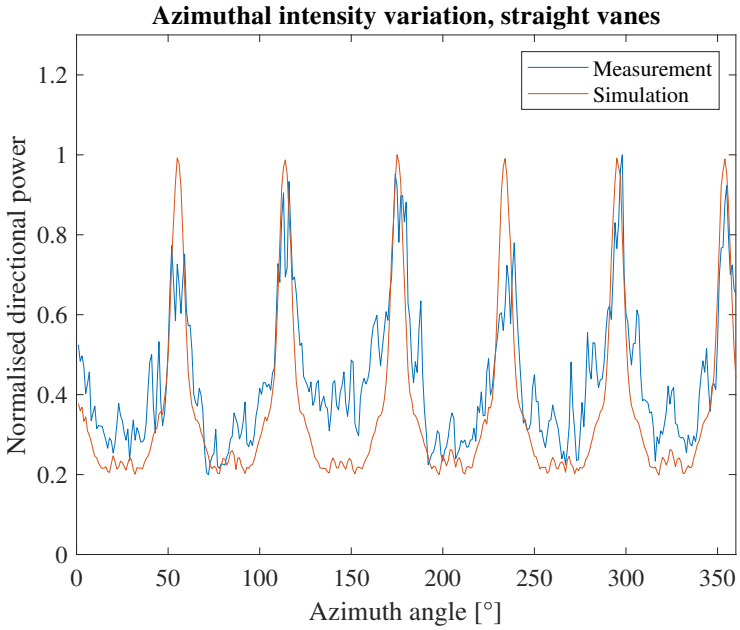

Figure 7.3: The azimuthal intensity variation of the measured straight vane PSF (blue) and the simulated straight vane PSF (orange). The directional powers have been normalised to the maximum value on the graph for each plot respectively. Simulation has been offset somewhat in azimuth angle to better coincide with the measured data.

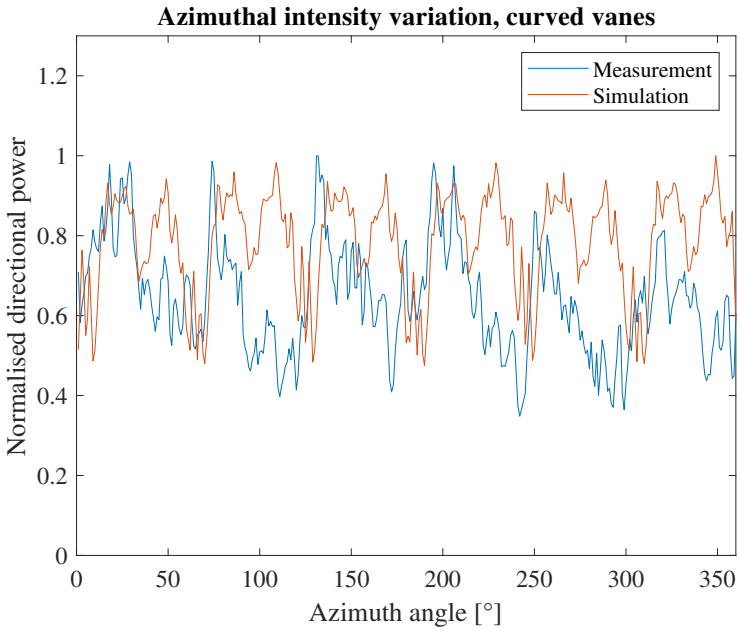

Figure 7.4: The azimuthal intensity variation of the measured curved vane PSF (blue) and the simulated curved vane PSF (orange). The directional powers have been normalised to the maximum value on the graph for each plot respectively. Simulation has been offset somewhat in azimuth angle to better coincide with the measured data.

By comparing the measured PSFs, figure 7.2a vs 7.2c and 7.3 vs 7.4, it is clear that the effect of the curved vane helps reduce the peak intensities present for the original design. Azimuthal variation is still observed for the curved vane PSF but its presence is anticipated since the arc angle employed is $\theta_{\text{arc}} = 60°$ and not 70° which was shown to yield isotropic spread (compare with the first video presented in section 5.2). Furthermore, the input field used in the experiment is not constant but a Gaussian beam which will contribute slightly to azimuthal anisotropy. The fact that it should produce a non-isotropic diffraction pattern is also supported by the simulated PSF in figure 7.2d.

Comparing each measured PSF to its associate simulated PSF show that the off-center intensity relative to the peak intensity is larger for each of the measured PSFs than what is numerically predicted. Note that no intensity scaling has been applied to these simulated PSFs, contrary to what was done in the comparison between experiment and simulation presented in section 4.3.3 for figures 4.7 and 4.8. One reasoning behind this scaling presented then is the same as why we obtain similar results now: the difficulty of manually aligning the secondary imaging system to the focal point along the optic axis. Using a live PSF cross-section plot in the camera software the distance to the secondary imaging system could be altered until peak intensity was achieved, though, due to vibrations large intensity fluctuations disturbed the alignment process. The power delivered by the laser source was also varying with time which added to the challenge. If the PSF is captured off-focus the peak power will decrease while the total throughput will remain the same, thus the surrounding intensity appear larger due to the choice of peak normalisation. This uncertainty in focusing will further infer large uncertainty in the measured quality values evaluated from the peak intensity.

Another unanticipated observation is the long scale azimuthal intensity variation present in the measured PSFs shown in figures 7.3 and 7.4. From previous observations it is established that an aperture of $2\pi/3$-rotational symmetry produces a PSF of $\pi/3$-rotational symmetry and therefore we expect the diffraction pattern to be periodic with angle of periodicity $\theta = 60°$. Though there is some $\pi/3$-periodicity present, it is far from perfect, which most likely is a cause of angular misalignment between the Schwarzschild objective and the secondary imaging system. This effect poses as a problem for the evaluation of the spike magnitude and azimuthal standard deviation, therefore, to compensate for the large angle intensity inhomogeneity these values were evaluated for each 60°-sector separately before being averaged into the final measured σ_θ and S_M. This method is presumed to give a better measure of these values despite the uneven intensity since we from theory know each 60°-sector should look the same. These measures along with the other measured quality values are presented in table 7.1 for the straight and curved vane objectives. The Strehl ratio was calculated as $Q_s = \frac{T_c}{T_s}\frac{P_s}{P_c}$, the subscript "s" indicate straight vane case and "c" curved vane case, the power transmittance is T and the total captured power by the CCD camera P. The transmittance was measured using an optical power meter by taking the ratio of the power transmitted through the objective to the power incident. The total power P was the sum of the normalised intensity captured by the camera. The measured obscuration is here estimated as $Q'_o = \frac{T_c}{T_s}$.

One important note when comparing between the two objectives is the fact that

the curved vane system used a thinner arm width of $w = 0.7$ mm compared to the straight vane case using $w = 0.9$ mm. This has effect on most Q-values in that the obscuration area is in fact smaller for the curved vanes, opposite of what we would have if the arm width is the same for both systems.

Table 7.1: Measured quantities (M) and simulated (S) for the prototype testing performed. Quality values (Q) are always normalised to the respective straight vane case M or S. The value Q'_o is similar to Q_o but with $|1 - p|$ replaced by p in the integrands of (5.7).

	Straight vanes, M	Curved vanes, M	Straight vanes, S	Curved vanes, S
σ_θ	0.3786	0.1951	0.5906	0.1597
S_M	1.0412	0.4589	1.7346	0.2757
Q_s	1	1.0352	1	1.0507
Q_c	1	1.0614	1	1.0323
Q_{ρ_s}	1	1.0008	1	0.998
Q'_o	1	1.0152	1	1.0075

The table confirms the already observed improvement in σ_θ and S_M from straight to curved vanes. There is however a noticeable deviation between measurements and simulations. Possible reasons include the already mentioned sources of error in the measurement setup but also, the choice of low $I_{\min} = 1 \cdot 10^{-6}$. Despite extending the intensity range by stacking images the noise floor was not suppressed below this minimum intensity and further filtered away from the measurements, meaning that a smaller part of the PSF was considered compared to simulations. Also, if unlucky, stray light being reflected against poorly colour coated elements inside the objective may have ended up in the PSF, causing issues that are not taken into account in simulations. The same goes for possible phase variations across the input beam and other potential diffractive effects inside the objective.

The rest of the measured quantities do compare reasonably well to the simulated values, though, since they depend on the captured peak intensity, due to the normalisation, they are accompanied by a large uncertainty. We can thus not conclude more than that they hint toward the simulation being correct in terms of the small change in these quality values with respect to the investigated change in spider vane design.

Due to the sensitive alignment of the experiment sufficient precision and accuracy was not achieved for, with high certainty, verify the anticipated behaviour of the quality values Q_s, Q_c, Q_{ρ_s} and Q'_o. However, the results clearly shows an improvement in σ_θ and S_M indicating a more isotropic intensity distribution. The measurement uncertainties could have been minimised by performing further measurements to assure that the peak intensity is captured, for both objectives. With the current setup this would have taken long time and a possible improvement for alleviating this issue would be to incorporate a live peak intensity tracker and possibly an automatic focusing system. For a better comparison between measurement and simulation in terms of σ_θ and S_M the setup could have been further refined to eliminate stray light through the objective and the characteristic of the input beam could have been measured for a more robust simulation to be performed.

8

Conclusion

In this work, the diffractive effects of the secondary mirror support structure in reflective microscope objectives have been theoretically, numerically and experimentally investigated. A sufficiently precise simulation method was developed for use in large numerical aperture systems, i.e for focusing systems with strongly non-parallel light propagation, and proved applicable for diffraction modelling of the investigated 15X and 40X Schwarzschild objectives. Based on theory and practical considerations regarding feasible manufacturing methods it was concluded that the use of curved spider vanes is the most suitable approach for mitigating the undesired intensity spikes caused by straight support structures. In terms of both structure stability and how well a circularly symmetric PSF is obtained the spider vane design of three arms, each employing a constant curvature of total subtended angle $\theta_{\text{arc}} = 70 - 90°$ was found to outperform other investigated designs. Additionally, with respect to various potential user preferences a numerical optimisation against other image quality criteria of interest was carried out and resulted in an optimal constant curvature spider vane design employing $\theta_{\text{arc}} \approx 70°$. Effects on environmental sustainability were not sufficiently analysed but are anticipated to be negligible.

A more general principle of curved vanes, which also accounts for spatially varying field amplitudes was developed. Based on the analysis on constant curvature vanes the developed principle was verified by simulation to produce close to optimal results in the case of diffraction of Gaussian amplitude distributed optical fields. This by using a curved structure designed to compensate a specific input field.

The practical implementations of the optimal aperture function were investigated for objectives with curved spider vanes and the 3D support structure is simply generated by taking the light ray-projection of the desired aperture. This was shown to make the fabrication of large NA objectives challenging.

In aim of experimentally verifying the proposed qualities of the curved vane design and for comparison to the original design an experimental setup for measuring the PSF was constructed. The 15X Schwarzschild objective using a curved vane support structure with $\theta_{\text{arc}} = 60°$ was experimentally verified to provide considerable improvement in circular symmetry of the PSF compared to the objective with straight support structure. Other measured image quality values indicated that the new design maintains the desired properties of the original design but the measurements are accompanied by considerable uncertainty. Additional measurements and possible improvements in the experiment setup are needed to provide definite verification of overall improved performance regarding the new design.

Although not considered in this study, future work may investigate more thoroughly what effect curved vanes have on non-central imaging. Tilting the aperture

slightly would remove the constant curvature seen by the transmitted light and cause anisotropies in the PSF. However, the image size is quite small and such effects are anticipated to be small. A PSF sweep through the field of focus might also be of interest to observe the effect curved vanes have on unfocused images. Investigating stray light propagating through the objective can also be of interest to explain difference between measurement and simulation.

Bibliography

[1] J. E. Harvey and C. Ftaclas, "Diffraction effects of telescope secondary mirror spiders on various image-quality criteria," *Appl. Opt.*, vol. 34, no. 28, pp. 6337–6349, Oct 1995. [Online]. Available: http://ao.osa.org/abstract.cfm?URI=ao-34-28-6337

[2] J. L. Richter, "Spider diffraction: a comparison of curved and straight legs," *Appl. Opt.*, vol. 23, no. 12, pp. 1907–1913, Jun 1984. [Online]. Available: http://ao.osa.org/abstract.cfm?URI=ao-23-12-1907

[3] BBC news. (1999) World's oldest telescope? . [Online]. Available: http://news.bbc.co.uk/2/hi/science/nature/380186.stm

[4] P. Wartenberg, M. Buljan, B. Richter, G. Haas, S. Brenner, M. Thieme, U. Vogel, and P. Benitez, "40-5: Invited paper: High frame-rate 1" wuxga oled microdisplay and advanced free-form optics for ultra-compact vr headsets," *SID Symposium Digest of Technical Papers*, vol. 49, no. 1, pp. 514–517, 2018. [Online]. Available: https://onlinelibrary.wiley.com/doi/abs/10.1002/sdtp.12447

[5] S. Lan, X. Zhang, M. Taghinejad, S. P. Rodrigues, K. Lee, Z. Liu, and W. Cai, "Metasurfaces for near-eye augmented reality," *CoRR*, vol. abs/1901.06408, 2019. [Online]. Available: http://arxiv.org/abs/1901.06408

[6] M. Faraji-Dana, E. Arbabi, A. Arbabi, S. M. Kamali, H. Kwon, and A. Faraon, "Compact Folded Metasurface Spectrometer," *Nature Commun.*, vol. 9, no. 1, p. 4196, 2018.

[7] W. Wall, *A History of Optical Telescopes in Astronomy.* Springer, 2018, ch. 5, p. 67. [Online]. Available: https://www.springer.com/la/book/9783319990873

[8] HUBBLSITE. (2019) Hubble essentials. [Online]. Available: http://hubblesite.org/the_telescope/hubble_essentials/

[9] Edmund Optics. (2019) Introduction to Reflective Objectives. [Online]. Available: https://www.edmundoptics.com/resources/application-notes/microscopy/introduction-to-reflective-objectives/

[10] R. L. Clark, *Amateur Telescope Making in the Internet Age: Finding Parts, Getting Help, and More (The Patrick Moore Practical Astronomy Series).* Springer, 2010. [Online]. Available: https://www.amazon.com/Amateur-Telescope-Making-Internet-Age-ebook/dp/B008HR71KK?SubscriptionId=AKIAIOBINVZYXZQZ2U3A&tag=chimbori05-20&linkCode=xm2&camp=2025&creative=165953&creativeASIN=B008HR71KK

[11] Thorlabs. (2019) Reflective Microscope Objectives . [Online]. Available: https://www.thorlabs.com/newgrouppage9.cfm?objectgroup_id=6933

[12] M. J. RIEDL, *Optical Design Fundamentals for Infrared Systems, Second Edition.* SPIE PRESS, 2001, p. 202. [Online]. Available: https://spie.org/Publications/Book/412729

[13] M. C. T. Bahaa E. A. Saleh, *Fundamentals of Photonics.* Hoboken, New Jersey: John Wiley & Sons, inc.., 2007.

[14] G. D. Boreman, *Modulation Transfer Function in Optical and ElectroOptical Systems (SPIE Tutorial Texts in Optical Engineering Vol. TT52).* SPIE Publications, 2001. [Online]. Available: https://www.amazon.com/Modulation-Transfer-Function-ElectroOptical-Engineering/dp/0819441430?SubscriptionId=AKIAIOBINVZYXZQZ2U3A&tag=chimbori05-20&linkCode=xm2&camp=2025&creative=165953&creativeASIN=0819441430

[15] Edmund Optics. (2019) Introduction to Modulation Transfer Function. [Online]. Available: https://www.edmundoptics.com/resources/application-notes/optics/introduction-to-modulation-transfer-function/

[16] M. Gu, *Advanced Optical Imaging Theory.* Hoboken, New Jersey: Springer-Verlag Berlin Heidelberg, 2000.

[17] F. Maass and P. Martin, "Precise analytic approximations for the bessel function j1(x)," *Results in Physics*, vol. 8, pp. 1234 – 1238, 2018. [Online]. Available: http://www.sciencedirect.com/science/article/pii/S2211379718300111

[18] J. D. Schmidt, *Numerical simulation of optical wave propagation with examples in MATLAB. [electronic resource].* Bellingham, Wash. : SPIE, c2010., 2010. [Online]. Available: http://proxy.lib.chalmers.se/login?url=http://search.ebscohost.com/login.aspx?direct=true&db=cat06296a&AN=clc.b1976208&lang=sv&site=eds-live&scope=site

[19] C. Rydberg and J. Bengtsson, "Efficient numerical representation of the optical field for the propagation of partially coherent radiation with a specified spatial and temporal coherence function," *Journal of the Optical Society of America. A, Optics, image science, and vision*, vol. 23, pp. 1616–25, 08 2006.

[20] Y. Nakata, Y. Urade, T. Nakanishi, and M. Kitano, "Plane-wave scattering by self-complementary metasurfaces in terms of electromagnetic duality and babinet's principle," 2013.

[21] Edmund Optics. (2019) Reflective Objectives. [Online]. Available: https://www.edmundoptics.com/c/reflective-objectives/709/

A

Appendix 1

A.1 Details on the numerical propagation method

This section provides additional material on the numerical method employed in the project work. The derivation of the propagation method is presented in section A.1.1, the constraints on sampling are described in section A.1.2, the treatment of numerical window size is outlined in section A.1.3

A.1.1 Derivation of the output field for the spherical to planar Huygen-Fresnel principle

The geometry that is used and the respective coordinates are shown in figure 4.1. We start from the Huygen-Fresnel integral, presented in section 2.3.1, which is repeated here for convenience (A.1):

$$g(\mathbf{p}_i) = \frac{-i}{2\lambda} \int_S f(\mathbf{p}_o) \frac{e^{ikr'}}{r'} (1 + \cos\chi) dS \tag{A.1}$$

Here, g is the field in $\mathbf{p}_i$ and f is the field in $\mathbf{p}_o$. S is the surface of integration (object plane) defined as $r =$ constant, $\theta \leq \theta_{\max}$ in spherical coordinates centered in focus and $dS = r^2 \sin\theta d\theta d\phi$ is the corresponding differential area element. In (A.1) it is assumed the phase front of f coincides with S (see χ in figure 4.1). We will use the coordinates u, v to describe points $\mathbf{p}_i$ in the image plane and coordinates x, y, z to describe points $\mathbf{p}_o$ in the object plane:

$$\mathbf{p}_o = \begin{cases} z = r\cos\theta \\ y = r\sin\theta\sin\phi \\ x = r\sin\theta\cos\phi \end{cases} \quad , \quad \mathbf{p}_i = \begin{cases} u(=x) \\ v(=y) \\ \rho = \sqrt{(u^2+v^2)} \end{cases} \tag{A.2}$$

Using the law of cosines we have:

$$\rho^2 = R^2 + r'^2 - 2Rr'\cos\chi \tag{A.3}$$

$$\Rightarrow \cos\chi = \frac{R^2 + r'^2 - \rho^2}{2Rr'} \tag{A.4}$$

The distance between $\mathbf{p}_o$ and $\mathbf{p}_i$ can be written as in (A.5):

$$r' = \sqrt{(r\sin\theta\cos\phi - u)^2 + (r\sin\theta\sin\phi - v)^2 + r^2\cos^2\theta} \tag{A.5}$$

which, using $r = R, \quad \forall \mathbf{p}_0 \in S$, can be rewritten into (A.6)

$$r' = \sqrt{R^2 + \rho^2 - 2R(u\sin\theta\cos\phi + v\sin\theta\sin\phi)} \\ = R\sqrt{1 + \frac{\rho^2}{R^2} - \frac{2}{R}(u\sin\theta\cos\phi + v\sin\theta\sin\phi)} \quad \text{(A.6)}$$

We expand (A.6) in a taylor series and take the first two terms $\sqrt{1+x} = 1 + x/2 - x^2/8 + ..$, arriving at (A.7).

$$r' = R + \frac{\rho^2}{2R} - (u\sin\theta\cos\phi + v\sin\theta\sin\phi) \quad \text{(A.7)}$$

As $\rho_{\max} << R$ is likely in our geometry we can approximate $r' \approx R$ except for in the phase factor $e^{ikr'}$ which we can now rewrite as in (A.8)

$$e^{ikr'} = e^{ikR}e^{ik\frac{\rho^2}{2R}}e^{-i2\pi(u\nu_x + v\nu_y)} \quad \text{(A.8)}$$

Only the last factor in (A.8) is integrated, which we recognise as a fourier transform in the coordinates $\nu_x = \frac{\sin\theta\cos\phi}{\lambda} = \frac{x}{R\lambda}$ and $\nu_y = \frac{\sin\theta\sin\phi}{\lambda} = \frac{y}{R\lambda}$. To obtain the fourier transform we need to rewrite the area element dS in terms of the differential elements $d\nu_z$ and $d\nu_x$. Rewriting dS in cartesian coordinates $d\nu_x$ and $d\nu_y$ is also convenient considering the accommodation of matrix sampling used in the numerical software. Assuming sufficient sampling we note from figure A.1 the following relationship:

$$dS\cos\theta = dS', \quad \text{where:} \quad \begin{cases} dS' = dxdy \\ \cos\theta = \frac{z}{R} \end{cases} \quad \text{(A.9)}$$

and using the following relations:

$$\begin{cases} x = R\lambda\nu_x \\ dx = R\lambda d\nu_x \\ y = R\lambda\nu_y \\ dy = R\lambda d\nu_y \end{cases} \quad \text{(A.10)}$$

we arrive at the expression for dS (A.11):

$$dS = \frac{d\nu_x d\nu_y R^2\lambda}{\sqrt{\frac{1}{\lambda^2} - \nu_x^2 - \nu_y^2}} \quad \text{(A.11)}$$

Figure A.1: The square sampling grid projected along $\hat{z}$ onto the spherical starting surface S. Since the samples on the surface S are not equidistant from each other it is required to consider the relation between dS and dS'.

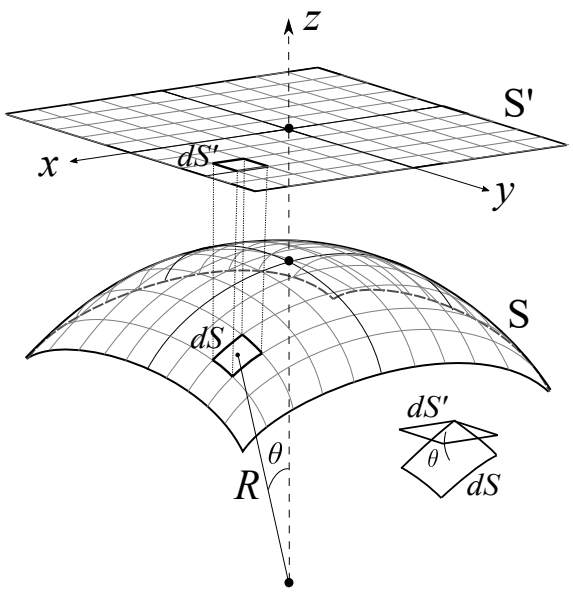

From (A.11) and figure A.1 we note that a compensation in magnitude is applied as a consequence of the spherical to planar mapping.

The integral in (A.1) can now be written as in (A.12):

$$g(u,v) = \frac{-iR^2}{2} e^{ikR} e^{ik\frac{u^2+v^2}{2R}} \int_S \frac{f(\nu_x,\nu_y)}{\sqrt{\frac{1}{\lambda^2}-\nu_x^2-\nu_y^2}} \frac{(1+\cos\chi)}{r'} e^{-i2\pi(u\nu_x+v\nu_y)} d\nu_x d\nu_y \tag{A.12}$$

Using the approximations: $r' \approx R$ and $\cos\chi \approx 1$ which require $\rho_{\max} << R$ the integral is further simplified to (4.1):

$$g(u,v) = -iRe^{ikR} e^{ik\frac{u^2+v^2}{2R}} \mathscr{F}\left\{ \frac{f(\nu_x,\nu_y)}{\sqrt{\frac{1}{\lambda^2}-\nu_x^2-\nu_y^2}} \right\}(u,v) \tag{A.13}$$

The integral in (A.12) adopts the shape of the fourier transform if the field f is zero outside the surface of integration S.

The backward relation is given by (A.14):

$$f(\nu_x,\nu_y) = \frac{ie^{-ikR}\sqrt{\frac{1}{\lambda^2}-\nu_x^2-\nu_y^2}}{R} \mathscr{F}^{-1}\left\{ g(u,v) e^{-ik\frac{u^2+v^2}{2R}} \right\}(\nu_x,\nu_y) \tag{A.14}$$

A.1.1.1 Test of validity

In order to neglect higher order terms in the expansion of (A.5) we require that they are sufficiently small. We will here investigate whether the third term in the expansion can be neglected considering the geometry and wavelength of interest. The third term in the expansion of r' is given in (A.15)

$$r'_3 = \frac{-R}{8}\left[\frac{\rho^4}{R^4} + \frac{4}{R^2}(u\sin\theta\cos\phi + v\sin\theta\sin\phi)^2 - \frac{4\rho^2}{R^3}(u\sin\theta\cos\phi + v\sin\theta\sin\phi) \right] \tag{A.15}$$

Assuming worst case scenario, taking $v = 0$, $\rho = \rho_{\max}$ and $\theta = \theta_{\max}$ and the following parameter values to form an example: $\lambda = 543\,\text{nm}$, $R = 25\,\text{mm}$, $\rho_{\max} = 100\,\mu\text{m}$ and $\sin\theta_{\max} = 1/2$. The phase contribution from the three terms is thus:

$$\frac{kr'_3}{\pi} = \begin{cases} \frac{\rho_{\max}^4}{4\lambda R^3} = 2.95\cdot 10^{-6} & << \quad 1 \\ \frac{\rho_{\max}^2 \sin^2\theta_{\max}}{\lambda R} = 0.1842 & < \quad 1 \\ \frac{\rho_{\max}^3 \sin\theta_{\max}}{\lambda R^2} = 1.4733\cdot 10^{-3} & << \quad 1 \end{cases} \tag{A.16}$$

Ideally each of the terms in (A.16) should be much smaller than one. The above example might lie in the limit of what one can allow. We now proceed with comparing to the fresnel approximation in the planar geometry, the third term in the expansion is:

$$r'^p_3 = \frac{-1}{8L^3}\left[(x-u)^4 + (y-v)^4 - 2(x-u)^2(y-v)^2 \right] \tag{A.17}$$

For worst case we can assume $y = v = 0$ and using $R = L$, $(x-u)_{\max} = R\sin\theta_{\max}\cos\phi - \rho_{\max}$ we get $kr_3'^p/\pi = (L\sin\theta_{\max}\cos\phi - \rho_{\max})^4/4\lambda L^3 \approx 670 >> 1$.

For the same geometry and wavelength in this example it appears that the spherical to planar propagation method seem relatively safe to use in contrary to the ordinary Fresnel approximation.

A.1.2 Sampling requirement on the numerical method

Enough samples are required as to sufficiently replicate the contribution from all spherical waves emitted by the object plane. Thus we sample such that the phase difference between two waves from any neighbouring points on the object plane is less than $\alpha\pi$ when they interfere in any point in the image plane. Consider figure A.2.

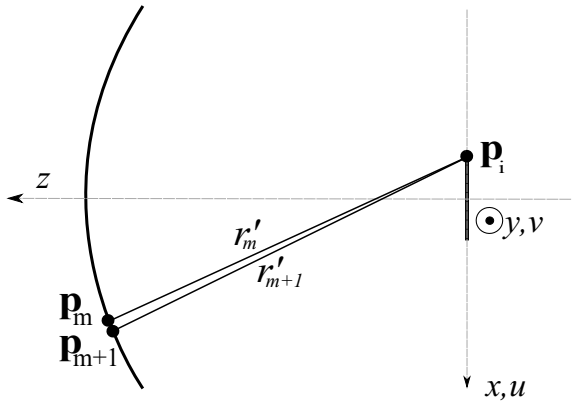

Figure A.2: Two neighbouring sample points. Their waves interfere in a point $\mathbf{p}_i$.

We require that $k|r'_{m+1} - r'_m| < \alpha\pi$. This is true for a phase front coinciding with the object plane, any other phase front will require another analysis, and most likely more samples. Seeing as the object plane is focused in the center of the image plane the largest phase difference between neighbouring points will be obtained for $\rho = \rho_{\max}$. Using this we can express the worst case phase difference as in (A.18) (taking $y = v = 0$):

$$\Delta\Phi = k\left|\sqrt{R^2 + \rho_{\max}^2 - 2x_{m+1}\rho_{\max}} - \sqrt{R^2 + \rho_{\max}^2 - 2x_m\rho_{\max}}\right| \tag{A.18}$$

Let δ be the sampling distance, then $x_n = n\delta$ where $n \in Z$. We find the worst case when $\partial\Delta\Phi/\partial n = 0$. Carrying out the calculation show that there is no local maximum or minimum, that is, $\partial\Delta\Phi/\partial n \neq 0, \forall n$. Instead we have to examine the edge cases:

$$\alpha\pi > \Delta\Phi = k\left|\sqrt{R^2 + \rho_{\max}^2 - 2(M-1)\delta\rho_{\max}} - \sqrt{R^2 + \rho_{\max}^2 - 2M\delta\rho_{\max}}\right| \tag{A.19}$$

We can substitute M using the maximum aperture diameter in the object plane D, $M = \frac{D}{2\delta}$. We get

$$\alpha\pi > k\left|\sqrt{R^2+\rho_{\max}^2-2(D/2-\delta)\rho_{\max}}-\sqrt{R^2+\rho_{\max}^2-D\rho_{\max}}\right| \tag{A.20}$$

Solving for δ gives (A.21)

$$\delta \leq \left|\frac{1}{2\rho_{\max}}\left[D\rho_{\max}+\left(\alpha\lambda/2+\sqrt{R^2+\rho_{\max}^2-D\rho_{\max}}\right)^2-R^2-\rho_{\max}^2\right]\right| \tag{A.21}$$

Note that in (A.21) $\rho_{\max}$ can be negative which is the case shown in figure A.2. As an example, for a system of the following parameter values: $\alpha = 0.1$, $D = 20\,\text{mm}$, $\lambda = 543\,\text{nm}$, $R = 25\,\text{mm}$, $\rho_{\max} = 100\,\mu\text{m}$ and $\sin\theta_{\max} = 1/2$ we have $\delta = 6.78\,\mu\text{m}$ for $0 < \rho_{\max}$ and $\delta = 6.80\,\mu\text{m}$ for $\rho_{\max} < 0$. The farthest distance between two neighbouring samples must not exceed $\delta \leq 6.78\,\mu\text{m}$. For a square grid of samples this distance corresponds to the diagonal between neighbouring elements. The distance a between each sample along the columns and rows of the array must thus satisfy (A.22):

$$a \leq \frac{\delta}{\sqrt{2}} \tag{A.22}$$

We now compare with the required sampling distance for a planar wave in a planar objection plane. The worst case is obtained for propagation between points on opposite sides of the planes. The phase difference is (here $0 < \rho_{\max}$):

$$\Delta\Phi = k\left|\sqrt{L^2+(\rho_{\max}+(D/2-\delta))^2}-\sqrt{L^2+(\rho_{\max}+D/2)^2}\right| \tag{A.23}$$

Solving for δ gives

$$\delta \leq \frac{D}{2}-\left[\sqrt{(\sqrt{L^2+(\rho_{\max}+D/2)^2}-\alpha\lambda/2)^2-L^2}-\rho_{\max}\right] \tag{A.24}$$

which, using the same parameter values as above, give $\delta = 72.5\,\text{nm}$. This is the situation you end up in when attempting the angular spectrum propagation method for the given system parameters. The array size required to cover the aperture $D = 2$ cm is $(\frac{\sqrt{2}D}{\delta})^2 = (\approx 390\cdot 10^3)^2$ vs $(\approx 4200)^2$ for the spherical starting surface.

A.1.3 Numerical window size requirements

For evaluation of the fourier transform given in (4.1) N is taken as an even number and the coordinate $x = 0, y = 0$ is sampled in position (r,c)=(N/2+1,N/2+1) in the array.

To avoid aliasing due to larger spatial frequencies folding in at the edges of our numerical window we need to analyse again the geometry. The samples constitute a square grid with uniformly separated points in ν_x-ν_y-space which is a cartesian-like system. This implicates that the samples are nonuniformly spaced on the spherical object surface. The spacing will be closest on the spherical surface where it is tangent to the u-v plane. The derived maximum sampling distance in the previous section corresponds to the diagonal distance between sample points in a square grid. Thus

the shortest distance between samples in the square grid is $a = \delta/\sqrt{2}$. The Nyquist criterion then gives the largest sampled spatial frequency as $\nu_{max} = 1/2a$.

In general, the largest sampled spatial frequency in each point is approximately given by $\nu_{max}(\theta) = 1/2Rd\theta$ if the number of samples is large and the distance R is large (see figure 4.1). Note however that θ used in this derivation refers to figure A.3 and is not the same. Using the relations in (A.2) the expression can be rewritten as $\nu_{max}(\theta) = \sin\theta/2a$. The angle at which the maximum spatial frequency propagates relative to the normal of the spherical surface the grid points interpolate, in each point, is:

$$\theta'_{max} = \arcsin(\lambda\nu_{max}(\theta)) \tag{A.25}$$

We now aim to find the maximum distance l from the center of the image plane to which a sampled spatial frequency can propagate. Consider figure A.3.

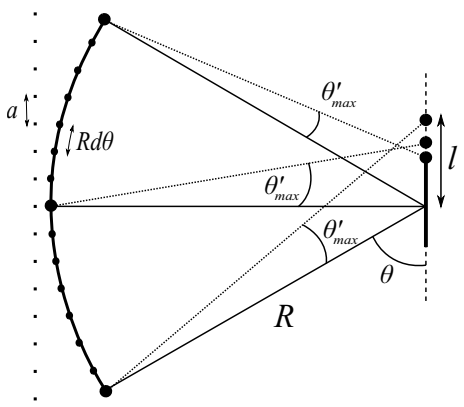

Figure A.3: Representation of the window size problem.

It is sufficient to analyse the problem considering θ'_{max} to one side only if solving for all θ for $\pi - \Phi \leq \theta \leq \pi + \Phi$ where $\Phi = \arcsin(D_{aperture}/2R)$. We can express the maximum length as in (A.26):

$$l(\theta) = |R\sin\theta\tan(\theta'_{max} + \frac{\pi}{2} - \theta) - R\cos\theta| \tag{A.26}$$

Evaluating (A.26) numerically for $R = 25.6\,\text{mm}$, $a = 4.9\,\mu\text{m}$ and $D_{aperture} = 18.8\,\text{mm}$ yields a maximum of $l_{max} = 1.448\,\text{mm}$ for the points on the object surface edges (as depicted in figure A.3).

In the image plane, our diameter (area) of interest is D_{image}. We wish not for larger spatial frequencies that reenters the numerical window upon exit to reach this area. To accommodate for this requirement it is sufficient to choose a grid size D_{grid} in the image plane that obeys:

$$\frac{D_{illum} + D_{image}}{2} \leq D_{grid} \tag{A.27}$$

where $D_{illum} = 2l_{max}$. At equality, the reentered frequencies just reach the edge of the area of interest. Using a numerical FFT for solving (4.1) will result in a field at the image plane sampled at points separated with a distance b according to (A.28):

$$b = \frac{R\lambda}{Na} \tag{A.28}$$

where N is the number of samples along one side of the grid. The grid diameter in the image plane can thus be written as $D_{grid} = Nb = R\lambda/a$. For our sampling distance we thus have two requirements to fulfill:

$$a: \begin{cases} 1 \leq \frac{2R\lambda}{a(D_{illum}(a)+D_{image})} = \text{A} \\ 1 \leq \frac{\delta_{max}}{a\sqrt{2}} = \text{B} \quad \text{for equality in (A.21)} \end{cases} \tag{A.29}$$

Remember that D_{illum} depends on l_{max} which depends on sampling distance a. We can evaluate these expressions for a range of sampling distances. The result is visualised in figure A.4 (assuming $D_{image} = 200\,\mu\text{m}$).

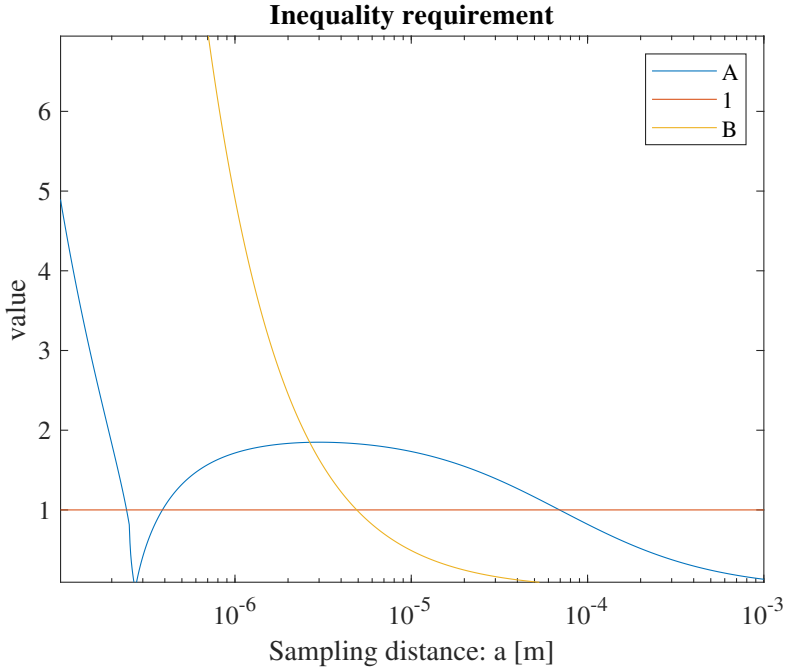

Figure A.4: Numerical evaluation of (A.29).

From figure A.4 we see that B is a stricter constraint and it is thus sufficient to choose a as $a = \delta_{max}/\sqrt{2}$. For the number of samples N we require that $D_{aperture} \leq Na$ where $D_{aperture}$ is the maximum aperture in the object plane. Of course, N must also satisfy (A.27) ($D_{grid} = Nb$). It is advantageous to choose as large sampling distance a as possible, not just to minimise computational time but also with respect to reducing reentering spatial frequencies as well as obtaining a higher resolution in the image plane (see (A.28)). With respect to computational time we combine this choice of a with the number of samples N that fulfills $D_{aperture} = Na$ as long as this complies with (A.27). If, as an example, $D_{aperture} = 18.8\,\text{mm}$ and the largest possible sampling distance $a = 4.9\,\mu\text{m}$ we obtain $N = 3832$ which gives $D_{grid} = 2.8\,\text{mm}$ which is much larger than $D_{image} = 200\,\mu\text{m}$ and approximately equal to $2l_{max}$ for the above parameter values (R, λ). Thus (A.27) is fulfilled and we have found a valid combination of N and a. If one desires finer resolution in the image plane it is

possible to increase the number of samples N at a cost of computational time, D_{grid} will remain constant.

It should be noted that during simulation, aliasing has been observed within the area of interest despite meeting the above stated conditions. Reasons might be under-sampled signals that reach further out than expected.

A.2 Schwarzschild raytracing

The aim of this model is to calculate the field in plane P_0 for any given input ray as a function of y. See figure A.5. All incoming rays have a wave vector $\mathbf{k}_0 = [k_x, k_y] = \frac{2\pi}{\lambda}[1, 0]$ for any given starting $y = y_0$. Starting at the input of the objective each ray's respective coordinate is $\mathbf{r} = [-l_1, y]$. From here they travel to the corresponding point $\mathbf{r}_0 = [-l_1 + l_2 + R_1 - \sqrt{R_1^2 - y^2}, y] = [f - \sqrt{R_1^2 - y^2}, y]$ along $\mathbf{k}_0$.

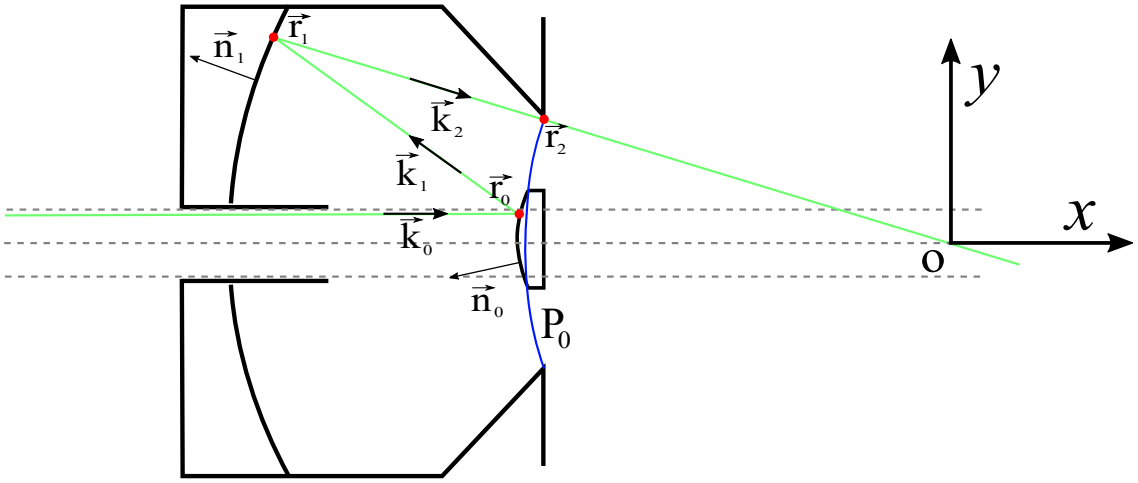

Figure A.5: Schematic for the ray tracing model.

To calculate $\mathbf{k}_1(y)$ we make use of $\mathbf{n}_0(y) = \frac{\nabla R_1}{|\nabla R_1|} = \frac{\nabla([x+f]^2+y^2)}{|\nabla R_1|} = 2[x+f, y]/2([x+f]^2+y^2)^{\frac{1}{2}} = \frac{1}{R_1}[\sqrt{R_1^2 - y^2}, y]$. We need only consider $y > 0$, if so we have $\theta_{\mathbf{k}_0,\mathbf{k}_1}(y) = 2\arccos(\mathbf{n}_0(y) \bullet \mathbf{k}_0(y)/|\mathbf{k}_0(y)|) = 2\arccos(\frac{1}{R_1}\sqrt{R_1^2 - y^2})$. Here $< \bullet >$ is a scalar product. We obtain $\mathbf{k}_1(y) = \hat{R}(\theta_{\mathbf{k}_0,\mathbf{k}_1}(y))\mathbf{k}_0(y)$ where $\hat{R}$ is the 2D rotational matrix. Now that we have $\mathbf{r}_0(y_0)$ and $\mathbf{k}_1(y_0)$ we can use $\mathbf{k}_1$ to propagate the ray from the corresponding $\mathbf{r}_0$ until we reach R_2. We can express each point $\mathbf{r}_1 = \mathbf{r}_1(y_1) = [f - \sqrt{R_2^2 - y_1^2}, y_1]$. We can now solve for the system of equations:

$$s_1 \frac{\mathbf{k}_1}{k_1} + \mathbf{r}_0 = \mathbf{r}_1$$

$$\Leftrightarrow$$

$$s_1 \begin{pmatrix} \cos\theta_{\mathbf{k}_0,\mathbf{k}_1} & -\sin\theta_{\mathbf{k}_0,\mathbf{k}_1} \\ \sin\theta_{\mathbf{k}_0,\mathbf{k}_1} & \cos\theta_{\mathbf{k}_0,\mathbf{k}_1} \end{pmatrix} \begin{pmatrix} 1 \\ 0 \end{pmatrix} + \begin{pmatrix} f - \sqrt{R_1^2 - y_0^2} \\ y_0 \end{pmatrix} = \begin{pmatrix} f - \sqrt{R_2^2 - y_1^2} \\ y_1 \end{pmatrix}$$

for the unknowns s_1 and y_1. As before we use the surface normal $\mathbf{n}_1(y_1) = \frac{1}{R_2}[\sqrt{R_2^2 - y_1^2}, y_1]$ and $\mathbf{k}_1$ to calculate $\theta_{\mathbf{k}_1,\mathbf{k}_2}(y_0) = \pi + 2\arccos(\mathbf{n}_1(y_0) \bullet \mathbf{k}_1(y_0)/|\mathbf{k}_1(y_0)|)$. We then calculate $\mathbf{k}_2 = \hat{R}(\theta_{\mathbf{k}_1,\mathbf{k}_2})\mathbf{k}_1$. Using $\mathbf{r}_2(y_2) = [-\sqrt{R^2 - y_2^2}, y_2]$, where R is the distance from $x = 0$, $y = 0$ to P_0, we arrive at another system of equations:

$$s_2 \frac{\mathbf{k}_2}{k_2} + \mathbf{r}_1 = \mathbf{r}_2 \tag{A.30}$$

which we solve for the unknowns s_2 and y_2. Define $s_0 = |\mathbf{r}_0(y_0) - \mathbf{r}(y_0)|$ then we calculate the electric field in each point $\mathbf{r}_2$ of P_0 as:

$$E_1(y_2(y_0)) = |E_0(y_0)| e^{i\frac{2\pi}{\lambda}[s_0(y_0) + s_1(y_0) + s_2(y_0)]} \tag{A.31}$$

where E_1 is the field in P_0 and E_0 the input field. A numeric interpolation generates 2D data.

A.3 Constant curvature aperture

This section aims to provide a quantitative description of the aperture geometry used for constant curvature vanes. In the case of a large focal distance objective, such that the transmitting rays are approximately parallel to the optic axis over the entire aperture, the starting plane can be approximated as planar. The aperture geometry is then relatively simple, see figure A.6.

Knowledge about the arm width w, arc angle θ as well as inner and outer radius r_a & r_b is sufficient as to determine the remaining parameters, see (A.32).

$$\begin{cases} r' = \frac{(r_b - r_a)/2}{\sin(\theta/2)} \\ R' = \sqrt{(r_a/2 + r_b/2)^2 + (r'\cos(\theta/2))^2} \\ \phi = \arccos\left(\frac{R'^2 + r_a^2 - r'^2}{2R'r_a}\right) \end{cases} \tag{A.32}$$

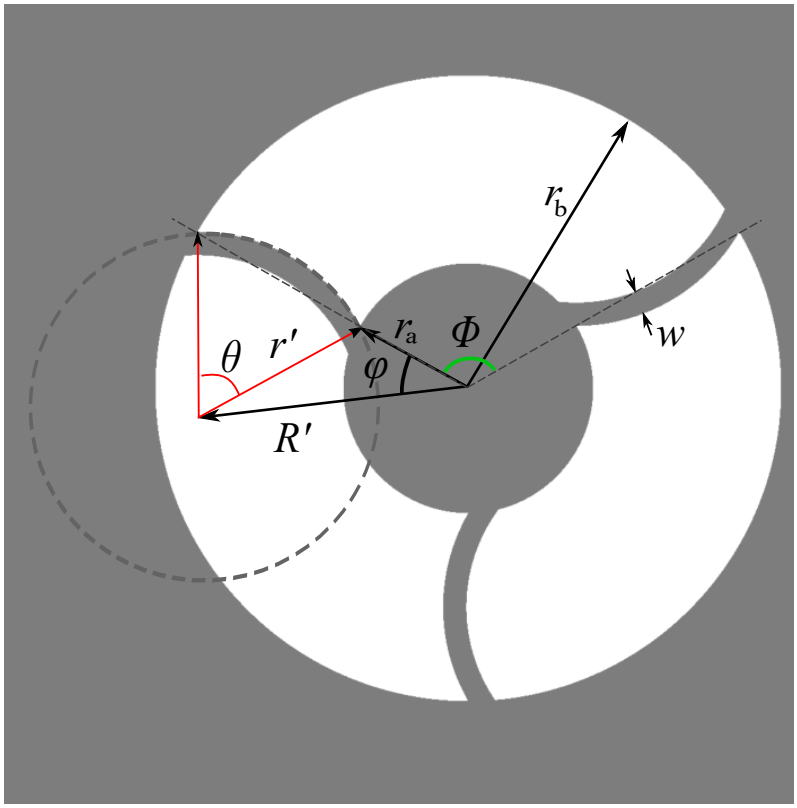

Figure A.6: The planar aperture geometry. The constant curvature of the vanes are defined by the border of the dashed circle with radius r' and a slightly smaller concentric circle with radius $r' - w$, where w is the arm width. θ is the angle subtended by a single vane, Φ is the angle offset between vanes.

For microscope systems with shorter focal lengths the rays are no longer parallel but rather convergent. Thus the starting plane is a spherical surface where the definition of constant curvature vanes become more complex. A constant curvature vane is in this case bounded by a small circle (S_c) crossing a great circle (G_{ab}) which intersects the aperture centre, see figure A.7 a). The small circle S_c makes angles θ'_{arc} with G_{ab} and the inner and outer circular obscurations are bounded by small circles S_a and S_b. Note that a small circle is a regular circle lying in a plane with a radius smaller than the sphere radius upon which it is projected. The same goes for a great circle with the difference being its radius equalising the sphere radius. S_c is centred in point P_c, has radius r_c and intersects points P_a, P_b and P_2. The subtended angle θ_{arc} by the curved vane is the integrated angular change of S_c with respect to the plane of G_{ab} between points P_a and P_b which we, using figure A.7 a) can relate according to (A.33). Using figures A.7 a-g) and the corresponding relations given in (A.33), (A.34) and (A.35) we can determine the unknown parameters from the knowledge of R, r_a, r_b, θ_{arc} and w.

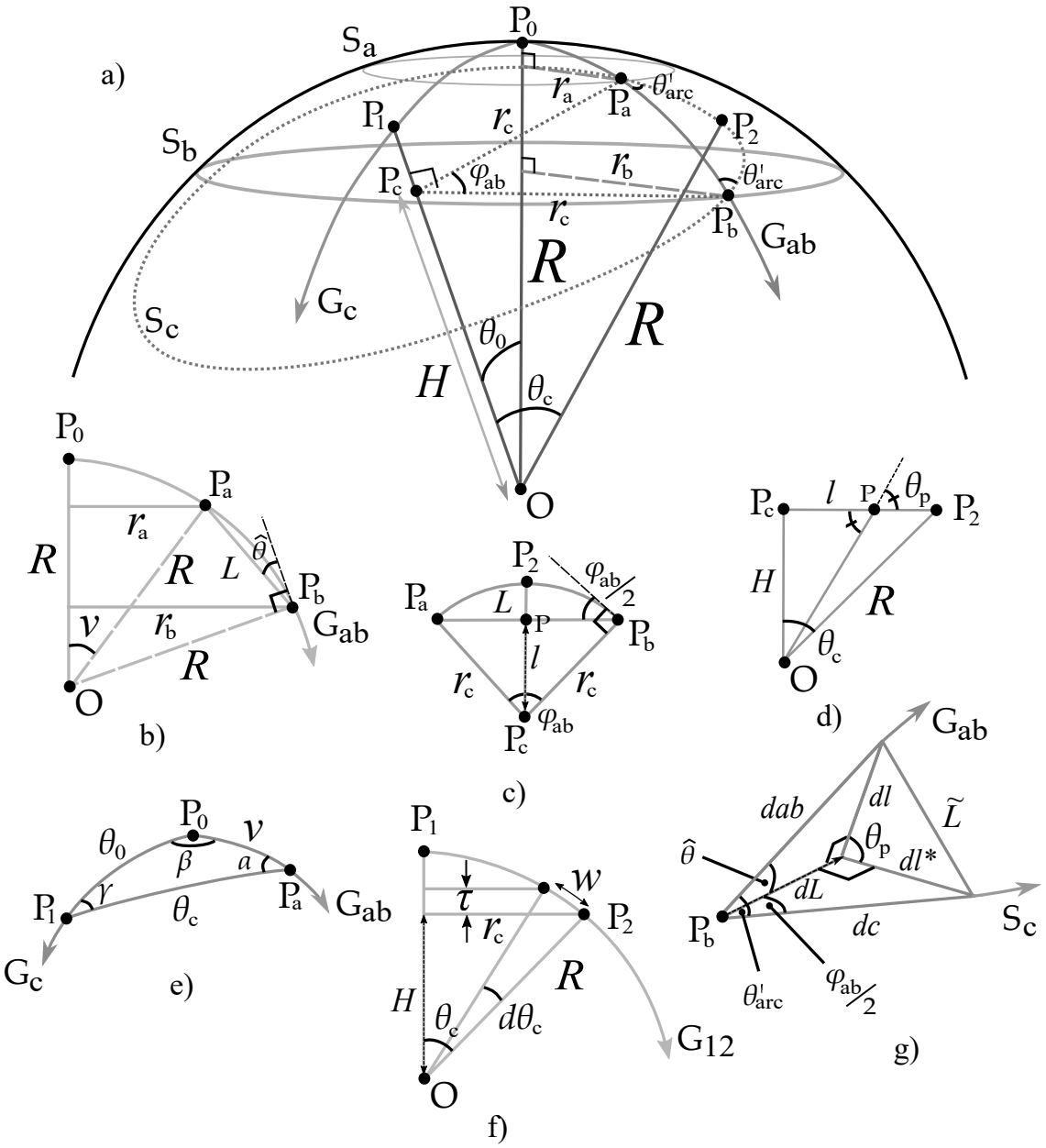

Figure A.7: A schematic providing a visualisation of the different parameters used for evaluating the spherical aperture geometry for constant curvature vanes.

$$\text{a):}\begin{cases} H^2 = R^2 - r_c^2 \\ \theta'_{\text{arc}} = \theta_{\text{arc}}/2 \\ \alpha = \frac{\pi}{2} + \theta'_{\text{arc}}, \quad \text{a) \& e)} \end{cases} \qquad \text{b):}\begin{cases} L^2 = (\sqrt{R^2 - r_a^2} - \sqrt{R^2 - r_b^2})^2 + (r_b^2 - r_a^2)^2 \\ v = \arcsin\frac{r_a}{R} \\ \hat{\theta} = \frac{1}{2}(\arcsin\frac{r_b}{R} - \arcsin\frac{r_a}{R}) \end{cases} \tag{A.33}$$

$$\text{c) \& d):}\begin{cases} l = \frac{L}{2\tan(\phi_{ab}/2)} \\ r_c = \frac{L}{2\sin(\phi_{ab}/2)} \\ \theta_p = \arctan\frac{H}{l} \end{cases} \qquad \text{e):}\begin{cases} \cos\theta_0 = \cos\theta_c \cos v + \sin\theta_c \sin v \cos\alpha \\ \frac{\sin\beta}{\sin\theta_c} = \frac{\sin\alpha}{\sin\theta_0} \\ \frac{\sin\gamma}{\sin v} = \frac{\sin\beta}{\sin\theta_c} \end{cases} \tag{A.34}$$

$$\text{f):}\begin{cases} d\theta_c = w/R \\ \tau = R(\cos(\theta_c - d\theta_c) - \cos\theta_c) \\ \theta_c = \arctan\frac{r_c}{H} \end{cases} \quad \text{g):}\begin{cases} dc = \frac{dL}{\cos(\phi_{ab}/2)} \\ dab = \frac{dL}{\cos\hat{\theta}} \\ dl^* = dL\tan(\phi_{ab}/2) \\ dl = dL\tan\hat{\theta} \\ \tilde{L}^2 = dab^2 + dc^2 - 2dab\cdot dc\cos\theta'_{\text{arc}} \\ \tilde{L}^2 = dl^2 + dl^{*2} - 2dl^*\cdot dl\cos\theta_p \end{cases} \tag{A.35}$$

Figure A.7 g) represents a corner of the intersection between G_{ab}, S_c and the straight line between points P_a and P_b. If we let $dL \to 0$ the relations given in (A.35) g) become justified and by dividing with dL we arrive at the following expression:

$$\begin{cases} 0 = \tan^2\hat{\theta} + \tan^2(\phi_{ab}/2) - 2\tan\hat{\theta}\tan(\phi_{ab}/2)\cos\theta_p(\phi_{ab}) - \frac{1}{\cos^2\hat{\theta}} - \frac{1}{\cos^2(\phi_{ab}/2)} + 2\frac{\cos\theta'_{\text{arc}}}{\cos\hat{\theta}\cos(\phi_{ab}/2)} \\ \theta_p(\phi_{ab}) = \arctan\left\{\frac{\sqrt{R^2 - L^2/(4\sin^2(\phi_{ab}/2))}}{L/(2\tan(\phi_{ab}/2))}\right\} \end{cases} \tag{A.36}$$

The first equation in (A.36) contains only one unknown (ϕ_{ab}). Thus we can solve it numerically for ϕ_{ab} and together with (A.33), (A.34) and (A.35) the remaining parameters are readily determined.

A.4 Field canceling analysis

Consider two aperture functions, (A.37) and (A.38):

$$p_1(x,y) = \begin{cases} 1, & -l/2 \le x \le l/2, \quad -w/2 \le y \le w/2 \\ 0, & \text{else} \end{cases} \tag{A.37}$$

$$p_2(x,y) = \begin{cases} -1, & -l/2 \le x - x_0 \le l/2, \quad -w/2 \le y - y_0 \le w/2 \\ 0, & \text{else} \end{cases} \tag{A.38}$$

Their corresponding fourier transforms are, (A.39) and (A.40):

$$F_1 \propto wl\text{sinc}\left(\frac{lx}{\lambda d}\right)\text{sinc}\left(\frac{wy}{\lambda d}\right) \tag{A.39}$$

$$F_2 \propto -wl\text{sinc}\left(\frac{lx}{\lambda d}\right)\text{sinc}\left(\frac{wy}{\lambda d}\right)\exp\left[-j\frac{2\pi(xx_0 + yy_0)}{\lambda d}\right] \tag{A.40}$$

It is now clear that the spatial separation (x_0, y_0) must vanish for the fields to completely cancel out everywhere. However, it is interesting to see whether the fields can be made to cancel out the high intensity spikes caused by the arm width w along $x = 0$. For this to work we must set $y_0 = 0$. Let's redefine the aperture functions as in (A.41) and (A.42):

$$p_1(x,y) = \begin{cases} 1, & -l/2 \leq x - x_0 \leq l/2, \quad -w/2 \leq y \leq w/2 \\ 0, & \text{else} \end{cases} \tag{A.41}$$

$$p_2(x,y) = \begin{cases} -1, & -l/2 \leq x + x_0 \leq l/2, \quad -w/2 \leq y \leq w/2 \\ 0, & \text{else} \end{cases} \tag{A.42}$$

Their corresponding fourier transforms are, (A.43) and (A.44):

$$F_1 \propto wl\text{sinc}\Big(\frac{lx}{\lambda d}\Big)\text{sinc}\Big(\frac{wy}{\lambda d}\Big)\exp\Big[-j\frac{2\pi x x_0}{\lambda d}\Big] \tag{A.43}$$

$$F_2 \propto -wl\text{sinc}\Big(\frac{lx}{\lambda d}\Big)\text{sinc}\Big(\frac{wy}{\lambda d}\Big)\exp\Big[j\frac{2\pi x x_0}{\lambda d}\Big] \tag{A.44}$$

If we superpose these fields we end up with (A.45):

$$E \propto 2wl\text{sinc}\Big(\frac{lx}{\lambda d}\Big)\text{sinc}\Big(\frac{wy}{\lambda d}\Big)\sin\Big(\frac{2\pi x x_0}{\lambda d}\Big) \tag{A.45}$$

The sine term in this expression sets the intensity along $x = 0$ to zero, however, to reduce the intensity in the entire first order diffraction spike we can require that the sine function should oscillate slower along x than the sinc in x. This bears the following implication, (A.46):

$$\frac{lx}{\lambda d} \geq \frac{2\pi x x_0}{\lambda d} \Rightarrow l \geq 2\pi x_0 \tag{A.46}$$

(A.46) states that the two apertures p_1 and p_2 must overlap which is an impossible geometry. Thus it would seem that we cannot suppress the intensity spikes using this approach.

A.5 Interference noise filtering

When determining an optimum θ_{arc} for the purposes of this thesis it is of interest to find a measure's general dependence on this parameter without influence of small scale interference effects. By averaging over several parameter sweeps the influence of interference noise can be suppressed. The performed data averaging is presented in this section.

Consider a measure $X = X_{p^{(i)}}(\theta_{\text{arc}}, p)$ which is a function of arc angle θ_{arc} and a sweep parameter $p \in p^{(i)}$. First, an averaged version of X in $p^{(i)}$ is evaluated, (A.47):

$$\bar{X}_{p^{(i)}}(\theta_{\text{arc}}) = \frac{1}{N_p}\sum_{n}^{N_p} X_p(\theta_{\text{arc}}, p(n)) \tag{A.47}$$

where N_p is the number of data points in $p^{(i)}$. Then a position dependent offset in X from $\bar{X}_{p^{(i)}}$ is calculated as, (A.48):

$$\Delta X_p(\theta_{\text{arc}}, p) = G(X_p(\theta_{\text{arc}}, p) - \bar{X}_{p^{(i)}}(\theta_{\text{arc}})) \tag{A.48}$$

Here G represents a moving gaussian averaging window of size = 20 data points. This method of calculating the offset was used to accommodate the possible dependence between θ_{arc} and $p^{(i)}$. The filtered measure X at each value in $p^{(i)}$ is then calculated as, (A.49):

$$\tilde{X}_p(\theta_{\text{arc}}, p) = \bar{X}_{p^{(i)}}(\theta_{\text{arc}}) + \Delta X_p(\theta_{\text{arc}}, p) \tag{A.49}$$

For use in the final averaging over all sweeps a measure of the fluctuations in X for each parameter $p^{(i)}$ is calculated as, (A.50):

$$\sigma_{p^{(i)}}(\theta_{\text{arc}}) = \sqrt{\frac{1}{N_p}\sum_{n}^{N_p}\left(X_p(\theta_{\text{arc}}, p(n)) - \tilde{X}_p(\theta_{\text{arc}}, p(n))\right)^2} \tag{A.50}$$

For calculating the total average measure $\bar{X}(\theta_{\text{arc}})$ at the device parameters of interest: $p_0^{(i)} \in p^{(i)}$ a weighted average between parameter specific averages is done using the fluctuations from (A.50):

$$\bar{X}(\theta_{\text{arc}}) = \sum_{k}^{M} \frac{\sigma_{p^{(k)}}(\theta_{\text{arc}})}{\sum_k^M \sigma_{p^{(k)}}(\theta_{\text{arc}})} \tilde{X}_p(\theta_{\text{arc}}, p_0^{(k)}) \tag{A.51}$$

where M is the number of sweep parameters $i = 1, 2..M$.

The filtered versions of σ_θ and S_M was obtained using the above presented method utilising parameter sweeps over w, r_i, λ with exact values given in table A.1. The device parameters p_0 are $\lambda = 543$ nm, $w = 0.7$ mm, $r = 4.4$ mm. While sweeping over one parameter the others were kept locked at p_0 values. Additionally, for the filtered version of the spike magnitude S_M a gaussian averaging filter was applied using a window width of 5 points for further smoothing.

Table A.1: Parameter values used for sweep averaging.

w [mm]	0.05 & [0.1, 0.2, 0.3, .. 2.0]
r [mm]	[3.5→ 5.4] 20 points, linear spacing
λ [nm]	[200, 300, .. 1000] & 1500, 2000, 3000, 5000, 543

A.6 Gaussian arm calculation

This section provides the method for estimating the Gaussian arm shape that was used in this thesis work. The Gaussian arm shape coordinates can be written $\mathbf{r}(l)$ where l is the length coordinate of the arm. Using equations (5.14) and (5.15), repeated here for convenience (A.52) and (A.53) respectively, and from the knowledge of the initial condition $\mathbf{r}(l = 0) = r_i\hat{x}$ and the beam radius w_ρ the arm shape can be determined. Here I is the Gaussian distributed intensity, w the arm width and ρ the radial coordinate. For a depiction of the geometry and coordinates used here, please refer to figure A.8 where also the coordinate θ is defined.

$$\text{const} = w\frac{dl}{d\theta}I(\mathbf{r}) \tag{A.52}$$

$$I(\rho) = I_0 \exp\Big[- \frac{2\rho^2}{w_\rho^2}\Big] \tag{A.53}$$

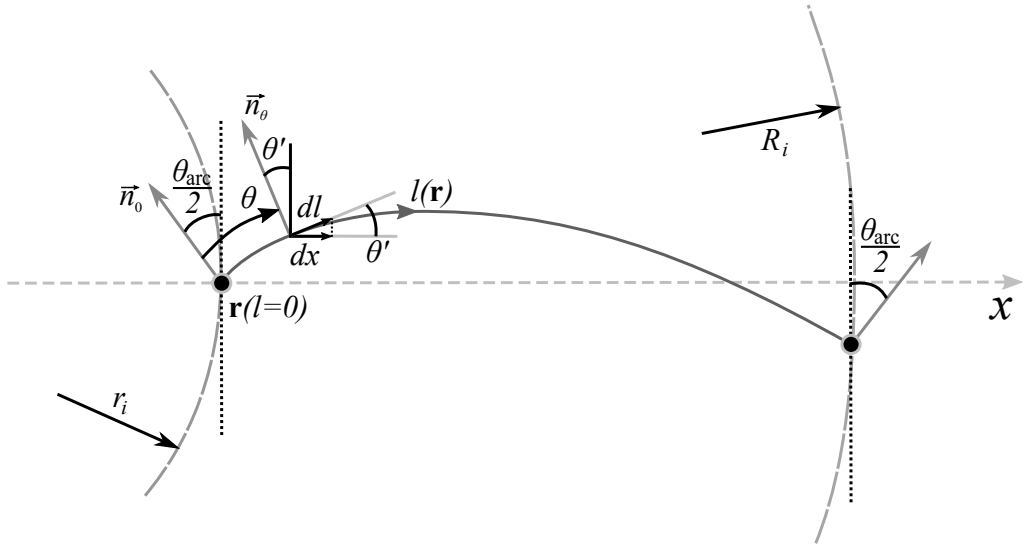

Figure A.8: An illustration of the geometry and coordinates used for determining the gaussian arm shape $\mathbf{r}(l)$.

The figure overviews the aperture section between the inner and outer obscuration circles (r_i and R_i) and furthermore presents the vector normal $\mathbf{n}_\theta(l)$ to the line $\mathbf{r}(l)$ as well as visualising the arc angle θ_{arc}. From figure A.8 we realise the arm shape can be determined as, (A.54):

$$\mathbf{r}(l) = \mathbf{r}(0) + \int_0^l \frac{\left(\frac{d\mathbf{n}_\theta}{dl}\right)}{\left|\frac{d\mathbf{n}_\theta}{dl}\right|} dl \tag{A.54}$$

To evaluate (A.54) we need to find an expression for the integrand. We start by inserting (A.53) into (A.52) and using the relations $\frac{dx}{dl} = \cos\theta'$, $\theta' = \theta_{\text{arc}}/2 - \theta$ observed in figure A.8 we obtain (A.55):

$$\frac{dx e^{-\frac{2\rho^2}{w_\rho^2}}}{C} = d\theta \cos\Big(\frac{\theta_{\text{arc}}}{2} - \theta\Big) \tag{A.55}$$

The constants w, I_0 and const are embedded into the new constant $C = \frac{\text{const}}{wI_0}$. To simplify the calculations in the pursuit of C the approximation $x \approx \rho \Rightarrow dx \approx d\rho$ is made. This is approximately true if r_i is sufficiently large. Next we integrate (A.55) and arrive in, (A.56):

$$\int_{r_i}^{\rho} \frac{e^{-\frac{2\rho^2}{w_\rho^2}} d\rho}{C} = \int_0^{\theta} \cos\Big(\frac{\theta_{\text{arc}}}{2} - \theta\Big) d\theta$$

$$\Rightarrow$$

$$\frac{\sqrt{\pi} w_\rho}{2\sqrt{2}C}\Big[\text{erf}\Big(\frac{\sqrt{2}\rho}{w_\rho}\Big) - \text{erf}\Big(\frac{\sqrt{2} r_i}{w_\rho}\Big)\Big] = \sin\frac{\theta_{\text{arc}}}{2} - \sin\Big(\frac{\theta_{\text{arc}}}{2} - \theta\Big) \quad \text{(A.56)}$$

From here we obtain $\theta(\rho)$ according to, (A.57):

$$\theta(\rho) = \frac{\theta_{\text{arc}}}{2} - \arcsin\left\{ \sin\frac{\theta_{\text{arc}}}{2} - \frac{\sqrt{\pi} w_\rho}{2\sqrt{2}C}\Big[\text{erf}\Big(\frac{\sqrt{2}\rho}{w_\rho}\Big) - \text{erf}\Big(\frac{\sqrt{2} r_i}{w_\rho}\Big)\Big] \right\} \quad \text{(A.57)}$$

and by using $\theta(R_i) = \theta_{\text{arc}}$ we find C, (A.58):

$$C = \frac{\frac{\sqrt{\pi} w_\rho}{2\sqrt{2}}\Big[\text{erf}\Big(\frac{\sqrt{2}\rho}{w_\rho}\Big) - \text{erf}\Big(\frac{\sqrt{2} r_i}{w_\rho}\Big)\Big]}{2\sin\frac{\theta_{\text{arc}}}{2}} \quad \text{(A.58)}$$

The vector normal $\mathbf{n}_\theta$ to $\mathbf{r}(l)$ is easily determined as a function of θ, (A.59):

$$\mathbf{n}_\theta = \hat{R}(-\theta)\mathbf{n}_0, \quad \mathbf{n}_0 = \hat{R}\Big(\frac{\pi + \theta_{\text{arc}}}{2}\Big)\begin{pmatrix}1\\0\end{pmatrix} \quad \text{(A.59)}$$

Here $\hat{R}$ represents the 2D-rotation matrix. The derivative of $\mathbf{n}_\theta$ with respect to θ read as, (A.60):

$$\begin{pmatrix}\frac{dn_x}{d\theta}\\ \frac{dn_y}{d\theta}\end{pmatrix} = \begin{pmatrix}\sin\frac{\theta_{\text{arc}}}{2}\sin\theta + \cos\frac{\theta_{\text{arc}}}{2}\cos\theta\\ \sin\frac{\theta_{\text{arc}}}{2}\cos\theta - \cos\frac{\theta_{\text{arc}}}{2}\sin\theta\end{pmatrix} = \begin{pmatrix} n_y(\theta)\\ -n_x(\theta)\end{pmatrix} \quad \text{(A.60)}$$

From $\frac{d\mathbf{n}_\theta}{dl} = \frac{d\mathbf{n}_\theta}{d\theta}\frac{d\theta}{d\rho}\frac{d\rho}{dl}$ we find the expression for the integrand in (A.54) as, (A.61):

$$\frac{\Big(\frac{d\mathbf{n}_\theta}{dl}\Big)}{\Big|\frac{d\mathbf{n}_\theta}{dl}\Big|} dl = \frac{\frac{d\theta}{d\rho}\frac{d\rho}{dl}\Big(\frac{dn_x}{d\theta}\hat{x} + \frac{dn_y}{d\theta}\hat{y}\Big)}{\Big|\frac{d\theta}{d\rho}\frac{d\rho}{dl}\Big|\sqrt{\Big(\frac{dn_x}{d\theta}\Big)^2 + \Big(\frac{dn_y}{d\theta}\Big)^2}} dl = \frac{n_y(\theta)\hat{x} - n_x(\theta)\hat{y}}{\sqrt{n_y(\theta)^2 + n_x(\theta)^2}} dl \quad \text{(A.61)}$$

where in the last step the assumption $\frac{d\theta}{d\rho}\frac{d\rho}{dl} > 0$ was made. The differential length element can be rewritten, using $dl = \frac{dl}{d\theta}\frac{d\theta}{d\rho}d\rho$ with $\frac{dl}{d\theta}$ from (A.52) and $\frac{d\theta}{d\rho}$ from (A.55) where $dx \approx d\rho$ we find, (A.62):

$$dl = \frac{\text{const}}{wI(\rho)} \frac{wI(\rho)}{\text{const}\cos\Big(\frac{\theta_{\text{arc}}}{2} - \theta\Big)} d\rho = \frac{d\rho}{\cos\Big(\frac{\theta_{\text{arc}}}{2} - \theta\Big)} \quad \text{(A.62)}$$

Finally we can rewrite the arm shape $\mathbf{r}(l)$ from (A.54) into, (A.63):

$$\mathbf{r}(\rho) = r_i\hat{x} + \int_{r_i}^{\rho} \frac{n_y(\theta)\hat{x} - n_x(\theta)\hat{y}}{\sqrt{n_y(\theta)^2 + n_x(\theta)^2}} \frac{d\rho}{\cos\Big(\frac{\theta_{\text{arc}}}{2} - \theta\Big)} \quad \text{(A.63)}$$

where $\mathbf{n}_\theta(\theta)$ is given by (A.60) and $\theta = \theta(\rho)$ is given by (A.57) and (A.58). For numeric evaluation the integral becomes a sum, (A.64):

$$\mathbf{r}(\rho_{m+1}) = r_i\hat{x} + \sum_{k=0}^{m} \frac{n_y(\theta(\rho_k))\hat{x} - n_x(\theta(\rho_k))\hat{y}}{\sqrt{n_y(\theta(\rho_k))^2 + n_x(\theta(\rho_k))^2}} \frac{\Delta\rho}{\cos\left(\frac{\theta_{\text{arc}}}{2} - \theta(\rho_k)\right)}, \quad \rho_p = r_i + p\Delta\rho \tag{A.64}$$

When calculating $\mathbf{r}(\rho)$ using (A.64) the step $\Delta\rho$ should be sufficiently small. In the project a common choice was to take $\Delta\rho = a$ where a is the sampling distance in the object plane.

B

Appendix 2

B.1 Equipment

Here the equipment utilised for the experimental setup is presented:

- He-Ne-laser, $\lambda = 543\,\mathrm{nm}$
- Reflective fiber collimator, Thorlabs RC12APC-F01
- SM-fiber, length 1.5 m
- Large beam fiber collimator, Thorlabs C40APC-A, providing near output Gaussian beam with $2w_0 = 7.4\,\mathrm{mm}$
- Schwarzschild objective, Thorlabs LMM-15X-P01 prototype with arm width $w = 0.9\,\mathrm{mm}$.
- Schwarzschild objective, Thorlabs LMM-15X-UVV prototype with arm width $w = 0.7\,\mathrm{mm}$ and employing constant curvature vanes of arc angle $\theta_{\mathrm{arc}} = 60°$.
- 40X achromatic microscope objective (used for experiment in section 4.3.3)
- 50X objective, Olympus MPLFCN 50/0.8 (used for experiment in section 7.1)
- SM1 lens tubes
- tube lens, $f = 200\,\mathrm{mm}$
- Scientific camera, Thorlabs 340M-USB, pixel size 7.4 µm
- Annular obscuration target, Thorlabs R1DF50
- Optics table, mechanical mounts and translational stages.
- Optical power meter

Pictures of the setup are presented in figure B.1.

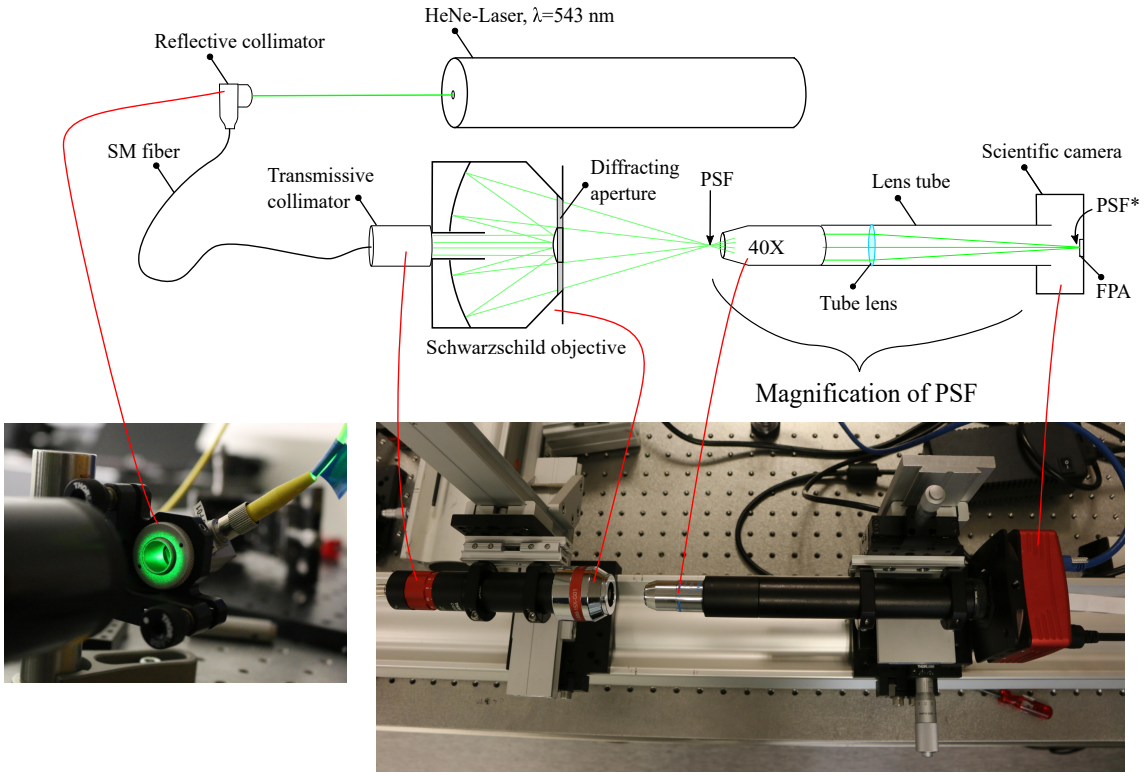

Figure B.1: A photo of the experimental setup. Some of the components are emphasised in the schematic.

B.2 Simulation parameters

For most simulations similar parameter values were used and it is thus considered convenient to gather this data here for reference. If not otherwise specified, the following simulation parameters were used, see table B.1:

Table B.1: The general simulation parameters for the 15X and 40X Schwarzschild objectives. R is the propagation distance, r_i the inner physical circular obscuration, R_i the outer physical circular obscuration, a the shortest distance between samples in the object plane, N the number of samples along each row and column, α, the minimum phase difference of half a cycle, D_{image} the image plane size of interest, θ_{arc} the arc angle subtended by a single spider arm, w the spider arm width, t the spider arm thickness, λ wavelength, f focal length, L aperture distance and y_1 entrance pupil radius.

	r_i [mm]	R_i [mm]	R [cm]	a [µm]	N	α	D_{image} [µm]
15X	3.8	9.4	2.89	5.5368	7000	0.1	200
40X	2.1	6.0	1.28	6.6459	2632	0.1	75

	w [mm]	t [mm]	λ [nm]	f [mm]	L [mm]	y_1 [mm]
15X	0.7	3	543	13.3	24.3	4
40X	0.6	1.3	543	5	10	2.55

B.3 Data merging algorithm

The algorithm employed for the merging of data is presented below:

(NF=Noise Factor, UL=Upper Limit, D=Data, M.i=measurement #i, N=Noise, RN=Relative Noise, NT=Noise threshold, PV=Peak Value, ND=Normalised Data, ×=element-vise multiplication, imregister=a function used to translate the image data as to match different measurements (essentially for suppressing effects of vibrations during measurement).)

η_l = NF ▷ A safe limit, used to remove noise below a certain value
η_u = UL ▷ A safe limit, used to remove saturated values above a certain value
for $i = 1$: number of measurements **do**
D(i) = import(M.i) ▷ Loading measurements with increasing exposure times (or power), measurements are 2D-arrays of doubles.
N(i) = $\sum \frac{\text{D}(i,\text{window edges})}{\text{number of elements(window edges)}}$ ▷ Calculate mean noise value from mean of data far from PSF peak.
RN(i) = N(i)/Max(D(i)) ▷ The relative noise value
NT(i) = η_lRN(i) ▷ Calculate noise threshold
D(i) = D(i) − N(i) ▷ Remove noise
PV(i) = Max(D(i)) ▷ Determine peak value
ND(i) = D(i)/Max(D(i)) ▷ Calculate normalised data
if i=1 **then**
Image = D(i) × (NT(i) < ND(i)) ▷ Sets all data points below the threshold to zero and adds to the total image.
else if $i > 1$ **then**
ND(i) = imregister(ND(i), ND($i-1$), ..) ▷ Matching the two data sets in space
$g(i)$ = findgain(RN($i-1$), η_u, D($i-1$), D(i)) ▷ Calculates the gain between consecutive measurements from their spatial overlap within the dynamic window
Image = $g(i)$ × Image + D(i) × (NT(i) < ND(i)) × (D(i) ≤ $g(i)$ × PV($i-1$) × NT(i)) ▷ Stack the data into the final image
end if
end for

---

function gain=findgain(l_l, u_l, l_m, u_m)
$g_m = (l_l \times \text{Max}(l_m) z < l_m) \times (u_m < \text{Max}(u_m) \times u_l) \times \frac{u_m}{l_m}$ ▷ Calculate the gain between two consecutive measurements in each spatial point and within the overlap specified by the lower and upper limits: l_l and u_l.
g_m(isnan(g_m)) = 0 ▷ Remove nan-values
gain= $\frac{\sum g_m}{\sum (g_m \neq 0)}$ ▷ Calculate mean gain

---